Growth of GaN Nanowires:

A Study Using In Situ Transmission Electron Microscopy

by

Rosa Estela Díaz Rivas

A Dissertation Presented in Partial Fulfillment
of the Requirements for the Degree
Doctor of Philosophy

Approved November 2010 by the
Graduate Supervisory Committee:

Subhash Mahajan, Chair
William Petuskey
Peter Crozier

ARIZONA STATE UNIVERSITY

December 2010

ABSTRACT

Owing to their special characteristics, group III-Nitride semiconductors have attracted special attention for their application in a wide range of optoelectronic devices. Of particular interest are their direct and wide band gaps that span from ultraviolet to the infrared wavelengths. In addition, their stronger bonds relative to the other compound semiconductors makes them thermally more stable, which provides devices with longer life time. However, the lattice mismatch between these semiconductors and their substrates cause the as-grown films to have high dislocation densities, reducing the life time of devices that contain these materials.

One possible solution for this problem is to substitute single crystal semiconductor nanowires for epitaxial films. Due to their dimensionality, semiconductor nanowires typically have stress-free surfaces and better physical properties. In order to employ semiconductor nanowires as building blocks for nanoscale devices, a precise control of the nanowires' crystallinity, morphology, and chemistry is necessary. This control can be achieved by first developing a deeper understanding of the processes involved in the synthesis of nanowires, and then by determining the effects of temperature and pressure on their growth.

This dissertation focuses on understanding of the growth processes involved in the formation of GaN nanowires. Nucleation and growth events were observed *in situ* and controlled in real-time using an environmental transmission electron microscope. These observations provide a satisfactory elucidation of the underlying growth mechanism during the formation of GaN nanowires.

Nucleation of these nanowires appears to follow the vapor-liquid-solid mechanism. However, nanowire growth is found to follow both the vapor-liquid-solid and vapor-solid-solid mechanisms. Direct evidence of the effects of III/V ratio on nanowire growth is also reported, which provides important information for tailoring the synthesis of GaN nanowires. These findings suggest *in situ* electron microscopy is a powerful tool to understand the growth of GaN nanowires and also that these experimental approach can be extended to study other binary semiconductor compound such as GaP, GaAs, and InP, or even ternary compounds such as InGaN. However, further experimental work is required to fully elucidate the kinetic effects on the growth process. A better control of the growth parameters is also recommended.

I dedicate this work to my family, especially my parents, Rosa and Coco, and my unconditional friend, David, for their love, support, and encouragement.

ACKNOWLEDGMENTS

First of all, I would like to thank my advisor, Prof. Subhash Mahajan, for the guidance and knowledge transferred to me throughout my graduate career. I would also like to thank Dr. Renu Sharma for introducing me to *in situ* electron microscopy and for her insight and guidance with my research. The research performed during my doctorate program could not have been completed without the financial support of the National Science Foundation.

Special thanks to Professor Crozier for his accurate comments on my research, for adopting me into his group, for advice with my career path, and for making Tecnai monthly meetings fun. I would also like to thank the people from the Center for Solid State Science, especially Karl Weis for his help and rapid response in solving instrumentation problems and Dr. Zhang Liu for his training with the microscopes used in this research. Also, I am deeply thankful to Professor Carpenter for his advice and helpful discussions on microscopy and encouragement with my career path.

I would like to thank the members of Dr. Mahajan's group: Zohair Zahidi for his assistance with data acquisition, Dr. Qinglei Zhang for his help with TEM, Heather McFelea for the brainstorming sessions, and Dr. Fanyu Meng for his help with HREM. I am also thankful to Dr. Karalee Jarvis for her help and support with TEM. I also would like to thank members of Dr. Crozier's group: Santhosh Shenna, Vaneet Sharma, and Dr. See Wee Chee, for their their help and assistance.

I am deeply grateful to my family, especially my parents Rosa and Coco, for their help and encouragement through my school years. Without their care and support I would not be here today – I really miss that fresh orange juice in the mornings. I also would like to thank my brothers, Jorge, Freddy and Tony, for their advice, support, and help through these years. I also need to thank my mother from a previous-life, best-friend, therapist, and partner in crime, David, for his support and precise comments during the last ten years of my life – my life would not be the same without you.

I want to express thanks for the support and encouragement that I got from Nick Meyers. His assistance with the microscope, help with my English, and advice on my career path will not be forgotten. Finally, I want to thank all the wonderful people that I met in Arizona, especially those good friends that kept me coming to KC's every week and made my years in grad school amusing. Special thanks goes to my friends Katie, Oscar, Maritza, Karalee, Heather, Stephanie, and Daniel that made my life really fun during the last five years. Those fun moments made me enjoyed grad school even more.

TABLE OF CONTENTS

Page

LIST OF TABLES

LIST OF FIGURES

Figure Page

Figure Page

Figure Page

CHAPTER 1

INTRODUCTION

1.1 Nanotechnology and nanoscience

Richard Feynman is mostly known for his work in quantum electrodynamics, for which he received a Novel Prize in Physics in 1965, and also for his introductory set of lectures on Physics, *"The Feynman Lectures on Physics"*, which changed the way physics was taught to the undergraduates. More importantly for materials science, Feynman was also known as the father of Nanotechnology (Hess, 2007).

On December of 1959, Feynman gave a talk at the annual meeting of the American Physical Society entitled *"There is plenty of room the bottom"* (Feyman, 1959). In this talk, he introduced the concept of nanotechnology for the first time. He considered the possibility of manipulating and controlling things at a "small" scale – the atomic scale. He suggested the idea of miniaturizing computers by making them of "little wires" with diameters ranging from 10 to 100 atoms. He also introduced the concept of the "bottom-up" and "top-down" approaches to fabricate nanoscale devices. He suggested that atoms could be put down in a certain arrangement by evaporating a particular material for the different components of the device, and also, he proposed to scale down existing technologies to build small machines that perform at an infinitesimal level. He also presented the idea – whose friend, Albert R. Hibbs, suggested originally – of incorporating a "mechanical surgeon" into the human body to assist some inadequately functioning organs.

In this talk, he also challenged physicist to built better electron microscopes. At the time, electron microscopes could only resolve 10 Å and he believed that it was not impossible to improve the resolution of electron microscopes by 100 times. Since the wavelength of an electron is 1/20 Å, he predicted that it should be possible to "see" individual atoms. He envisioned the importance to observe individual atoms in both biology and chemistry to respond to fundamental questions at that time.

When referring to the synthesis and characterization of matter at the nanoscale he gave the following statement:

"If you have a strange substance and you want to know what it is, you go through a long and complicated process of chemical analysis. You can analyze almost anything today, so I am a little late with my idea. But if the physicists wanted to, they could also dig under the chemists in the problem of chemical analysis. It would be very easy to make an analysis of any complicated chemical substance; all one would have to do would be to look at it and see where the atoms are. The only trouble is that the electron microscope is one hundred times too poor. Later, I would like to ask the question: Can the physicists do something about the third problem of chemistry – namely, synthesis? Is there a physical way to synthesize any chemical substance?"

- Richard Feynman.

He was proposing the development of atomic resolution microscopes coupled with analytical techniques that would provide the acquisition of chemical information at the atomic level. He would be pleased to know that physicist

exceeded his challenge with the development of microscopes that "see" individual atoms and synthesize "little wires" at the same time.

In 1974 Norio Taniguchi first defined the term 'nano-technology' in his paper, *"On the basic concept of Nano-Technology"* (Taniguchi, 1974), in which he considered nanotechnology as the ability to precisely engineer matter at the atomic level. Since then, the definition of nanotechnology has been extended and the National Science Foundation defines nanotechnology as "the ability to understand, control, and manipulate matter at the level of individual atoms and molecules, as well as at the 'supramolecular' level involving clusters of molecules, in the range of about 0.1 to 100 nm, in order to create materials, devices, and systems with fundamentally new properties and functions because of their small structure" (Roco, 2007).

A distinction should be made between nanotechnology and nanoscience. Nanoscience proposes a theory, upon which a technology could be developed. It focuses on the observation and study of phenomena at the nanoscale, as well as ways to manipulate matter at the same scale. Physical phenomena such as Debye length, excitation diffusion length, and electronic density of states are altered as the dimensions of the system are reduced. As a result, mechanical, optical, electrical, and magnetic properties arise that are different from those at the macroscale.

Nanotechnology and nanoscience are exciting fields that have and will offer revolutionary breakthroughs in many disciplines – from physics and

chemistry to biology and medicine. Even more powerful is and will be the overlapping of these disciplines to produce remarkably new technologies.

Such understanding and control of matter at the nanoscale promises a broad number of fundamental and technological new applications for industry, energy conversion, biomedicine, bioengineering, environmental engineering, computing, security, food, etc. Some application are, for example, detecting and treating cancer by subcellular intervention, cleaning oil spills by braking oil molecules with designed nanoparticles, processing of information using photons or electron spins, using hydrogen as energy source by using fuel cells based on nanoparticles or nanostructures, using solar energy by building more efficient solar cells with semiconductor nanostructures, reducing energy consumption by using light-emitting diodes (LEDs) based on semiconductor nanostructures as well, and the list goes on.

The importance of nanotechnology and nanoscience is such that in the year 2000 the US government decided to create the National Nanotechnology Initiative (NNI). This is a long-term (2000 – 2020) research and development program with an investment of over $12 billion (NNI, 2010) in the last decade. This program brings together 25 departments and independent agencies, including the National Science Foundation, the Department of Defense, the Department of Energy, the National Institutes of Health, the National Institute of Standards and Technology, and the National Aeronautical and Space Administration (Roco, 2007). The resulting outcome is the formation of an interdisciplinary nanotechnology and nanoscience community with about 50,000 contributors, over

60 large centers, networks, and user facilitates, as well as the participation of industry and business with more than 1500 companies.

In summary, nanotechnology and nanoscience are relative young and growing fields that include nearly every discipline of science and engineering. The advantage of reducing the size of materials is that their intrinsic properties may be changed for better, creating materials and devices that will outperform existing technologies. Although there have been significant breakthroughs in these fields over the last two decades, there is still a need for an even better understanding and a complete control of matter at the nanoscale to develop and enable technologies that have both innovative and powerful functionalities.

1.2 Nanostructure Materials

Most of the results and much of the interested in nanotechnology these days are focused on the study and applications of nanostructures. Nanostructured materials are defined as those materials with at least one spatial dimension ranging from 1 to 100nm (Brydson & Hammond, 2005). As it was indicated above, reducing the spatial dimensions of a structure to the nanoscale range has a dramatic impact on its physical properties and enables innovative technologies.

1.2.1 Nanostructure classification

Depending on the number of dimensions which lie within the nanoscale range, nanostructured materials can be classified into (a) zero dimensional nanostructures (0-D), where all three dimensions are confined in the nanoscale range, for example, quantum dots and nanoparticles (Figure 1.1A); (b) one-dimensional nanostructures (1-D), where two dimensions are confined in the

range of nanometers, this category includes nanotubes and nanowires (Figure 1.1B); and (c) two-dimensional nanostructures (2-D), where one dimension is confined in the nanoscale range, for example, quantum wells (Figure 1.1C) and grain boundary films (Shchukin, Ledentsov, & Bimberg, 2003).

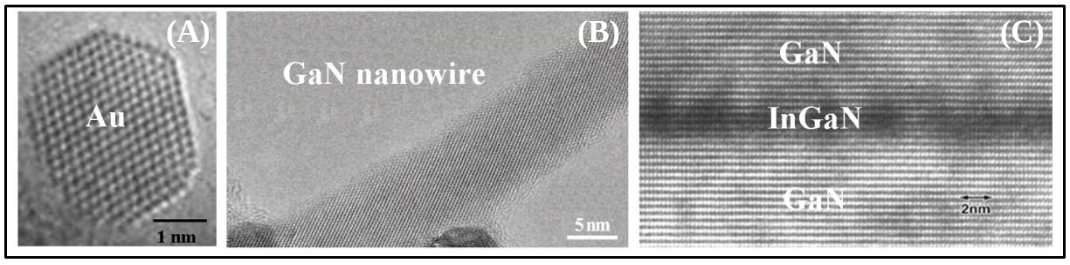

Figure 1.1 Examples of 0-D, 1-D, and 2-D nanostructures. (A) Au nanoparticle (Jefferson, 2008), (B) GaN nanowire, (C) InGaN quantum well (Ponce, et al., 2003).

The work in this thesis focuses on the growth of semiconductor nanowires. Thus, a detail description of growth, properties, and applications of semiconductor nanowires will be given in Chapter 3.

1.2.2 Nanostructure properties

The unique properties of nanostructures can be separated into two categories – surface-related effects and quantum confinement effects. Surface effects arise because atoms at the surface of a crystalline solid experience a different chemical environment than other atoms, changing their behavior (Cao, 2004). Quantum effects occur when the de Broglie wavelength of the valence electrons is of the same order as a size of the nanostructure material itself (Daniel & Astruc, 2004).

In bulk materials, the proportion of surface atoms to bulk atoms is entirely negligible and processes that take place at the surface of a material do not have any effect on the behavior of the material as a whole. However, the surface-to-volume ratio of nanostructures is considerably higher, high enough that physical properties are very different from those in bulk materials. The main effect of a large surface area is the increase of surface free energy, which increases the reactivity of the surface. The increase in surface area and surface free energy leads to changes in the structure and chemistry of the material. One of these changes is the decrease in interatomic distance. This is the case, for example, of copper metallic clusters, where the interatomic distance is observed to decrease with decreasing cluster size (Figure 1.2). Also, a large surface area leads to the stabilization of metastable structures or the simple relaxation of the normal crystalline lattice to try to accommodate the high proportion of surface atoms. For example, gold nanoparticles adopt a polyhedral shape instead of the usual cubic structure in the bulk (Brydson & Hammond, 2005). Also, the melting temperature of materials is affected by the large surface area. For instance, the melting point of Au has been observed to decrease by approximately a factor of two when the particle size is reduced from 10nm to 2nm, as seen in Figure 1.3 (Buffat & Borel, 1976).

Quantum size effects occur, as indicated before, when the wavelength of the electrons in a material is of the same order of at least one dimension of the

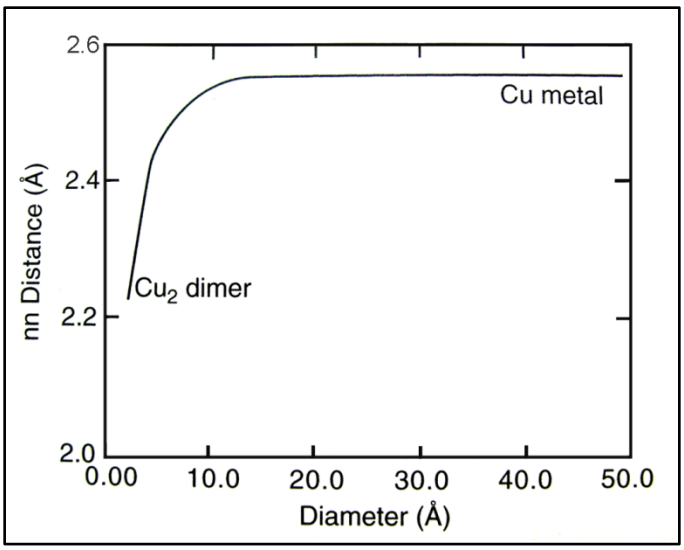

Figure 1.2. Schematic diagram showing the variation in the nearest-neighbor (nn) distance as a function of cluster size or particle size for copper (Brydson & Hammond, 2005).

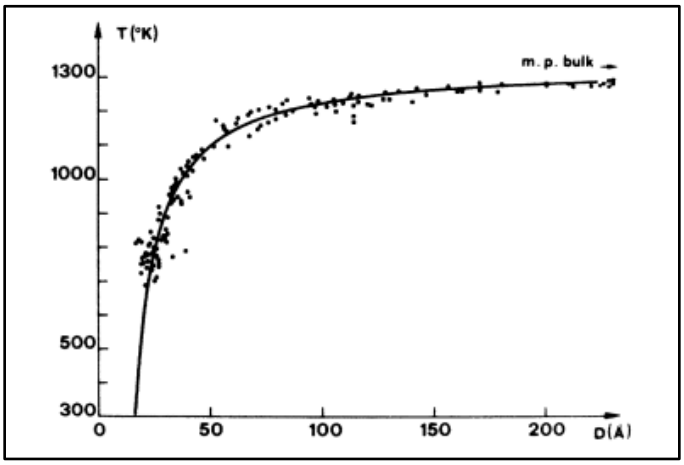

Figure 1.3. Schematic diagram showing the decrease in the melting point of gold nanoparticles as a function of particle size. •: experimental values and solid line: theoretical approximation (Buffat & Borel, 1976).

material. In the free electron model, the energies of the electronic states as well as the spacing between successive energies depend on $\boldsymbol{1/a^2}$ where $\boldsymbol{a}$ is the

dimension of the system in a particular direction. Thus, the energies and energy separations of individual electronic states will be very different at the nanoscale. As a consequence, the allowed energy bands become substantially narrower than in an infinite solid and the discrete nature of the energy states becomes more apparent at the nanoscale, although a fully discrete energy spectrum is only observed in systems that are confined in all three dimensions, for example, quantum dots. Figure 1.4 is a schematic representation of the energy bands in a bulk semiconductor, and the discrete energy levels in a quantum dot and a single atom (Shchukin, Ledentsov, & Bimberg, 2003). The discrete nature of the energy states in nanostructures causes a distortion in the electronic properties and the electrons tend to behave more like a 'particle in a box', i.e., the motion of the electrons is limited in the confining dimension of the material and become quantized (Brydson & Hammond, 2005). In addition, as the size of the nanostructure is decreased the band gap of the material is increased (or blue-shifted). Thus, quantum confined structures exhibit spectral tunability allowing the emission wavelength to be tuned simply by changing their size.

Additionally, the density of states of the electrons is strongly affected by the number of dimensions in which electrons are quantized (Weisbuch & Borger, 1991). The density of states is proportional to $\boldsymbol{E}^{(n-2)/2}$, where $\boldsymbol{E}$ is the energy of an individual electronic state and $\boldsymbol{n}$ is the number of dimensions in which the electrons are quantized. Hence, in the case of semiconductor materials, the

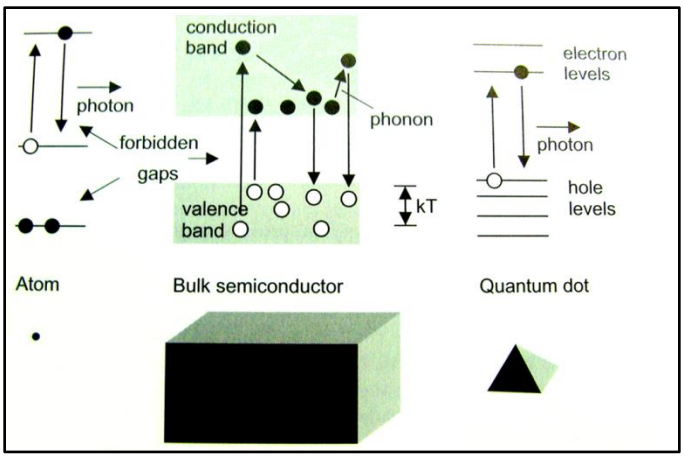

Figure 1.4. Schematic of energy levels in an atom, bulk semiconductor, and a quantum dot (Shchukin, Ledentsov, & Bimberg, 2003).

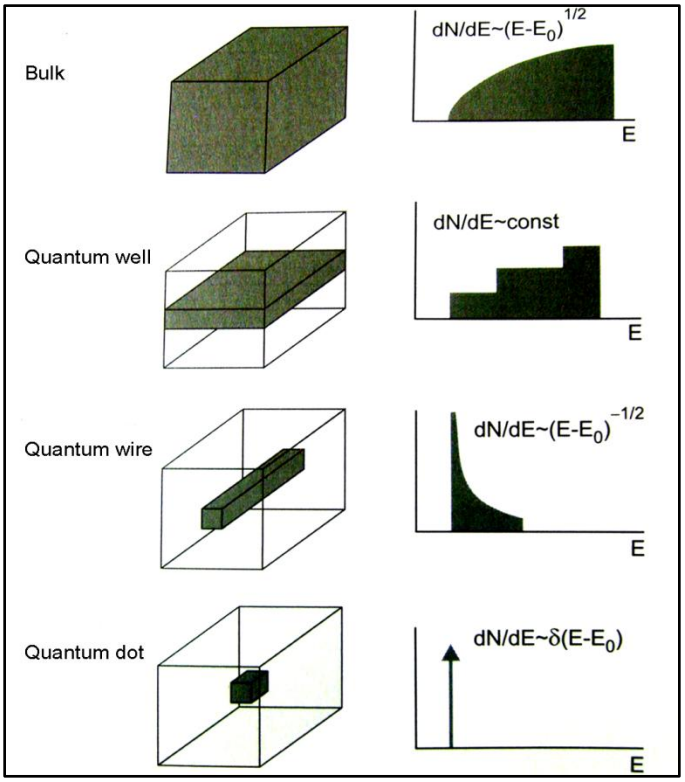

Figure 1.5. Schematic of semiconductor structures and corresponding electronic density of states (Shchukin, Ledentsov, & Bimberg, 2003).

density of states of the conduction band changes for 2-D, 1-D, and 0-D nanostructures as depicted in Figure 1.5.

Many of the electronic and optical properties of nanostructures are strongly affected by quantum size effects. For example, gold nanoparticles exhibit semiconductor properties in contrast with bulk gold that is metallic. Also, colloidal solutions of gold nanoparticles show a deep red color that becomes progressively more yellow as the particle size increases. Figure 1.6 shows optical absorption spectra of gold nanoparticles of varying sizes (Brydson & Hammond, 2005).

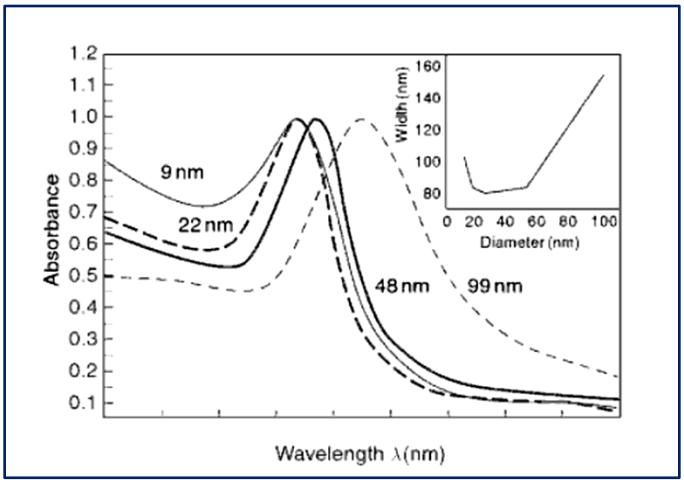

Figure 1.6. Size dependence of the optical absorption wavelength for gold nanoparticles and (inset) the corresponding value of the full width at half maximum (FWHM) of the absorption peak (Brydson & Hammond, 2005).

1.2.3 Fabrication methods of nanostructures

Nanostructures can be fabricated in different ways. As mentioned before, all the different fabrication methods can be classified roughly into either those which construct from the top down using processes that involve the removal of

atoms to create a desired nanostructure, or those which build from the bottom up, atom by atom until the nanostructure is formed.

1.2.3.1 Top-down approach

In this approach, nanostructures with appropriate properties are fabricated from bulk materials by a combination of lithography, etching and deposition. This approach has proven to be highly effective for the last 60 years in the electronic industry, which has been fabricating smaller and smaller devices.

Conventional lithographic processes can be used to create nanostructures by the formation of a pattern on a substrate via the creation of a resist on the substrate surface. Lithographic methods use either visible or ultraviolet (UV) light, X-rays, electrons or ions to project an image containing the desired pattern onto a surface coated with a photoresist material. The resist material, typically a polymer, metal halide, or metal oxide, undergo structural or chemical modification during irradiation, often altering the solubility of the exposed resist. In a positive resist, irradiated areas are dissolved as they are more soluble than unexposed materials, whilst in a negative resist irradiated areas are insoluble (Figure 1.7). The resist can then be used as a template, or as an etch-mask, for subsequent deposition onto, or etching of, the underlying substrate (Brydson & Hammond, 2005).

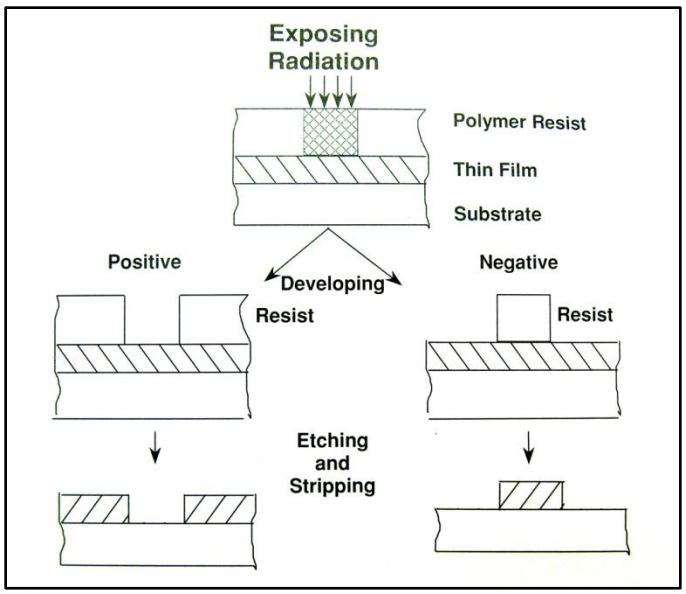

Figure 1.7. Schematic of positive and negative resists.

An important consideration when fabricating nanostructures by lithography is the ultimate resolution of the lithographic technique. Fundamentally the wavelength of the radiation used in the lithographic process determines the size of pattern imprinted on the resist and hence the final nanostructure size. Typically the resolution ranges from a few hundred of nanometers for optical techniques to tens of nanometers for electron beam techniques (Brydson & Hammond, 2005). As device features get smaller, the size of their nanostructure components is pushed to the atomic regime and conventional lithographic methods face fundamental challenges. Thus, in order to overcome these challenges, a broader range of patterning techniques than the UV or optical projection methods are needed to enable ultimate atomic resolution, lower cost, and application to a broader range of materials and surface geometries (Harriot & Hull, 2004).

1.2.3.2 Bottom-up approach

Nature has been successfully creating live organisms from the bottom-up for millions of years. Although current research is nowhere close to this level of fabrication, the bottom-up approach sort of mimics nature's way of self-assembling atoms to form nanostructures in three dimensions.

Bottom-up techniques involve controlled crystallization of nanostructures, with sizes near atomic scale, from vapor or liquid sources. These techniques are astonishingly precise and usually produce uniform and highly ordered crystalline nanostructures. The precision in which this approach synthesizes nanostructures goes beyond that achievable with top-down methods, and even though the bottom-up approach is still fairly new, it has the potential to enable devices with unique features and new functional systems and thereby create innovative technologies. Lu and Lieber (2007) reviewed different nanoelectronic applications fabricated from the bottom-up. In this review, they presented some work done on electromechanical and resistance-change memory devices based on carbon nanotubes and core-shell nanowires structure respectively among other nanoelectronic examples.

Different bottom-up methods have been developed in order to synthesize nanostructures materials in the last decades. In particular, vapor phase deposition techniques use some sort of energy to evaporate or decompose a solid or liquid source, the resulting vapor atoms are deposited on a substrate, where they diffuse and either leave the substrate or nucleate to form a solid cluster. Eventually, the

nanostructure grows epitaxially from this cluster. A more detailed description of epitaxial growth will be given in Chapter 3.

Usually vapor phase deposition techniques are used to fabricate different nanostructures such as thin films, nanowires, quantum dots, nanoparticles, etc. These techniques can be classified roughly depending on the method to evaporate or decompose the solid or liquid source into vapor. Thus, methods that involve purely physical process are part of the physical vapor deposition (PVD) variety and those methods that involve chemical reactions are part of the chemical vapor deposition (CVD) processes.

Examples of PVD conversion processes are thermal evaporation, such as resistive or electron beam heating, laser ablation or pulsed laser deposition, where a short nanosecond pulse from a laser is focused onto the surface of a bulk target, and sputtering, in which the removal of a target material is done by bombardment the target with ions. Examples of CVD process are molecular beam epitaxy (MBE) and metalorganic chemical vapor deposition (MOCVD), where usually chemical reactions or thermal decomposition of gas phases species occur at elevated temperatures, typically 500 ˚C – 1000 ˚C (Brydson & Hammond, 2005).

MBE and MOCVD are used extensively for the production of semiconductor nanostructures. In MBE, epitaxial, single atomic layers (0.2 – 0.3 nm) are grown on a heated substrate under ultra high vacuum conditions. Standard MBE uses elements in a very pure form as solid sources and after evaporation, the produced beams of atoms intersect at the substrate and deposit the appropriate semiconductor, atomic layer by atomic layer. In MOCVD, the

required elements are transported as components of gaseous compounds such as metal alkys and non-metal hydrides, e.g., trimethylgallium [$(CH_3)_3Ga$] (TMG) and ammonia (NH_3,), into a suitable chamber where they flow over the surface of a heated substrate. These compounds break down and react so as to deposit the relevant semiconductor (Brydson & Hammond, 2005).

Both techniques, MBE and MOCVD, have their advantages and disadvantages, for example, solid-source MBE is capable of growing sharp interfaces between adjacent layers, and the slow growth rates gives precision in layer thicknesses. On the other hand, the high growth rate of MOCVD is more appropriate for commercial production, as well as its ability to scale up to larger systems, permitting simultaneous growth on multiple substrates.

1.3 Semiconductor materials

Even though research and development in nanotechnology covers a broad range of materials, much of the interest and research funding is centered in semiconductor materials. Semiconductors and devices based on them play an important role in modern life. From personal computers to video game consoles, from solar cells to worldwide satellite phones, semiconductors contribute to everyday life like no other manmade material. In particular semiconductor nanostructures offer a wide range of unique properties, which can be used to produce superior and innovative electronic devices. This section reviews relevant semiconductor physics and continues with a short description of common semiconductors and their applications.

1.3.1 Introduction to band theory of solids

In an isolated atom, each electron orbital has a set of stable energy levels. When two atoms come together, the outer electrons – valence electrons – become responsible for the bonding between the atoms. Upon bonding the atomic energy levels split into bonding and anti-bonding molecular orbital. The molecule can exists as more bonding orbitals are filled with electrons when compared with anti-bonding orbitals. When more atoms come together to form a solid, more molecular orbitals are generated and gradually they overlap to form broad energy bands. These bands contain allowed energy levels and they are separated by forbidden energy regions, band gaps, where electrons are not allowed to occupy (Figure 1.8). Those bands in which the outer electrons are present are called the valence bands. The valence bands can be partially or completely full of outer electrons and these bands determine the electronic behavior of a solid in a variety of circumstances.

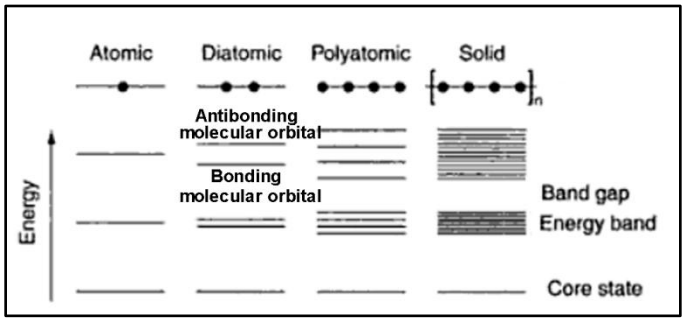

Figure 1.8. Electron energy level diagram for a single atom, a diatomic molecule, a polyatomic molecule, and a solid. This diagram shows the broadening of molecular orbitals into energy bands for a one dimensional solid (Brydson & Hammond, 2005).

An alternative approach to understand electronic band structure in solids is to consider the wave nature of electrons and the interaction of these waves with the periodic crystalline potential of the solid. In simple terms, the starting point of this approach is the Drude-Lorentz free electron model (Ashcroft & Mermin, 1976) where the energy $\boldsymbol{E}$ of a free electron varies linearly with $\boldsymbol{k^2}$, where $\boldsymbol{k}$ is the wave vector and can take all possible values. In the Kroning-Penney model, the electron now is considered to be in a periodic potential associated with a crystal with a unit cell dimension $\boldsymbol{a}$. Electron waves with a wave vector $\boldsymbol{k=n\pi/a}$ cannot propagate through the crystal because they undergo Bragg reflection. Both forward and backward travelling waves exists in the lattice, and the superposition of these creates standing waves. Thus, two standing waves exist at $\boldsymbol{k=n\pi/a}$ and they have different associated energies. Consequently, a band gap forms in the energy curve at the corresponding values of wave vectors: $\boldsymbol{k=n\pi/a}$, as shown in Figure 1.9. The region between any two diffraction conditions, that is, between $\boldsymbol{-n\pi/a}$ and $\boldsymbol{+n\pi/a}$, is known as Brillouin zones (BZ). In a real crystal, i.e., a three dimensional crystal, the BZ are described by complex surfaces in three dimension, for example the BZ of silicon are shown in Figure 1.10 A . The electron energy band diagram is mapped for different directions of the Brillouin zone as shown in Figure 1.10 B for silicon. A more detailed description of this approach can be found in Ashcroft's textbook (Ashcroft & Mermin, 1976).

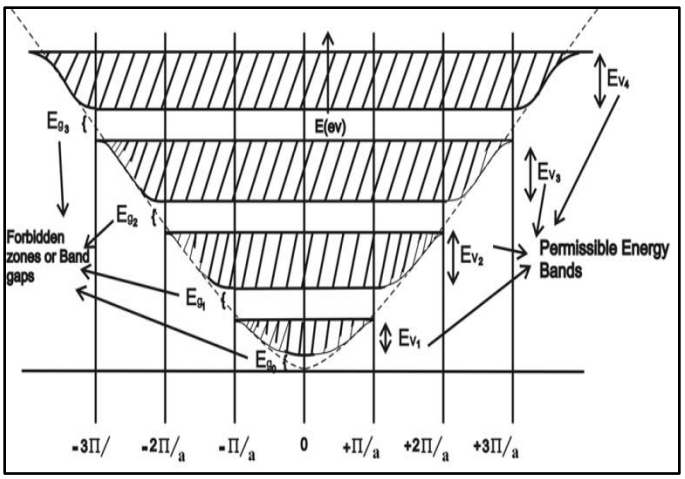

Figure 1.9. Energy band diagram of electrons in a crystalline solid following the Kronig-Penny model. The interruption of the E-k diagram appears at k=nπ/a due to Bragg reflections (Sharma B. K., 2010).

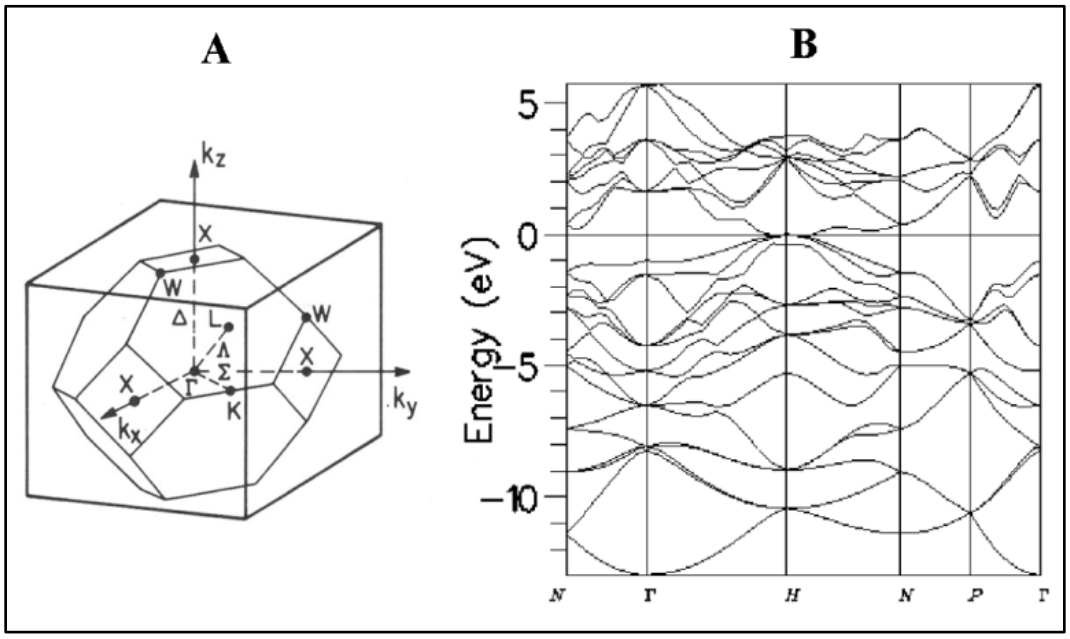

Figure 1.10. (A) Brillouin zone (Ullrich, 2001) and (B) energy band structure diagram (Clark, 1996) for crystalline Si.

1.3.2 Difference between metals, insulators, and semiconductors

The electronic band structure of a solid determines if the solid behaves as an insulator, a metal, or a semiconductor. In insulators, the valence band is fully occupied with outer electrons and the energy gap between the conduction and the valence band is very large. Electrons in the valence band are unlikely to acquire enough energy to go to the conduction band. Because of the lack of vacancies in the valence band and electrons in the conduction band, the solid do not conduct electricity. In metals, the valence band and the conduction band are only half-filled or the conduction band overlaps with the valence band; in either case vacant energy states are available and electrons can easily move through the solid, as a result the solid exhibit conductivity.

In semiconductors, there is a relatively small band gap between the valence band and conduction band. The energy states within the valence band are also fully occupied and at absolute zero temperature (0 K) electrons are not free to move about the solid – thus, semiconductors behave as insulators at this temperature. However, electrons from the valence can move into the bottom of conduction band by absorbing the energy of a photon or a phonon. Electrons in the conduction band are free to move because of the large amount of vacancies and the vacancies, holes, left on the valence band are also free to move about the band, contributing both to the electrical conductivity. When an electric field is applied, both electrons and holes can move in their respective bands, leading to electrical conduction (Mahajan & Harsha, 1998). There is no set band gap width

that determines whether a material is an insulator or a semiconductor so the distinction is usually made in the way the materials is used.

1.3.3 Classification of semiconductor materials

Semiconductors can be roughly classified into those having direct or indirect band gap. In direct band gap semiconductors, the minimum in the conduction band and the maximum in the valence band have the same ***k*** value. Thus when electrons make a transition from one band to the other one, the wave vector is conserve as well as the energy by the absorption or emission of a photon. On the other hand, in indirect band gap semiconductors, the lowest energy state in the conduction band and the highest energy state in the valence band have different ***k*** values. Electronic transitions are possible, but usually involve an additional intermediate step such as the emission or absorption of a phonon. These transitions are relatively slow, hence other processes, known as non-radiative processes, might occur without allowing the emission of a photon. This makes indirect band gap semiconductors unsuitable for light production.

The majority of binary semiconductors consisting of elements from the group three and five have direct band gap. Examples of III-V semiconductor include gallium arsenide (GaAs), gallium nitride (GaN), indium nitride (InN), and indium phosphide (InP). These semiconductors have good light production efficiency, hence they are suitable for many optoelectronic applications. Also, group II-VI semiconductors such as cadmium telluride (CdTe), zinc selenide (ZnSe), and zinc oxide (ZnO) have direct band gap. Additionally, also ternary compounds such as indium gallium nitride ($In_xGa_{1-x}N$) or gallium indium arsenide

($Ga_xIn_{1-x}As$) have a direct band gap and are used for optoelectronic applications. Examples of indirect band gap semiconductors include Si, germanium (Ge), and aluminum arsenide (AlAs). Even though Si is unsuitable for light production, it is the basis for the majority of purely electronic devices due to its superior temperature performance, naturally-forming native oxide (that acts as an insulating barrier) and high natural abundance. Figure 1.11 shows a schematic of energy band diagrams for GaAs and Si with the allowed electron energies versus the electron wave vector *k* and the direct and indirect transitions (black arrows).

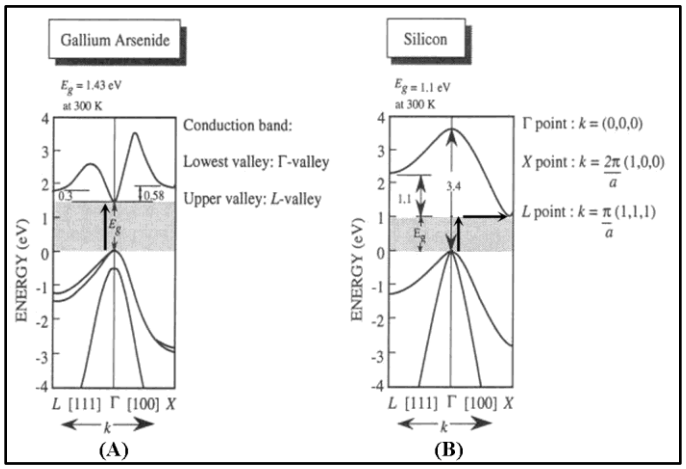

Figure 1.11. Schematic of the energy band diagrams for GaAs and Si with the allowed electron energies versus the electron wave vector k and the direct and indirect transitions (black arrows) (Mahajan & Harsha, 1998).

The electrical properties of a semiconductor may be modified by the introduction of impurity atoms – dopants – into the lattice. Either extra electrons or extra holes can be introduced when introducing dopants into the lattice. If the excess carriers are electron, the doped semiconductor is called n-type. If the excess carriers are holes the semiconductor is called p-type (Mahajan & Harsha,

1998). These semiconductors are called extrinsic semiconductors. On the other hand, when the electrical conductivity of a semiconductor depends only on the thermally generated electrons and holes, the semiconductors are called intrinsic semiconductors.

1.3.4 Semiconductor applications

Semiconductor devices such as LED's and solar cells consist of the junction of a p- and n-type semiconductor or the junction of a metal with either a p- or n-type semiconductor. The principles of p-n junctions can be found in Mahajan and Harsha textbook (1998). The main feature of a p-n junction is that upon forward voltage the minority carriers are injected across the junction, resulting in an increased junction current. When a forward bias is applied to LEDs, additional electrons and holes are injected as minority carriers across the junction, where they recombine realizing photons with energies of the same magnitude as the band gap of the semiconductor. Thus, for example, GaAs based LEDs emit infrared light, while GaN, AlN and InGaN LEDs emit green, UV, and violet light respectively. When a solar cell is illuminated with radiation with energy greater than the bandgap of the semiconductor, a forward voltage is generated across the junction. Solar cells have been fabricated for the last 35 years, currently the record of efficiency is 42.8% for an InGaN multijunction based solar cell. Commercial solar cells are based on GaAs, CdTe or Si thin films but their efficiencies are really low (from 11% to 20%).

The ability to fabricate semiconductor nanostructures that emit and absorb light at a range of specific wavelengths, from the infrared through the visible to

ultraviolet spectral regions, opens up a wide range of optoelectronic applications. However, the precise control needed to fabricate semiconductor nanostructures with specific characteristics only will be achieved when a complete understanding of their properties is accomplished.

1.4 Overview of this thesis

The work in this thesis focuses on understanding the growth processes involve during the formation of GaN nanowires. Thus, Chapter 2 reviews fundamental properties and characteristics of GaN. Chapter 3 presents a general review on growth of semiconductor nanowires as well as their properties and applications. As mentioned before, the growth of GaN nanowires was observed *in situ* and controlled in real-time using an environmental transmission electron microscope. Thus, Chapter 4 reviews important characteristic of *in situ* electron microscopy, in particular environmental transmission electron microscopy, and also presents a review of the characterization methods, gold deposition technique, and gas precursors used in this thesis. Finally, Chapter 5, and 6 present experimental results and conclusions on the nucleation and growth of GaN nanowires.

CHAPTER 2

FUNDAMENTAL PROPERTIES OF GaN

For the last forty years or so, GaN and its alloys with AlN and InN have attracted considerable interest for their applications in a number of optoelectronics devices, such as light emitting diodes, photovoltaics, solid state lasers, and ultraviolet detectors, as well as high-power and high-temperature electronic devices. This chapter aims to provide a short overview of the exceptional properties and characteristics that made GaN and its compounds such interesting materials.

Growth of GaN crystal was first reported in 1932 by Johnson, Parsons and Crew (1932). The method consisted of the simple conversion of Ga metal into GaN in the presence of NH_3. In the late 1960s, GaN was introduced to the semiconductor community when Maruska and Titjen developed a hydride vapor-phase epitaxy method for the growth of GaN on a sapphire substrate (1969). The epitaxial layers were naturally n-type with high background carrier concentration in the range of 1 to 5 x 10^{19} cm^{-3} attributed to nitrogen vacancies. Later, Pankove and colleagues (1971) managed to develop the first blue, green, yellow, and red LEDs with a metal-insulator-n-type GaN structure. The same year, Manasevit and colleagues (1971) succeeded in synthesizing GaN epitaxial films and needles by MOCVD for the first time. In these early stages, the main issues when trying to develop GaN-based devices were the inability to reduce the high background of electron concentration as well as achieve p-type GaN without generating more defects, and also the difficulties to grow smooth GaN epitaxial films as well as

AlGaN and InGaN alloys. These issues were not overcome for many years, and the interest in GaN and its related compounds decreased. More than a decade later, Amano and Akasaki (1986) successfully grew for the first time smooth GaN films using a low temperature AlN buffer layer by MOCVD. Few years later, they also developed p-type GaN with Mg-doping followed by an ex-situ low energy electron beam irradiation (LEEBI) treatment (Amano, Kito, Hiramatsu, & Akasaki, 1989). The high p-type carrier density (~ 10^{16} cm^{-3}) was sufficient to produce the first p-n junction blue LEDs which were also reported in the same papers. Few years later, Nakamura and colleagues at Nichia Chemical Industries were able to increase the p-doping using thermal annealing after growth (Nakamura, Mukai, Senoh, & Iwasa, 1992). They also developed thin quantum wells of InGaN and AlGaN with improved quality and superior performance and they formed the basis for bright blue and green commercial LEDs (Nakamura, Mukai, Senoh, Nagahama, & Iwasa, 1993) (Nakamura, Mukai, & Senoh, 1994) (Nakamura, Mukai, & Senoh, 1994). Also, the same group reported pulsed room-temperature operation of an AlGaN/GaN/InGaN injection laser (Nakamura, et al., 1996). Since these outstanding achievements were realized, GaN and related compounds have been available to produce remarkable light emitting devices.

2.1 Crystal structure of GaN

Under ambient conditions, the thermodynamically stable crystal structure is wurtzite (WZ) for bulk GaN. The zincblende (ZB) structure was also observed when growing thin films on {011} crystal planes of cubic substrates such as Si, MgO, and GaAs (Morkoc, 1999). Also, under high-pressure conditions (50 GPa),

a phase transition from wurtzite to rock salt has been observed (Gorczyca & Christensen, 1993).

The wurtzite structure has a hexagonal unit cell with ***a*** and ***c*** components. It contains six gallium atoms and six nitrogen atoms. The space group for this structure is $P6_3mc$ (C^4_{6v}). The wurtzite structure consist of two interpenetrating hexagonal close packed sub-lattices, each sub-lattice being occupied by either gallium or nitrogen atoms, offset along the c-axis by 5/8 of the cell height (5/8 c). In the case of Ga polarity, the gallium atoms are located at (0, 0, 0) and (2/3, 1/3, 1/2), while the nitrogen atoms are located at (0, 0, 3/8) and (2/3, 1/3, 7/8). A schematic representation of the wurtzite structure is shown in Figure 2.1.

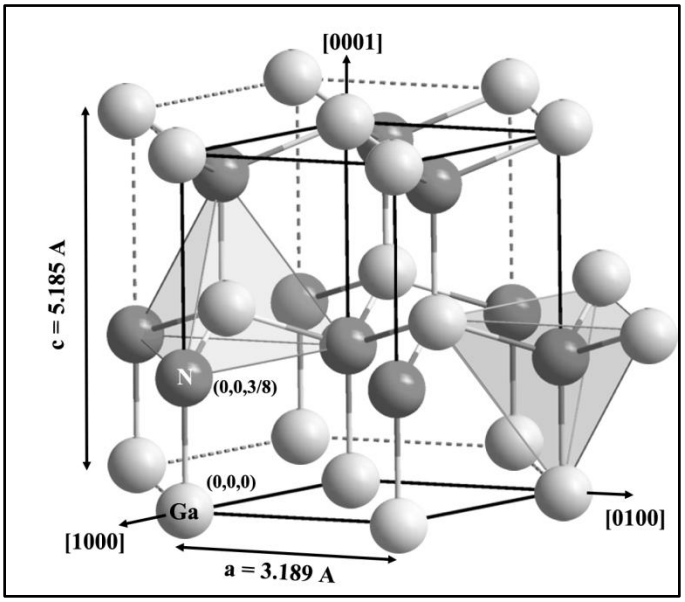

Figure 2.1. Schematic representation of wurtzite structure for GaN

The zincblende structure has a cubic unit cell, containing four gallium atoms and four nitrogen atoms. The space grouping for the zincblende structure is F-43m (T^2_d). The position of the atoms within the unit cell is identical to the

diamond crystal structure. The structure consists of two interpenetrating face-centered cubic lattices, offset by one quarter of the distance along a body diagonal (Figure 2.2). Each atom in the structure may be viewed as positioned at the center of a tetrahedron, with its four nearest neighbors defining the four corners of the tetrahedron.

The rock salt structure is face centered cubic and for GaN also contains equal amounts gallium and nitrogen. The space group for the rock salt crystal structure is Fm-3m. A schematic representation of this structure is shown in Figure 2.3.

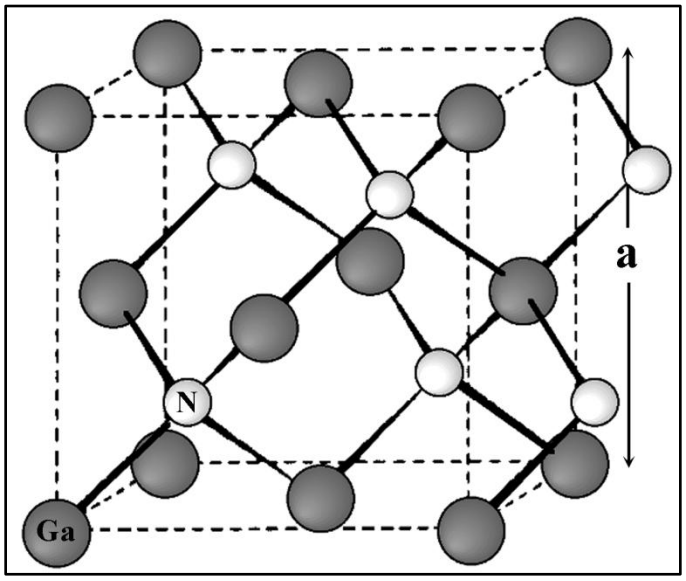

Figure 2.2. Schematic representation of the zincblende structure for GaN

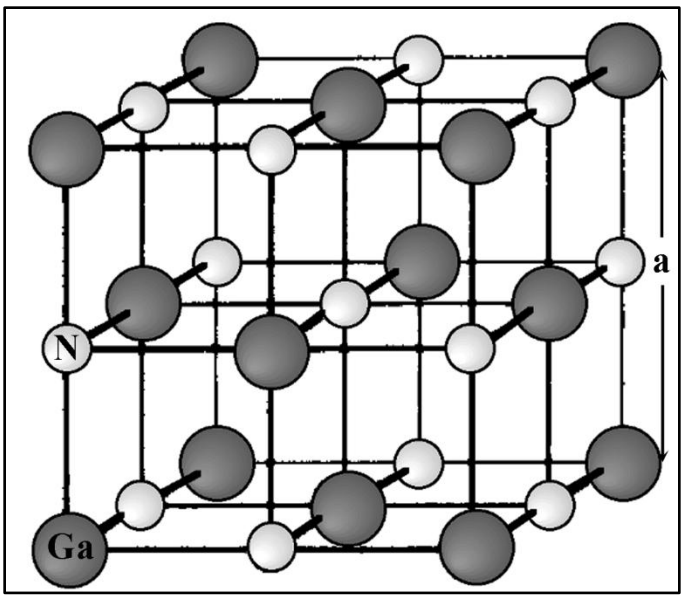

Figure 2.3. Schematic representation of the rocksalt structure for GaN

At room temperature, the measured values of lattice parameters for the wurtzite GaN are $\boldsymbol{a_o}$= 3.189 Å and $\boldsymbol{c_o}$= 5.186 Å (Lagerstedt & Monemar, 1979). The measured values for the zincblende polytype is $\boldsymbol{a}$ = 4.520 Å. A high-pressure phase transition from the wurtzite to the rock salt structure has been predicted and observed experimentally (Mohammad & Morkoc, 1996). The transition point is 50GPa and the experimental lattice constant in the rocksalt phase is $\boldsymbol{a}$ = 4.22 Å.

The wurtzite and zincblende structures are similar. Both crystal structures are held together by tetrahedral bonds between the atoms (Figure 2.4 A and B). Thus, each gallium atom is coordinated by four nitrogen atoms and vice versa. These structures differ only in the bond angle of the second-nearest neighbor, which generates two different stacking sequences of the closest packed diatomic planes. The growth most often occurs in direction of the closest packed diatomic planes, i.e., the <0001> directions in the hexagonal cell of the WZ structure and

the <111> directions in the cubic cell of the ZB structure. Thus, the stacking sequence for the WZ structure is **AaBbAaBbAaBb** in the <0001> direction (Figure 2.4 C), where **Aa** and **Bb** are two distinct layers of gallium-nitrogen pairs; and the stacking sequence for the zincblende structure is **AaBbCcAaBbCcAaBbCa** in the <111> directions (Figure 2.4 D).

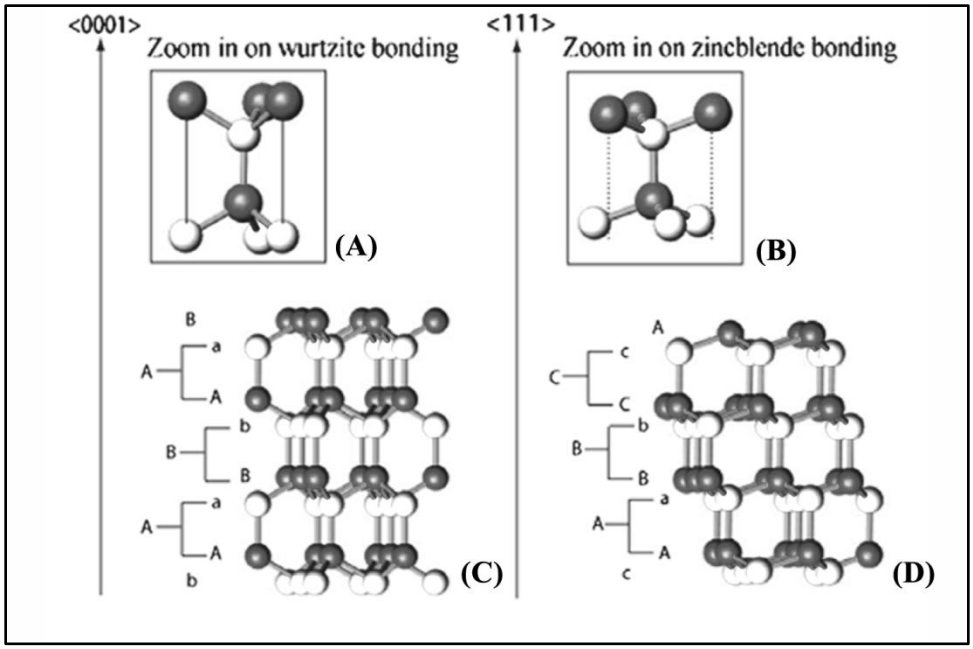

Figure 2.4. Stick and ball representation of the (A, C) wurtzite and (B, D) zincblende structure in the <-110> viewing direction. (a) and (b) showed the bonding configuration in the ZB and WZ structures. The upper and lower cases in (c) and (d) indicate layers of gallium (grey) and nitrogen (white) atoms (Dick, et al., 2010).

The nomenclature for various commonly used planes and directions of hexagonal semiconductors in three-dimensional versions is presented in Figure 2.5 (Morkoc, 1999).

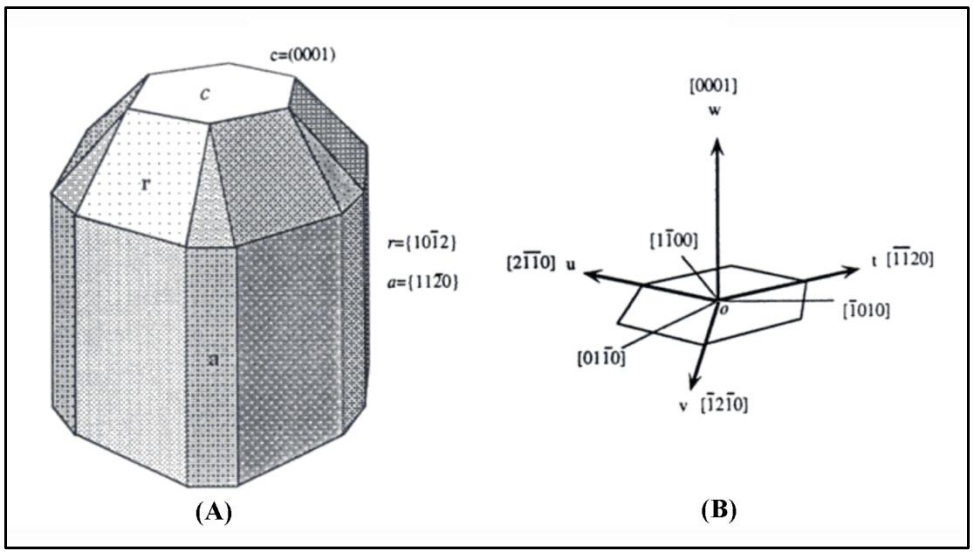

Figure 2.5. Three-dimensional schematic view of commonly used planes and directions in a crystal with hexagonal symmetry

Another important thing to note is that the bonding in GaN has both covalent and an ionic character. It is common to quantitatively define the ionic character of the bond by the Phillips ionicity, f_i, of the crystal, where f_i is zero for perfectly covalent bond and one for perfectly ionic bond (Phillips, Ionicity of chemical bond in crystals, 1970). Thus, the values for wurtzite GaN and zincblende GaN are $f_i = 0.500$ and $f_i = 0.519$ respectively (Ferhat, Zaoui, Certier, & Khelifa, 1996). The ionic nature of the bond causes planes that have uneven number of gallium and nitrogen atoms.

2.2 Fundamental properties of GaN

One of the special characteristics that makes GaN attractive for light emitting devices and photovoltaic applications is its direct bandgap of 3.42 eV (at 300 K). Also, GaN can alloy with InN and AlN over the whole composition range to form ternary, or quaternary, compounds with bandgap energies ranging

from 0.7 eV (infrared) to 6.2 eV (ultraviolet) as shown in Figure 2.6. This provides the possibility of bandgap engineering over the entire visible spectrum which is essential for producing any specific wavelength emitters or collectors. Important electronic properties of WZ and ZB GaN are listed in Table 2.1.

Table 2.1. Electronic properties of GaN (Levinshtein, Rumyantsev, & Shur, 2001)

Electronic Properties	*Wurtzite GaN*	*Zincblende GaN*
Electron mobility at 300 K ($cm^2/V•s$)	≤ 1000	≤ 1000
Hole mobility at 300 K($cm^2/V•s$)	≤ 200	≤ 350
Effective electron mass (m_o)	0.20	0.13
Effective hole mass (m_o)		
Heavy	1.4	1.3
Light	0.3	0.2
Electron affinity (eV)	4.1	4.1
Diffusion coefficient (cm^2/s)		
Electrons	25	25
Holes	5	9
Electron thermal velocity (m/s)	2.6×10^5	3.2×10^5
Hole thermal velocity (m/s)	9.4×10^4	9.5×10^4

Another interesting feature is their stronger chemical bonds relative to the other compound semiconductors which makes the material very stable and

resistant to high electrical currents and intense light illumination, resulting in devices thermally more stable with longer lifetime than with the conventional systems (Nakamura S. , 1998). The strong chemical bonds also makes it difficult to introduce dislocations once the material is grown, which is the main mechanism of degradation observed in other wide bandgap semiconductors (Mohammad, Salvador, & Hadis, 1995).

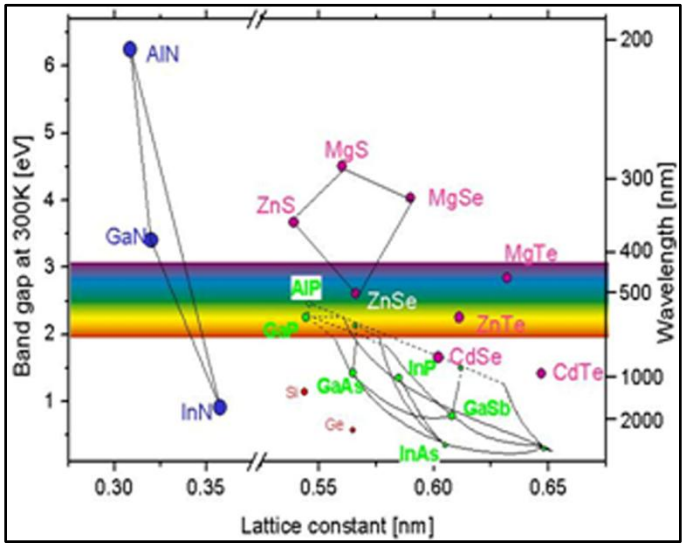

Figure 2.6. Schematic representation of band gaps vs lattice constant of compound semiconductors that emit in the visible range of the electromagnetic spectrum. The lattice constant or interatomic separation is related with bond strength. Thus, the group III-nitride semiconductors have stronger chemical bonds compare with other wide bandgap semiconductors which makes them thermally more stable (Lymperakis & Neugebauer, 2010).

Thermodynamic properties of WZ GaN have been reported by different authors and some of these properties are listed in Table 2.2.

Table 2.2. Thermodynamic properties of WZ GaN (Morkoc, 1999) (Adachi, 2005)

Thermodynamic properties	*Wurtzite GaN*
Theoretical melting temperature (K)	2791
Log (vapor pressure, p) (atm)	*5699 – 15 923/T*
Heat of sublimation (kcal/mol)	72.4 ± 0.5
Linear thermal expansion coefficient (K^{-1})	
Along a_o (over the range 300 – 900 K)	5.59 x 10^{-6}
Along c_o(over the range 700 – 900 K)	7.75 x 10^{-6}
Thermal conductivity at 300 K (W/cm K)	1.3
Debye temperature θ_D (K)	600
Heat capacity (J/mol K)	35.3
Specific heat at constant pressure *Cp(T)* (cal $mol^{-1}K^{-1}$)	9.1 + (2.15 10 -3 T)

A thorough description of the GaN phase stability has been reported by Unland et al. (2003). The calculated phase diagram for GaN is shown in Figure 2.7. Although this calculations show that GaN starts forming about 302.9 K, experimental results demonstrated that high-quality GaN epitaxial films are obtained at 1373 K.

2.3 Defects on GaN

GaN and related materials are rich in structural defects as well as point defects such as vacancies. The large lattice mismatch between the substrates and the epitaxial films generates high density of threading dislocations ~10^9 – 10^{10} cm^{-2} (Lester, Ponce, Craford, & Steigerwald, 1995). Unlike conventional

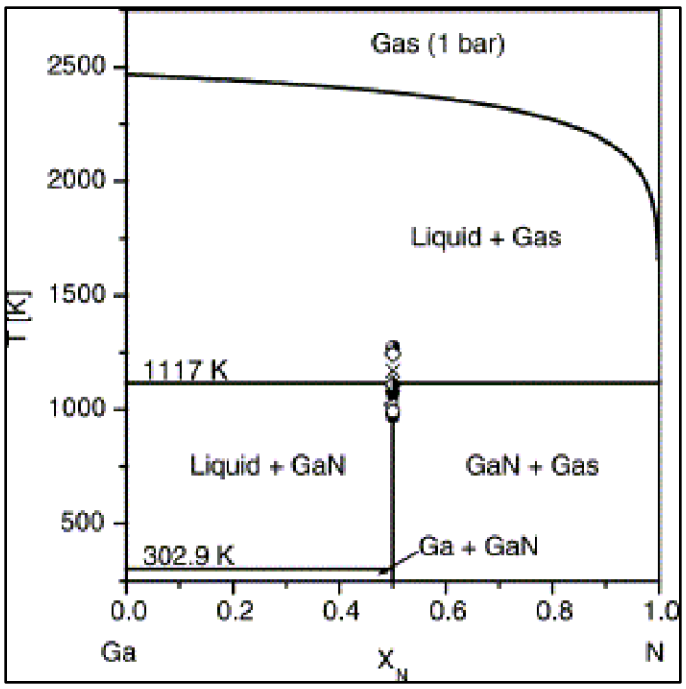

Figure 2.7. Section of the calculated phase diagram at 1 bar (750 Torr). According to calculations, above 1117K GaN decomposes into Ga_{liquid} and N_2. Experimental data are superimposed. Solid symbols denote solid GaN, open symbols denote GaN decomposed into liquid + gas.

epitaxial films, dislocations are rare in GaN nanowires (Inoue, Hoshino, Takeda, Ishino, Ishida, & Fujiyasu, 2004). Even when there is a mismatch between the substrate and the nanowires, the strain generated at the nanowires-substrate interface can be accommodated coherently without nucleation threading dislocations. However, other defects such as stacking faults or rotational twins can be randomly distributed in GaN nanowires and other compound semiconductor nanowires (Tham, Nam, & Fischer, 2006) (Dick, et al., 2010). These structural defects may introduce additional electronic states near the band

edges or act as electron scattering centers (Stiles & Hammann, 1990), thus, affecting the electrical and optical properties of nanowires (Bao, 2008).

In order to characterize the structure of the nanowires, it is important to emphasize the difference between a twin plane and a stacking fault. The majority of twin planes and stacking faults in the group-III nitrides lie on the (0001) basal planes for the WZ structure and on the (111) planes for the ZB structure. As mentioned before, the normal stacking sequence, in the directions of the basal planes, for the WZ and ZB structures are **AaBbAaBbAaBb** and **AaBbCcAaBbCcAaBbCc** (Figure 2.4 C and D), where uppercase and lowercase letters represent gallium and nitrogen atoms. In the WZ structure, misplacement of a single bilayer is defined as a stacking fault, resulting in stacking the sequence **AaBb<u>AaBb</u>|<u>Cc</u>BbCcBb** with the fault line between **Bb** and **Cc** (Figure 2.8). This automatically creates a single unit of ZB structure (**<u>AaBbCc</u>**) as shown in the shaded rectangle in Figure 2.8. Additionally, based on the number of single units of ZB structure, the stacking faults can be classified into three types: Intrinsic (I_1) with one ZB segment (**AB<u>AB</u>|<u>C</u>BCB**) (Figure 2.8), intrinsic (I_2) with two ZB segments (**AB<u>AB</u>|<u>C</u>|<u>A</u>CA)** (Figure 2.9 A), and extrinsic (E) with three ZB segments (**AB<u>AB</u>|<u>C</u>|<u>A</u>|<u>B</u>AB**) (Figure 2.9 B) (Hull & Bancon, 1984).

In the ZB structure, misplacement of a single bilayer creates a twin plane. A twin plane is defined as a mirror plane between two segments rotated by 60 ˚ from each other. The stacking sequence can then be written as **AaBbCc<u>Aa</u>CcBbAa**, the twin plane in this sequence is **<u>Aa</u>** as shown in Figure 2.10.

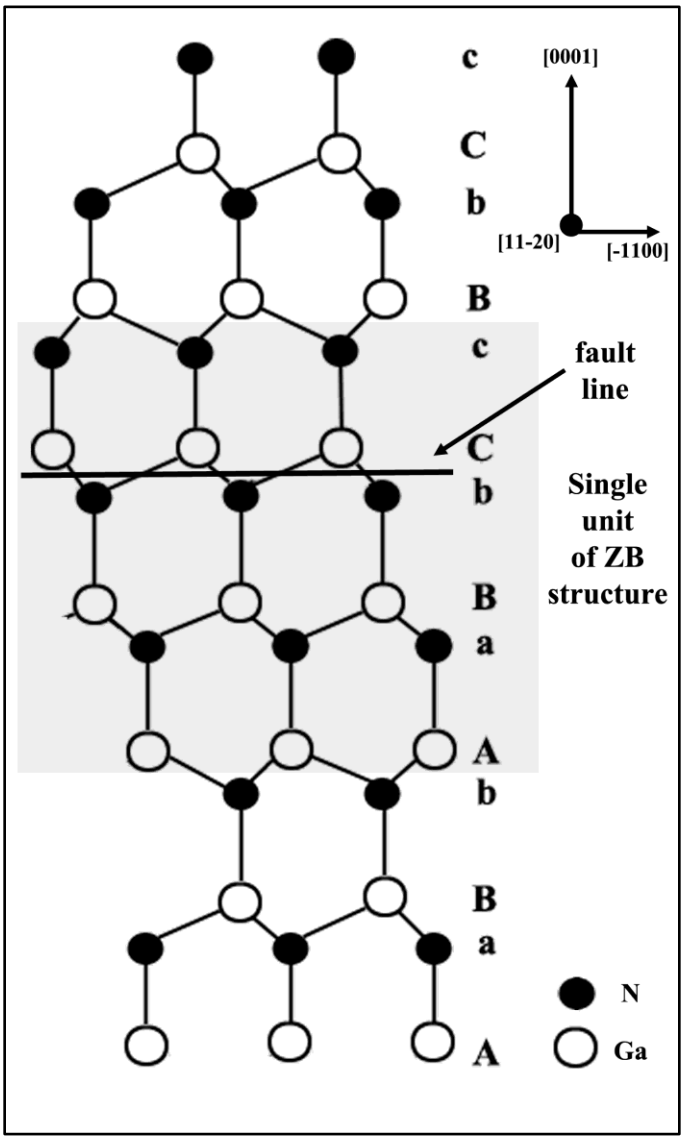

Figure 2.8. Stacking fault in the WZ structure along the [0001] direction. The stacking fault forms a single unit of the ZB structure (shaded rectangle). This stacking fault is also known as intrinsic I_1 stacking fault.

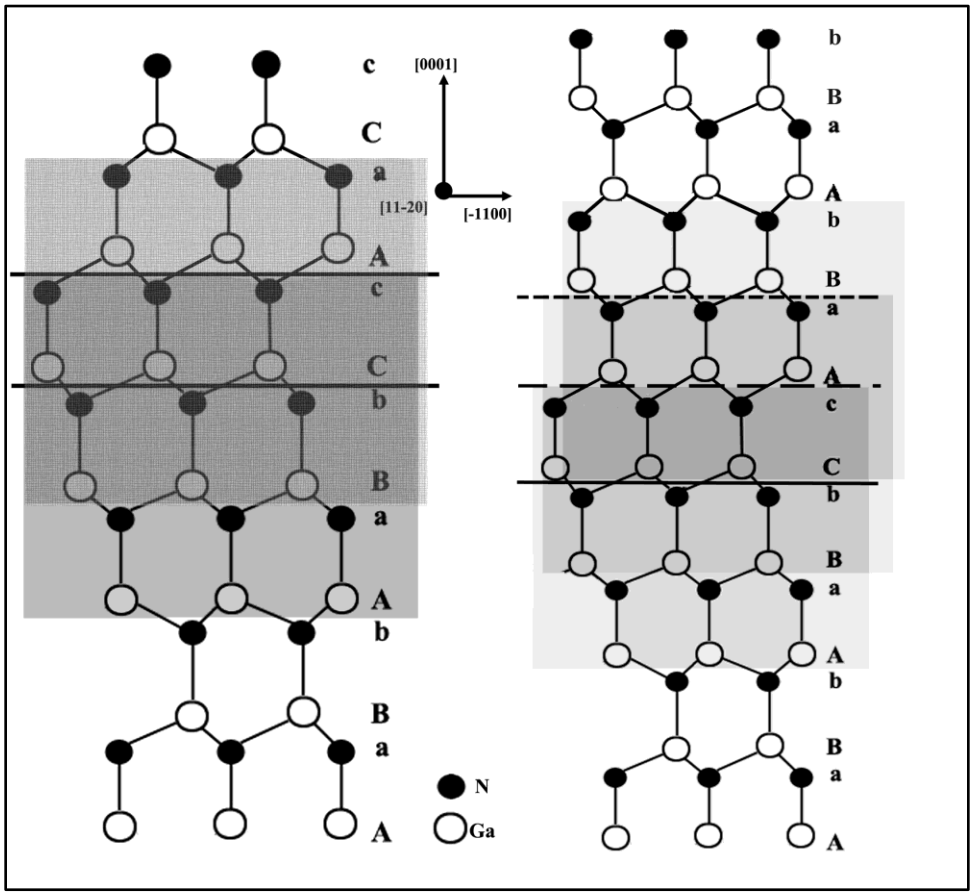

Figure 2.9. Stacking sequence of intrisic I_2 and extrinsic stacking faults along the [0001] direction for the WZ strcuture. Intrisic I_2 stacking fault has two single ZB units and extrinsic stacking fault has three ZB units (shaded rectangules).

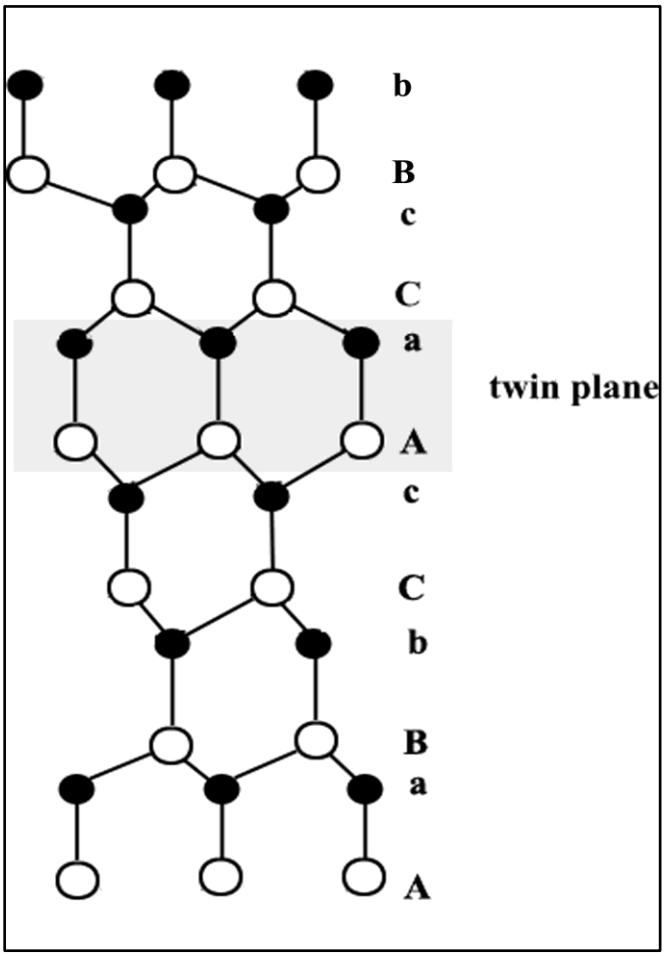

Figure 2.10. Stacking sequence in the ZB structure along the [111] direction.

The twin plane in the sequence is Aa bilayer.

CHAPTER 3

SEMICONDUCTOR NANOWIRES

Since the discovery of carbon nanotubes (Ijima & Ichihashi, 1993), there has been an exponential increase in interest and research on one-dimensional nanostructures – nanofibers, nanotubes, nanorods, and nanowires – mainly because the unique properties that they present related to their large surface area and possible quantum confinement in two dimensions. In particular, nanowires are defined as structures with diameters in the nanoscale range and length typically in the range of micrometers. Nanowires are usually symmetric in the two smaller dimensions and have a round or regular polyhedral cross-section (Dick K. , 2008). In addition to the unique properties that one-dimensional nanostructures own, nanowires are synthesized using a broad selection of semiconductor materials making this type of one-dimensional nanostructures ideal building blocks or interconnects for fabrication of nanoscale devices.

The bulk of this thesis focuses on the nucleation and growth of GaN nanowires. This chapter, however, is concerned with a more general discussion of semiconductor nanowires. The first section reviews the growth of semiconductor nanowires and starts with a brief introduction to the general synthesis strategies. Subsequently, this section presents a brief overview on crystal growth using thermodynamic and kinetic rationale. Finally, this section explores the growth mechanisms involve during nanowire synthesis. The second section surveys interesting fundamental properties as well as applications of semiconductor nanowires.

3.1. Growth of nanowires

In general, nanowire growth occurs due to an enhancement of the growth in one dimension and/or suppression of the growth in the other dimensions. Before discussing general strategies that promote this type of crystal growth, it is worth differentiating between growth methods and growth mechanisms. Herein, growth mechanism refers to the general phenomenon whereby a one-dimensional morphology is obtained, and growth method refers to the experimentally employed chemical processes that incorporate the underlying mechanism to realize the synthesis of these nanostructures (Law, Goldberger, & Yang, 2004).

Many methods have been developed for the synthesis of semiconductor nanowires. These methods follow either the top-down or bottom-up approaches. As mentioned before, the top-down approach takes advantage of existing lithographic technologies to form this type of nanostructures. However, size limitations seem to be a problem when trying to decrease the diameter of the nanowires. The growth methods that follow the bottom-up approach are more common since they have shown exceptional versatility in terms of material options and typically they produce nanowires with smaller diameters. Several growth methods that follow this approach usually use initial starting reactants in the vapor phase, but growth from solution has also been reported (Xia, et al., 2003).

Chemical vapor deposition methods such as MBE and MOCVD are the most explored synthetic methods for the growth of semiconductor nanowires. These methods usually use small particles of a foreign material to assist nanowire

growth. The particles are not consumed during growth, but act to substantially increase the growth rate in one dimension. This particular growth method is also called catalytic growth and depending on the phase of the particle (liquid or solid phase), the catalytic growth follow either the vapor-liquid-solid (VLS) or the vapor-solid-solid (VSS) mechanism. Another type of growth is the non-catalytic growth in which foreign particles are not used to assist the growth. This type of growth follows the vapor-solid (VS) mechanism. Also, template based methods represent a straightforward route to the synthesis of nanowires. In this approach, the template simply serves as support within (or around) which a different material is deposited and shaped into a nanowire with its morphology complementary to that of the template (Xia, et al., 2003). Template based methods, though, also have size limitations and limited flexibility of materials. (Cao, 2004).

The nanowires described in this thesis were grown using metalorganic sources in the vapor phase and Au particles were used to promote one-dimensional growth. The nanowires were grown *in-situ* in a transmission electron microscope and both VLS and VSS mechanisms were observed. These results will be presented in Chapter 5 and 6. The following sections review fundamental concepts related to the VLS as well as VSS mechanisms.

3.1.1. Crystal growth

Before describing the characteristic aspects of growth mechanism involved during nanowire growth, it is worth presenting a short review on the theory of crystal growth.

Crystal growth occurs when a driving force causes a system to depart from its equilibrium condition. In crystal growth of nanostructures, a system consists of two components. One is the medium (vapor, solution, or melt), which supplies the system with the growth species, and the other one is the solid surface of the growing crystal. The interface between the medium and the crystal is where growth or dissolution takes place (Sunagawa, 2005). Understanding the different aspects and properties of the medium-crystal interface is necessary for the understanding of crystal growth and control of the properties of nanostructures.

When the crystal grows from the vapor phase, which is generally the case for nanostructures, the thermodynamic driving force for crystallization is expressed by the ratio, *S*, between the equilibrium vapor pressure of the supply in the gas phase ($\boldsymbol{p_\infty}$) and the pressure $\boldsymbol{p}$ at growth (Sunagawa, 2005):

$$S = p/p_\infty$$

The term *S* is called supersaturation. Supersaturation can also be defined as the difference of the chemical potentials ($\boldsymbol{\Delta\mu}$), which are function of pressure, of the growth species in the vapor ($\boldsymbol{\mu_v}$) and the chemical potential of growing crystal ($\boldsymbol{\mu_c}$). In other words,

$$\Delta\mu = \mu_v - \mu_c = kT\, ln\frac{p}{p_\infty} = kT\ ln\, \mathrm{S}$$

Where $\boldsymbol{k}$ is the Boltzmann constant, $\boldsymbol{T}$ is the growth temperature, $\boldsymbol{p}$ is the pressure at growth, $\boldsymbol{p_\infty}$ is the vapor pressure of the supply, and $\boldsymbol{S}$ is the supersaturation. This means that the chemical potential of the growth species in the vapor has to

be higher than the chemical potential of the crystal in order for crystal growth to happen.

Crystal growth can be divided into two major types of growth. The first is growth of free-standing crystals, where nucleation and growth occur in a homogeneous medium (vapor, solution, or melt). The second type is the growth of a crystalline material on the surface of another crystalline material or substrate. When the structure and orientation of the growing crystal is influenced by the structure of the substrate, the type of growth is called epitaxy. There are two types of epitaxial growth: homoepitaxy in which the growing crystal and substrate have identical characteristics, and heteroepitaxy in which the growing crystal is of a different material from that of the substrate. Heteroepitaxy is the typical growth method when synthesizing semiconductor nanowires and other nanostructures.

The processes involved during epitaxial growth are shown in Figure 3.1. First growth species – atoms or molecules – arrive to the surface of the substrate (1). These are either adsorbed or desorbed onto and from the substrate (2). The adsorbed species are usually called adatoms or building blocks. The adsorbed species undergo surface diffusion on the substrate (3) and after some period of time these leave the substrate surface (4), or they become trapped by surface discontinuities (5) such as missing atoms or atomic steps, or they meet other diffusing species and form clusters (6). The irreversibly incorporation of the growth species into the substrate surface is thermodynamically favorable and results in the growth of the crystal. The creation of stable clusters leads to the formation of two-dimensional nuclei and allows the crystal to grow as well (Cao,

2004). Crystal growth is usually a combination of two fundamental processes: incorporation of growth species on the crystal surface and two-dimensional nucleation.

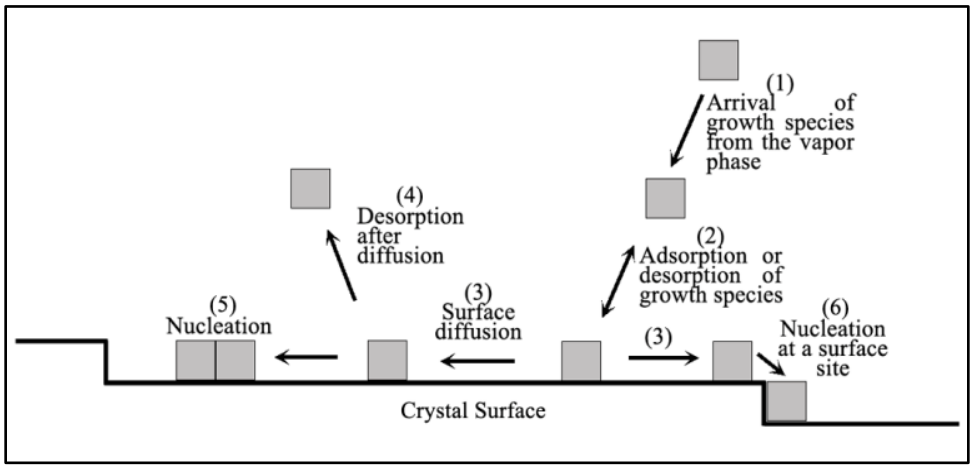

Figure 3.1 Atomistic representation of the processes involved during epitaxial growth. The growth species arrive to the medium-crystal interface (1). The growth species are either adsorbed or desorbed onto and from the surface (2). Adsorbed species undergo surface diffusion (3). During surface diffusion they could either leave the substrate (4), form clusters (5), or get trapped at surface discontinuities (6).

On the atomic scale, crystal surfaces are not smooth, flat, or continuous, and such discontinuities are responsible for crystal growth (Cao, 2004). Atoms in a crystal may be considered as cubes with a coordination number of six (six chemical bonds), thus, surface of a crystal may be represented as in Figure 3.2. The large flat regions between individual steps are called terraces (1) and they may contain defects such as vacancies (2). Terraces are connected by step edges, or ledges (3). Kinks occur wherever the ledge changes direction (ledge-kink) (4)

or when there is a vacancy (5) or adatom defect at the edge (kink) (6). Many bulk defects also terminate at the crystal including screw (7) and edge dislocations (8) and grain boundaries (Richardson, Holloway, & Unertl, 1996).

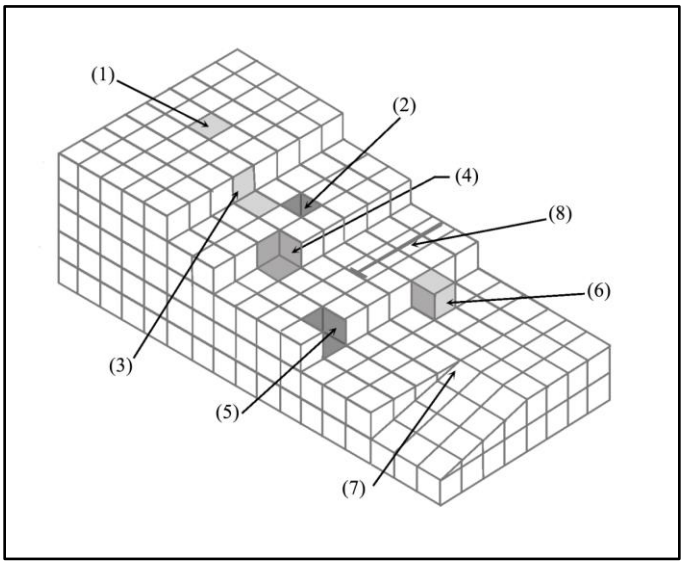

Figure 3.2. Atomistic representation of a crystal surface. Each atom is represented by cubes with six chemical bonds. The surface is composed of (1) terraces, which may contain vacancies (2). Terraces are connected by steps or ledges (3). Kinks occur wherever the ledge changes direction (ledge-kink) (4) or when there is a vacancy (5) or an adatom defect at the edge (kink) (6). Also screw (7) and edge (8) dislocations may terminate at the surface. This figure is a modify version of a figure in Richardson, Holloway, and Unertl (1996).

Crystal discontinuities act as incorporation sites for adatoms. Each incorporation site has a different number of unsatisfied bonds associated with it, thus, each incorporation site has a specific surface energy. Vacancies in the terrace and ledge have five and four unsatisfied bonds respectively. These are the most preferential incorporation sites with the highest surface energy, but these

sites are not considered to be of critical importance to crystal growth. This is because when adatoms fill the vacancies in the terrace or ledge, the number of unsatisfied bonds is reduced compare to the number of unsatisfied bonds on the vacancies, reducing also the surface energy of the site. Both ledge-kinks and kinks have three unsatisfied bonds and steps only have two unsatisfied bonds. Incorporation at these sites forms new sites having the same or more number of unsatisfied bonds than the original sites. Thus, these sites are important for crystal growth processes. Terraces are considered to be 'atomically flat' and have the lowest surface energy in a crystal. An adatom on a terrace is considered to be in a thermodynamically unstable state since only has one chemical bond with the surface. Incorporation on 'atomically flat' surfaces usually requires two-dimensional nucleation in order for the crystal to grow.

Two-dimensional nucleation is the process where two or more adatoms bind together to form a cluster of only one building layer high in the dimension perpendicular to the surface. There is an excess free energy associated with the formation of clusters of radius r (Figure 3.3). This excess free energy has two components: a negative part associated with the formation of a small volume of solid, which is proportional to r^3, and a positive part associated with the creation of a medium-crystal interface, which is proportional to r^2 (Porter & Easterling, 2004). The energy required for nucleation to occur increases as r increases, reaches a maximum at r_c and decreases thereafter (Sunagawa, 2005). If $r < r_c$ the system can lower its free energy by dissolution of the clusters, whereas when $r > r_c$ the free energy of the system decreases if the cluster grows. Stable clusters

with $r > r_c$ are referred as nuclei and r_c is known as the critical nucleus size (Porter & Easterling, 2004).

As mentioned earlier, a combination of incorporation of growth species into the crystal surface and two-dimensional nucleation is usually what takes place during crystal growth. However, processes that involve the incorporation of growth species into the crystal are preferential since growth species are more strongly bonded to crystal discontinuities such as steps and kinks than to an atomically flat surface. Different crystal growth modes are described depending on which of these processes is most prevalent during the crystal growth and these are described below.

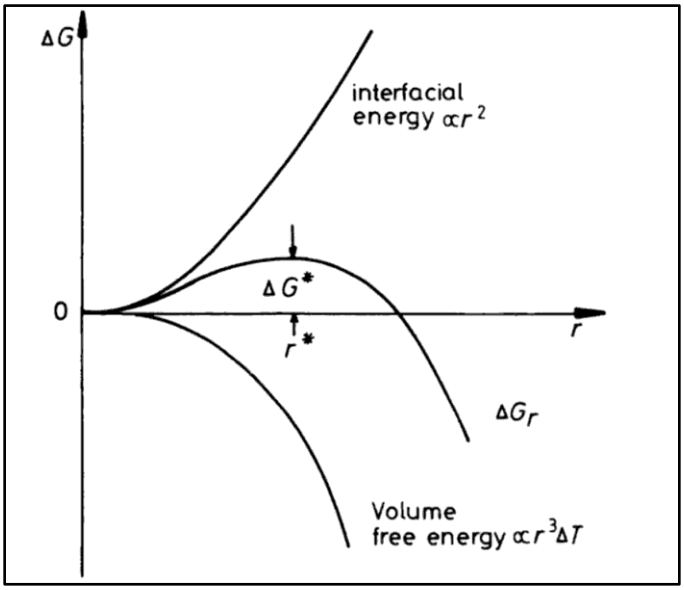

Figure 3.3. The free energy change associated with homogeneous nucleation of a cluster of radius r (Porter & Easterling, 2004)

A crystal growth mode that relies almost entirely on the incorporation at steps and kinks is called step flow growth (Sunagawa, 2005). Incorporation of

adatoms at kink or step sites forms new kinks and steps causing the steps to move forward across the surface (Figure 3.4 A). Steps continue to move forward until they reach the edge of the crystal and the surface becomes atomically flat. When all the steps run out, for step flow growth to continue a nucleation event must occur somewhere in order to form a new growth step.

Another crystal growth mode is called "birth and spread" (Sunagawa, 2005). This mode relies heavily on both incorporation at steps and kinks and on nucleation. In this growth mode the crystal growth begins with an atomically flat crystal face with no preferential incorporation sites. When a critical nucleus is formed on the atomically flat surface – birth – a rough surface with steps and/or kinks is generated, forming a new layer (Figure 3.4 B). This new layer then spreads by incorporation of adatoms at the step edges of the nucleus. This process is similar to the step flow growth except that it only consists of a single step. As this step is terminated at the edges of the crystal, a new 'atomically flat' layer is formed and the process is repeated. The growth conditions are such that the nucleation rate is low compared to the spreading rate. This means that the next birth does not occur until the lower layer has spread significantly.

A crystal growth mode that relies almost entirely on two-dimensional nucleation is also possible. A nucleation dominated growth usually requires a higher supersaturation than incorporation at stepped surfaces. This is because at high supersaturation values, the driving force for crystal growth is high, the critical nucleus is small, and the growth rates are high. In this regime, it is possible to come to a point where most of growth species that reach the crystal

surface nucleate with each other reaching the surface instead of incorporating at steps and kinks on the surfaces of the crystal. In this case nucleation becomes more important than incorporation at steps or kinks.

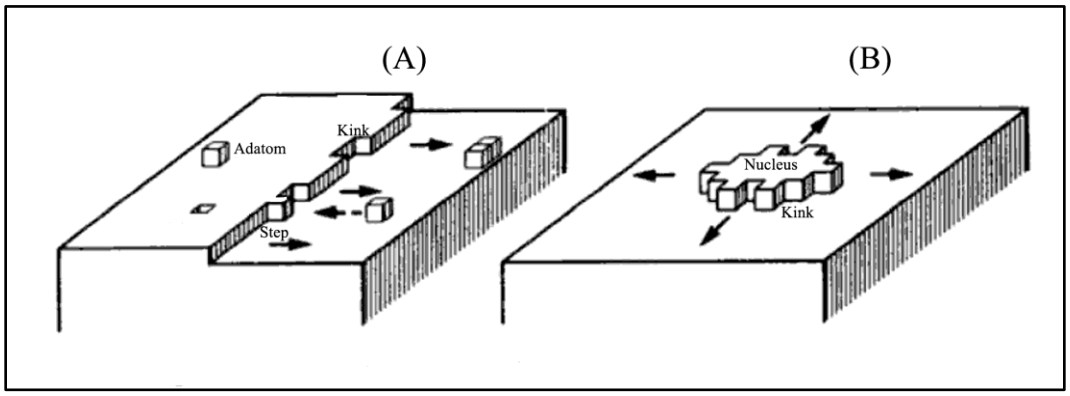

Figure 3.4. Schematic represetation of (A) step flow growth and (B) birth and spread growth (Sunagawa, 2005).

When all available steps are consumed and the supersaturation is not high enough for two-dimensional nucleation, screw dislocation serves as a continuous source to generate growth sites so that the stepped growth would continue. The crystal growth continues in a spiral growth, and this crystal growth mechanism is known as BCF theory since the concept was developed by Burton, Cabrera, and Frank (1951).

3.1.2 The VLS and VSS mechanisms

The vapor-liquid-solid mechanism has become one of the most prominent mechanisms for synthesizing semiconductor nanowires. This mechanism was first proposed by Wagner and Ellis (1964) to explain growth of whiskers – micrometer sized wires – as an alternative to the BCF mechanism (Burton, Cabrera, & Frank, 1951) in which a whisker was thought to contain an axial screw

dislocations that acted as a preferential growth site. In this original work, the authors concluded that metal particles promote the growth of whiskers from the vapor.

This study focused on the use of Au particles to grow Si whiskers, but the authors also reported similar results with Pt, Ag, Pd, Cu, and Ni particles. When a small Au particle was placed on a single crystal Si substrate (Figure 3.5A) and heated up to temperatures far above the Au-Si eutectic temperature, the authors observed the formation of a small droplet of Au-Si liquid alloy (Figure 3.5 B). After introducing the molecular precursor ($SiCl_4$), they noted the growth of solid material (Si) underneath the alloy droplet (Au-Si alloy) (Figure 3.5 C, D). They concluded that the surface of the alloy droplet is a preferential site for deposition from the vapor and proposed that it might act as a catalyst for the decomposition of the precursor. This results on the incorporation of Si atoms into the alloy droplet, which eventually becomes supersaturated with Si, promoting whisker growth by precipitation at the solid surface.

As a result of this study, Givargizov further elaborated experimental observations and developed models and theories regarding the VLS process for Si and Ge whiskers (Givargizov, 1975). More than fifteen years later, Hiruma and coworkers showed for the first time the validity of the VLS growth mechanism at the nanoscale (Yazawa, Koguchi, Muto, Ozawa, & Hiruma, 1992). The authors were able to grow InAs nanowhiskers or nanowires with diameters raging from 15 nm to 60 nm using a Au film of monolayer thickness. In this study, small Au particles were also observed on the nanowire tips and the authors concluded that a

similar mechanism proposed by Wagner and Ellis must take place during the growth of these nanowires.

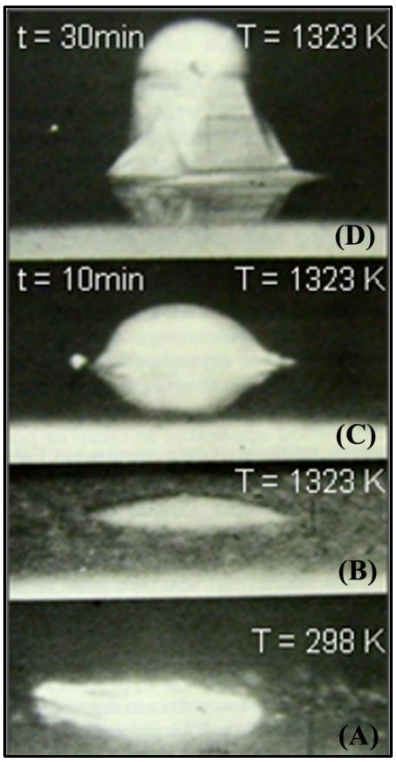

Figure 3.5. Sequence of frames taken during alloying and VLS growth. (A) gold particle on silicon substrate at room temperature; (B) liquid droplet of gold-silicon alloy at 1050 ˚C; (C) and (D) after 10 and 30 minutes respectively of growth at 1050 ˚C (Wagner & Ellis, 1964).

Since these initial results, there has been an explosion of work on the growth of semiconductor nanowires following the VLS mechanism, motivated in part by the potential advantages of semiconductors nanowires in nanoscale device applications. Nanowires have been grown from a variety of materials including single and compound semiconductors from the group IV, III-V and II-VI systems (Xia, et al., 2003) (Martensson, et al., 2004) (Law, Goldberger, & Yang,

Semiconductor Nanowires and Nanotubes, 2004), and using different metal particles and substrates. Also, there has been numerous reports on the growth of nanowire heterostructures following the VLS mechanism (Bjork, et al., 2002) (Gudiksen, J, J, C, & M, 2002) (Wu, Fan, & Yang, 2002).

In addition, advances in electron microscopy have allowed researchers to observe nanowire growth *in-situ* and study in great detail the kinetics involved in the VLS mechanism (Wu & Yang, 2001) (Kodambaka S. , Tersoff, Reuter, & Ross, 2007) (Hofmann, et al., 2008) (Kim, Tersoff, Kodambaka, Reuter, A, & Ross, 2008). Wu and Yang (2001) first reported the direct observation of the VLS mechanism at the nanoscale. In this work, micrometer-sized Ge particles were dispersed on a TEM grid together with solution-made monodispersed Au nanoclusters. After heating up the sample to 900 ˚C, Ge particles generate sufficient vapor to condense onto the neighboring Au clusters. Figure 3.6 shows a sequence of TEM images during the growth of a Ge nanowire. The authors identified three stages during the growth process that further confirmed the processes involve during the VLS mechanism. The first stage is an alloying process in which solid Au nanoclusters became liquid and increased in size after the incorporation of Ge atoms from the vapor at 900 ˚C (Figure 3.6 A and B). The second stage is nucleation (Figure 3.6 C) which was observed to occur at edge of the Au-Ge alloy droplet. Once the Ge nanocrystals nucleate at the liquid-solid interface, further condensation/dissolution of Ge vapor into the system increases the amount of Ge crystal precipitation from the alloy, leading to the third stage, axial growth (Figure 3.6 D).

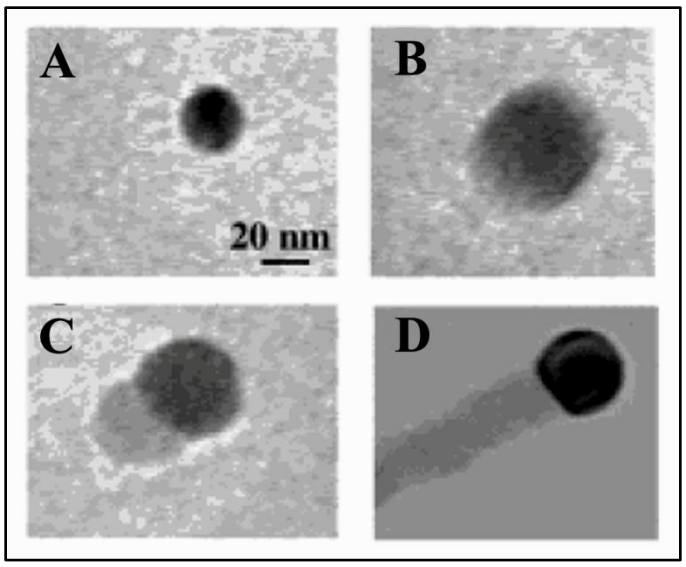

Figure 3.6. In-situ TEM images recorded during the growth of Ge nanowires. (A) Au nanocluster in solid state at 500 ˚C, (B) liquid Au-Ge alloy, (C) the nucleation of Ge nanocrystals on the alloy surface, (D) axial growth of Ge nanowires after further condensation from the vapor (Wu & Yang, 2001).

The VLS mechanism can be explained using simple thermodynamic concepts, however, kinetic processes, for example catalytic process or surface diffusion, should also be considered. In the case of Si nanowire growth promoted by Au particles (Figure 3.7 A), for example, the growth could be simply explained based on the Au-Si phase diagram (Figure 3.7 B). The Au-Si binary system is a simple eutectic system (Predel & Madelung, 1991-1998). There is a limited solubility in the solid phase which is less than 2 at. % Si in Au and less than 2 at. % Au in Si, but there is a continuous solubility in the liquid. In this binary system there is a single eutectic temperature (Te) at 363 ˚C, at which point the composition of the liquid alloy will be 18.6 at % Si. The VLS mechanism starts with a solid Au particle on top of a Si substrate at room temperature (1 in Figure

3.7). After heating the sample to a temperature above the eutectic temperature, a liquid Au-Si alloy is formed (2). This alloy droplet serves as preferential site for

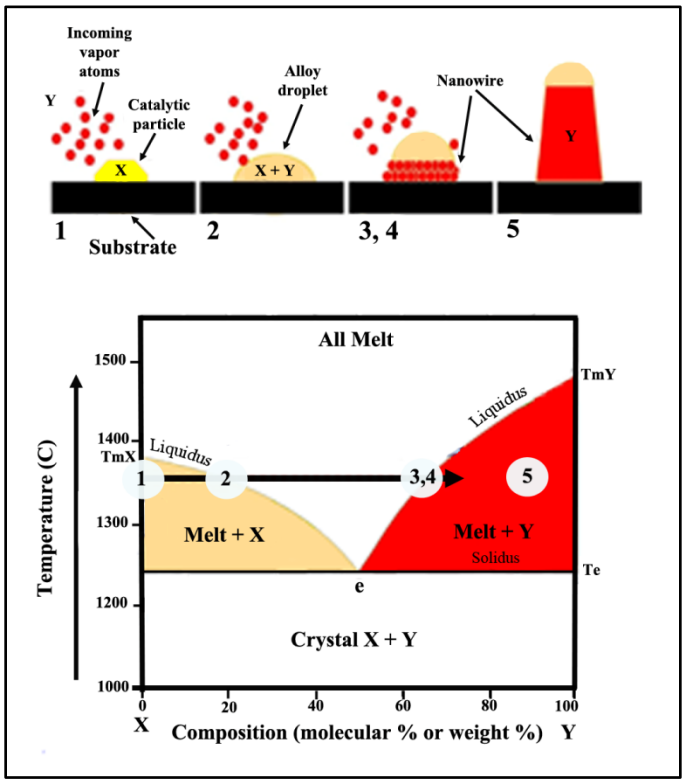

Figure 3.7. Schematic illustration of single semiconductor nanowire growth following the VLS mechanism and the main stages of this process are projected onto the conventional binary phase diagram of elements X and Y to show the compositional and phase evolution during the nanowire growth process.

the decomposition of the Si precursor – increasing the amount of Si in the vapor near the surface of the droplet. Si atoms dissolve into the alloy droplet until the composition reaches the liquidus line (3). Since the vapor is continuously supplied with an overpressure of Si precursor molecules, the Si concentration in the alloy droplet increases beyond the liquidus line and the droplet eventually becomes supersaturated. This is a thermodynamically unstable situation, thus the

alloy droplet precipitates Si (4) at the liquid-solid interface in order to re-establish the stable composition. Further growth occurs by the continuous incorporation of Si atoms onto the liquid-solid interface (5).

An extension of the VLS growth mechanism is the VSS mechanism. In the VSS mechanism, as mentioned before, a solid metal particle is used to promote the unidirectional growth. Convincing evidence of the state of the particle during nanowire growth was presented by Kodambaka et al. (Kodambaka S. , Tersoff, Reuter, & Ross, 2007). In this work, Ge nanowires were grown from the vapor using Au particles inside an electron microscope. In-situ observations indicated that both VLS and VSS growth mechanism can occur simultaneously below the bulk eutectic temperature. The authors concluded that sufficient supersaturation must be maintained for the alloy droplet to continue in the liquid phase below the eutectic temperature, otherwise, the particle solidifies and the VSS growth mechanism takes place. This study proves that the VLS and VSS mechanisms are very similar. However, growth kinetics may differ in both cases.

Very recently, a review on the thermodynamics and kinetics of the VLS and VSS mechanisms was presented by Wacaser and coworkers from Lund University (Wacaser, Dick, Johansson, Borgstrom, Deppert, & Samuelson, 2008). In this review, the authors presented a more general mechanism to explain nanowire growth. They suggested that the boundary where the vapor, catalytic particle, and nanowire meet is a preferential site for incorporation of the growth species and nucleation of the crystal. They showed that the reason for this was that the Gibbs free energy is most flexible at this boundary and can thus be

minimized. Additionally, this boundary has a relatively high supersaturation because of the contact with the supply. This general mechanism, called by the authors *preferential interface nucleation*, emphasizes both the fundamental importance of nucleation differences and the different interfaces and phase boundaries in a three phase system. The next section presents the highlights of this review.

3.1.3 Thermodynamics and kinetics behind nanowire growth

In a three phase system at least three materials or phases of the material participate in the growth process. This system consists of a supply that is usually in the vapor phase, a catalytic particle that is either liquid or solid and collects the growth species, and the nanowire (Figure 3.8). The boundary where these three phases meet is called the triple phase boundary (TPB) (Wacaser et al., 2008).

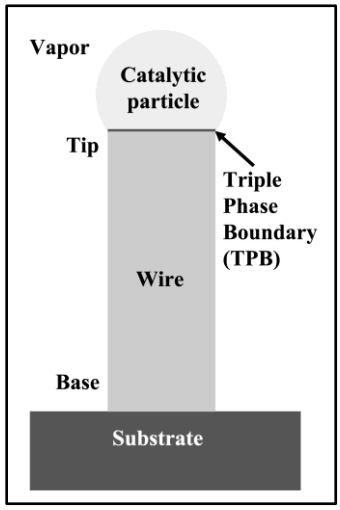

Figure 3.8. Schematic representation of the different phases involved during nanowire growth. (Modified from Wacaser, 2008)

Previously, it was mentioned that supersaturation is the driving force for crystal growth. In the case of nanowire growth, the three phase system has three

important interfaces, the medium-particle, particle-nanowire, and medium-nanowire. The magnitudes of the relative supersaturation at these interfaces are (Wacaser et al., 2008):

$$\Delta\mu_{vp} = \mu_v - \mu_p$$

$$\Delta\mu_{pn} = \mu_p - \mu_n$$

$$\Delta\mu_{vn} = \mu_v - \mu_{\mathrm{n}}$$

where $\Delta\mu_{vp}$, $\Delta\mu_{pn}$, and $\Delta\mu_{vn}$ are the difference in chemical potentials between the vapor and particle, particle and nanowire, and vapor and nanowire respectively; and μ_{v}, μ_{p}, and μ_{n} are the chemical potential of the vapor, particle in the liquid or solid phase, and nanowire respectively.

The medium supplies the growth species, thus the chemical potential of the vapor should be the highest. The nanowire act as a sink for the growth species, thus its chemical potential would be the lowest. During nanowire growth, then, the next inequality must be true:

$$\mu_v \geq \mu_p \geq \mu_c$$

The chemical potential within a particular phase will be uniform unless there are inhomogeneities in the system such as chemical reactions, gradients in temperature and/or concentration, or different surface structures at different interfaces. Considering uniform chemical potentials for each phase, the previous inequality indicates that the difference in chemical potential between the growth species in the vapor and the nanowire is higher than the difference in chemical potential between the catalytic particle and the nanowire. This means that the driving force for crystallization at the catalytic particle-nanowire interface is

smaller than or similar to the driving force for crystallization on the vapor-nanowire interface. In other words, the growth at the particle-nanowire interface is slower than the growth at the medium-nanowire interface. This statement is not valid for nanowire growth. Thus, in order to describe the enhancement of the growth rate under the catalytic particle, inhomogeneities of the system should be taken into account (Wacaser et al., 2008).

The local supersaturation near the particle-nanowire interface can be higher than that near the medium-nanowire interface if a kinetic process locally increases the chemical potential of the growth species inside the particle. An example of a kinetic process is a catalytic chemical reaction combined with transport to the particle-nanowire interface. Nanowire growth systems frequently use molecular precursors to supply the growth species to the system. These precursors must decompose before the growth species get incorporated into the seed particle. If the seed particle acts as a catalyst for the decomposition of the precursor, then the decomposition happens more rapidly on the medium-particle interface than on the medium-nanowire interface. Thus, the concentration and local chemical potential of the growth species would be higher at the medium-particle than at the medium-nanowire interface. This means that the chemical potential of the growth species in the particle has a maximum for the system, creating the driving force for nanowire growth.

The enhanced growth rate at the particle-nanowire means that the activation energy for nanowire growth is less than that for bulk growth. This difference in activation energies between a catalyzed and non-catalyzed

decomposition can be used to demonstrate the occurrence of catalytic activity during nanowire growth. In practice, however, it is difficult to determine the appropriate activation energies, since most kinetic process may depend on the materials present such as carrier gas, other precursors, substrate, even reactor walls, and in some cases may depend on growth conditions (Dick, 2008). Some research groups have reported difference in activation energies between nanowire growth and bulk growth, concluding that catalysis is the rate limiting process during growth.

Catalytic chemical reactions are not always the rate limiting process. For example, growth of nanowires is possible by MBE in which no precursors are used and thus catalytic dissociation does not exist (Schubert, et al., 2004). Also, GaAs nanowires and GaAs layers grown with the same conditions were reported to have the same activation energy of growth (Borgstrom, Deppert, Samuelson, & Seifert, 2004). These observations might be explained by considering gradients in temperature and/or concentration, which might also cause a maximum local chemical potential at the particle-nanowire interface.

Wacaser and coworkers evaluated the nucleation at the vapor-particle, particle-nanowire, vapor-nanowire, and vapor-particle-nanowire interfaces. The rate of formation of a nucleus, $\boldsymbol{J}$, of arbitrary size depends on the concentration of growth species, $\boldsymbol{C}$, and the change in Gibbs free energy at the interfaces, $\boldsymbol{\Delta G}$, that is,

$$J \propto C \exp\left(-\frac{\Delta G}{kT}\right)$$

where k and T are the Boltzmann constant and growth temperature respectively.

The magnitude of the concentration of the growth species in a solid or liquid solution can be written in terms of the supersaturation or the difference in chemical potential $\Delta\mu$ of the two phases, and the equilibrium concentration C_{eq}, which is the value for which the chemical potential is the same in the two different phases,

$$C = C_{eq} \exp\left(\frac{\Delta\mu}{kT}\right)$$

The particle may be a solution or alloy that can possibly be described by the previous equation, but the medium is often a vapor or molecular beam. To compare the concentration and equilibrium concentration of the particle to the equivalent values in a vapor one must compare partial pressures to solution concentrations. In other words

$$P = P_{eq} \exp\left(\frac{\Delta\mu}{kT}\right),$$

where P is the partial pressure of the growth species in the vapor and P_{eq} is the equilibrium vapor pressure. The differences in concentrations may have an effect on the nucleation rates and thus the growth rates at the different interfaces and are important to the general nanowire growth.

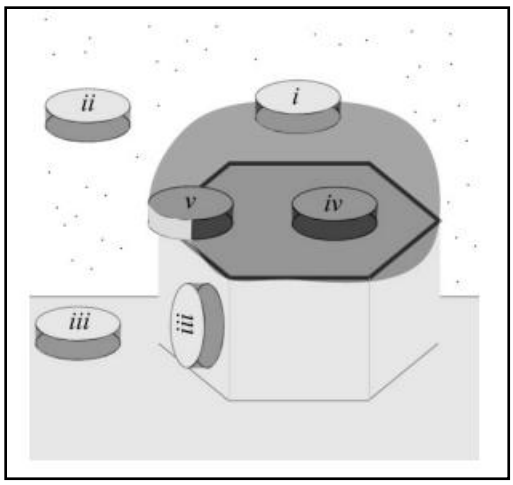

Figure 3.9. Illustration depicting nucleation at different interfaces in a three-phase system. (i) Nucleation on a heterogeneous particle surface (a the medium-particle interface). (ii) Homogeneous or self nucleation. Nucleation on a homogeneous crystal at (iii) the medium-nanowire interface, (iv) the particle-nanowire interface, and (v) the triple phase boundary (Wacaser et al, 2008).

When a nucleus forms at the medium-particle interface (nucleus i in Figure 3.9), the change in Gibbs free energy for the formation of a crystalline nucleus from the medium onto the particle surface (ΔG_{vp}) can be written as:

$$\Delta G_{vp} = -n\,\Delta\mu_{vc} + Ph\gamma_{vc} + A(\gamma_{pc} + \gamma_{vc} - \gamma_{vp})$$

The first term is the energy released when the chemical potential of a number *n* of atoms or building blocks changes for the vapor to the particle phase. The other two terms represent interfaces that are formed or are changed when a nucleus develops. The second term in the previous equation represents the edge of a nucleus with a height *h* and a perimeter length *P*. This edge is a medium-nanowire interface and has the specific surface energy of the medium-nanowire interface γ_{vc}. The third term represents the other three interfaces involve which

all have the same area *A*. Using the same rational, the change in Gibbs free energy for the formation of every nucleus in Figure 3.9 can be found and these are listed in Table 3.1.

Table 3.1. Change in Gibbs free energy for a nucleus form at different interfaces in a three phase system (Wacaser et al., 2008).

Nucleus	ΔG
i	$\Delta G_{vp} = -n\,\Delta\mu_{vc} + Ph\gamma_{vc} + A(\gamma_{pc} + \gamma_{vc} - \gamma_{vp})$
ii	$\Delta G_{vcv} = -n\,\Delta\mu_{vc} + Ph\gamma_{vc} + 2A\gamma_{vc}$
iii	$\Delta G_{vc} = -n\,\Delta\mu_{vc} + Ph\gamma_{vc}$
iv	$\Delta G_{pc} = -n\,\Delta\mu_{pc} + Ph\gamma_{pc}$
v	$\Delta G_{TPB} = -n\,\Delta\mu_{vc} + P_{pc}h\gamma_{pc} + P_{vc}h\gamma_{vc}$

It is worth noticing that the energy term in ΔG for nucleation at the triple phase boundary has two terms. One part of a nucleus will be a vapor-crystal interface and the other a particle-crystal interface with perimeter length P_{vc} and P_{pc} respectively. Additionally, all three of the supersaturations could be considered at the triple phase boundary, but only the largest supersaturation ($\Delta\mu_{vc}$) is considered to be the most important at this boundary.

Comparing the expressions for the different Gibbs free energies of nucleation in Table 3.1, might lead to an understanding of which interfaces are more preferential nucleation sites. At the triple phase boundary, the supersaturation is at its highest because it is in contact with the medium (vapor). The edge energy terms are variable depending on the shape and placement of the

nucleus. Thus, the change in Gibbs free energy for the formation of a nucleus at this boundary could be very low because the supersaturation is high and the edge energy terms can be adjusted to minimize ΔG. This makes the triple phase boundary the most preferential nucleation site in a three phase system.

After nucleation occurs, either at the particle-nanowire interface or on the triple phase boundary, steps will exist at the edges of the nuclei. The steps can propagate by step flow along the interface. Thus it is possible to think of nanowire growth as a birth at the triple phase boundary and spread of that nucleus to form the nanowire. The type of morphology of the nanowires that are formed will be greatly dependent on the nucleation rates and step propagation rates of the system (Wacaser, Dick, Johansson, Borgstrom, Deppert, & Samuelson, 2008). Further discussion on the growth of nanowires is presented in Chapter 6 and 7.

3.2 Some properties and application of semiconductor nanowires

Semiconductor nanowires are of particular interest for device applications, as they exhibit quantum confinement in two dimensions while the third is relatively unrestricted. As described before, the density of states is not a continuous function of energy, and causes sharp and strong electronic transitions that might improve, for example, the optoelectronic properties over the bulk materials (Li, Qian, Xiang, & Lieber, 2006). Nanowires also can be used as interconnects in nanoscale devices (Lu & Lieber, 2007). The additional free surface, compare to thin films, brings strain relief to the crystal, decreasing the density of dislocations and improving the crystallinity of the material. In addition, nanowires have higher surface-to-volume ratio than other similar

structures, making them interesting for catalysis and sensing applications (Xia, et al., 2003).

Quantum confinement effects play a significant role in determining the energy levels, and hence the optical properties, of nanowires. This implies that nanowire band gaps, and thus wavelength, can be tuned by changing their size. The electrical transport properties of nanowires are particularly important since controllable and predictable conductance is vital to many nanoscale electronics applications (Lieber, 1998). Semiconductor nanowires have been used as conducting channels in field-effect transistors (FETs) (Chung, Yu, & Heath, 2000) (Duan, Huang, Cui, Wang, & Lieber, 2001) (Goldberger, Sirbuly, Law, & Yang, 2005). However, further research needs to be done in order to find out if a nanowire transistor can operate better than other transistor types. Semiconductor nanowires can act as both light emission sources, such as LED's and lasers, and a light detention elements, such as UV detectors or photovoltaics (Sirbuly, Law, Yan, & Yang, 2005), improving the efficiency of optoelectronic devices.

CHAPTER 4

INSTRUMENTATION AND METHODS

As mentioned previously, this thesis reports direct observations of the nucleation and growth of GaN nanowires. The entire growth process was observed *in situ* and controlled in real time using an environmental transmission electron microscope (ETEM). Au particles were used to promote the nanowire growth. The particles were deposited onto perforated SiOx film TEM grids by sputtering at room temperature. Trimethylgallium (TMG) and ammonia (NH_3) were the Ga and N sources respectively. Post-growth structural and chemical analysis was performed using several techniques in a transmission electron microscope (TEM).

This chapter starts with a section dedicated to *in situ* electron microscopy with emphasis on environmental TEM and a description of the microscope that was employed in this study. Subsequently, characterization techniques such as electron energy loss spectroscopy (EELS), energy dispersive X-ray spectroscopy (EDX or EDS), and high resolution electron microscopy (HREM) are briefly reviewed. The final part of this chapter covers basic aspects of sputtering deposition.

4.1 *In situ* transmission electron microscopy

Transmission electron microscopy is a powerful technique for characterization of nanostructures. Due to continued efforts in electron optics, the lateral resolution of electron microscopes has now dropped below 0.1 nm (Haider, Rose, Uhlemann, Kabius, & Urban, 1998). Additionally, the ability of forming

strongly focused electron probes (Krivanek, Dellby, & Lupini, 1999) offers electron microscopes with the capability to provide analytical techniques with high lateral resolution. The combination of high-resolution imaging and analytical analysis offers valuable structural and chemical information to nanostructure growers, allowing them to optimize the crystallinity, morphology, and chemistry of nanostructures. However, post-growth characterization lacks in providing direct information on the way in which variables such as temperature, stress, and environment affect the structure, and hence, the properties of nanostructures. Such important information can be obtained by performing *in situ* experiments in the electron microscope.

In situ electron microscopy is a unique and effective technique to study the response of materials to a change in state. *In situ* experiments involve the use of special stages and/or modification of conventional TEMs to introduce and control these changes while observing the microstructure of the material. As a result, *in situ* studies in these modified electron microscopes have allowed researchers to observe chemical and physical processes at the atomic scale and measure the kinetics of these processes directly.

It has been demonstrated for decades that experiments can be conducted in real time inside the specimen chamber of electron microscopes. Late 1950's specific *in situ* experiments were first developed by Hirsch et al. (Hirsch, Horne, & Whelan, 1956). In this work, plastic deformation experiments using aluminum thin foils were carried out inside a TEM. Arrangement and motion of dislocations were observed by applying stress to the sample with a large beam current and

finely focused illumination in a 100kV TEM. Later in the 1960's and 1970's, a series of experiments were conducted in which a combination of a hot stage and ultra high vacuum was introduced to study the nucleation and growth process involve during thin film formation (Pashley, 1965) (Yagi, Takayanagi, Kobayashi, & Honjo, 1976). In 1981, Sinclair et al. demonstrated the value of using *in situ* electron microscopy to study the surface of CdTe thin films at atomic resolution (Sinclair, Yamashita, & Ponce, 1981). Other important applications of *in situ* electron microscopy are summarized by Butler and Hale (1981). Although these early *in situ* experiments in ultra high vacuum have produced important results for materials science, there are important applications in materials science such as crystal growth and catalysis in which the effect of environment on the sample is extremely important.

The beginnings of environmental transmission electron microscopy started in the 1930's with applications in biology (Marton, 1935) (Abrams & McBain, 1944). The aim of these studies was to keep the biological specimen hydrated by introducing water vapor or other solvent medium. In the early 1970's, Baker et al. (Baker, Thomas, & Wells, 1975) studied the reshaping of catalyst particles under various gas environments, but direct observations were lacking on atomic resolution. Later, Boyes and Gai (Boyes & Gai, 1997) designed and developed an environmental cell for a conventional TEM that offered *in situ* studies of materials at atomic scale. In basic terms, the environmental cell combines small apertures (located at various levels) and different pumping levels in order to restrict gas flow above and below the sample area as well as to provide maximum channeling

of the electron beam through the sample. The environmental TEM (ETEM) has been successfully used to understand physical and chemical processes in different research areas such as catalysis, metallurgy, and semiconductor processing (Gai P. L., 1997) (Gai P. L., 1999) (Sharma R. , 2005).

In particular, the possibility of introduction of different gases into the sample area coupled with thermal heating of the sample makes the TEM not only a characterization tool but also a chemical vapor deposition mini-chamber, allowing researchers to study directly the dynamic processes involved during growth of nanostructures and the relation of these processes with the structural and chemical characteristic of such materials. (Kodambaka S. , Tersoff, Reuter, & Ross, 2007) (Kodambaka, Tersoff, Reuter, & Ross, 2006) (Hofmann, et al., 2008) (Kim, Tersoff, Kodambaka, Reuter, A, & Ross, 2008) (Diaz, Sharma, Jarvis, Zaidi, Zhang, & Mahajan, Submitted).

In our research, *in situ* observations were carried out in environmental scanning transmission electron microscope (ESTEM) FEI TECNAI F-20 (Figure 4.1) at Arizona State University. TECNAI F-20 is a 200 keV field emission gun high resolution and analytical TEM/STEM with a 1.2 nm spherical aberration coefficient and 0.24 nm Scherzer resolution. This unique microscope is equipped with a differential pumping system that consists of two sets of apertures (arranged a'- a and b'- b as shown in Figure 4.2) and three pumping levels. The region between these two sets of apertures is pumped out by a turbo-molecular pump, creating the first level of pumping. A second level of pumping is introduced above and below the b'- b apertures to pump out any gas that is leaking through

them. Usually, a third level of pumping is introduced between the condenser aperture and the electron gun, thus improving the vacuum around the electron gun (Sharma R. , 2005). This particular design allows the possibility to get routinely atomic resolution images and EELS spectra from nanoparticles under H_2 gas pressures in the range of about 0.5 to 1.5 Torr.

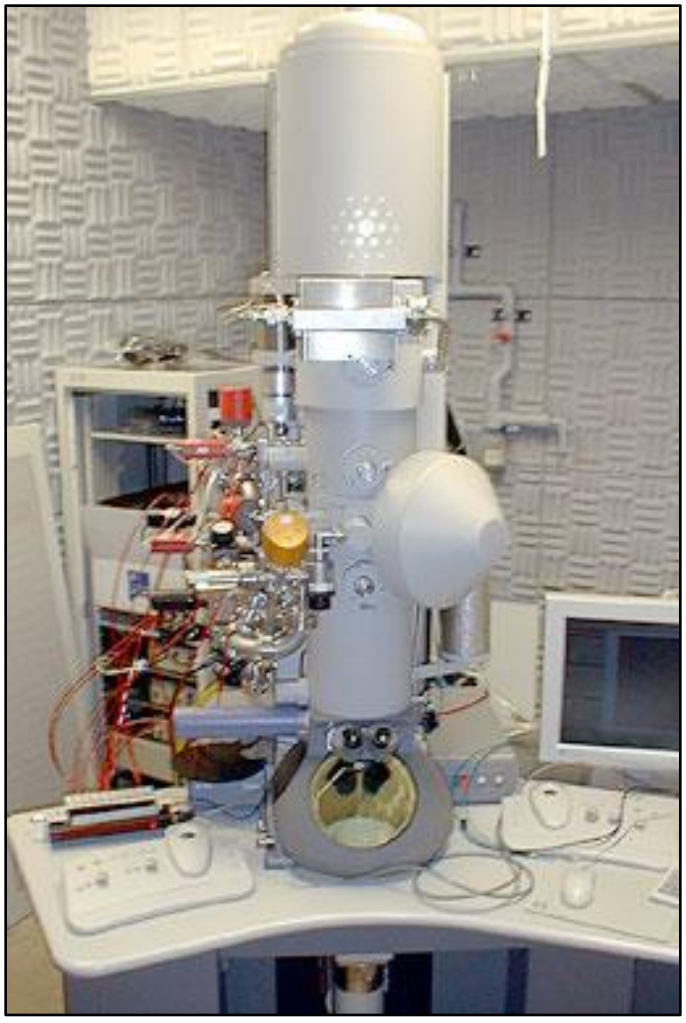

Figure 4.1. FEI TECNAI F-20 is equipped with a differential pumping system for in situ studies of gas-solid/liquid and liquid/solid interactions.

The system can handle gas pressures up to 10 Torr, has both heating (900 $^{\circ}$C) and cooling (liquid N_2) holders for controlled-temperature studies and is

equipped with annular dark-field detectors for STEM imaging and post-column Gatan Imaging Filter (GIF) for energy-filtered diffraction, imaging and EELS analysis. Low and high magnification images and digital videos with 15 frames per second time resolution are recorded using a Gatan Orius 600SC camera.

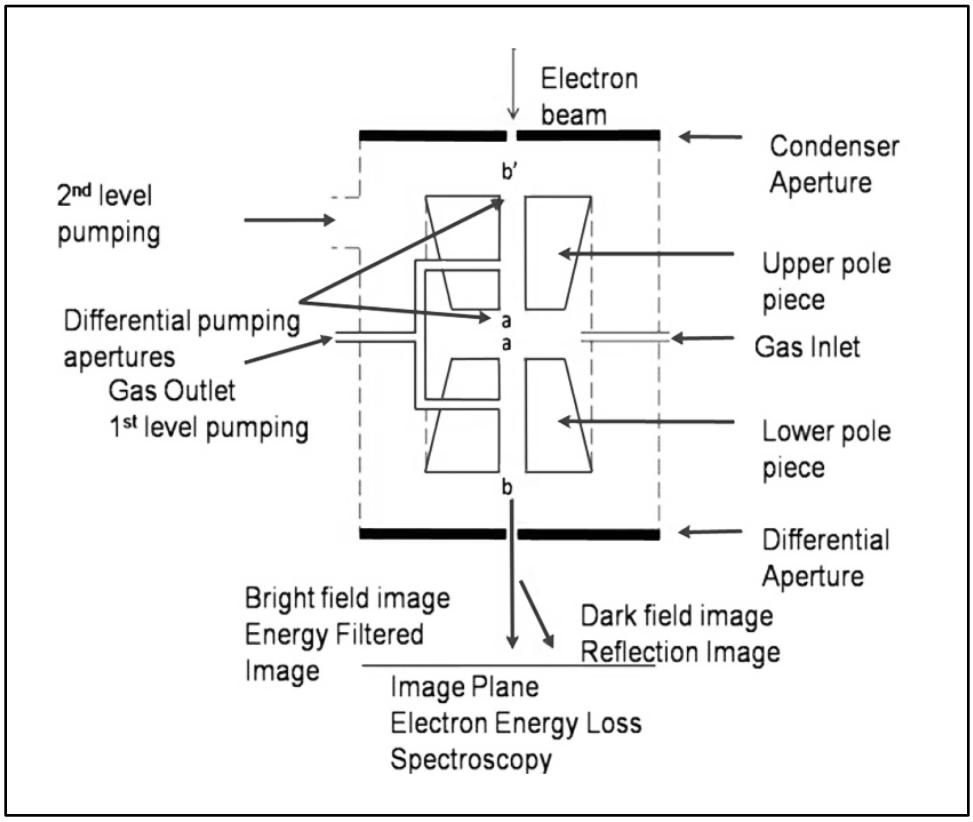

Figure 4.2. Schematic representation of the differential pumping system found in Tecnai F-20 ETEM (Sharma, R., 2005)

4.2 Characterization Techniques

4.2.1 Basic concepts in electron microscopy

4.2.1.1 Interaction between electrons and materials

When a specimen is illuminated with high energy electrons, various interactions between the specimen and the incident electrons can occur (Figure

4.3). When the specimen is extremely thin, many electrons penetrate the specimen without interactions, and these electrons are called transmitted electrons. The rest of the electrons interact with the specimen and the probability of interaction increases with specimen thickness.

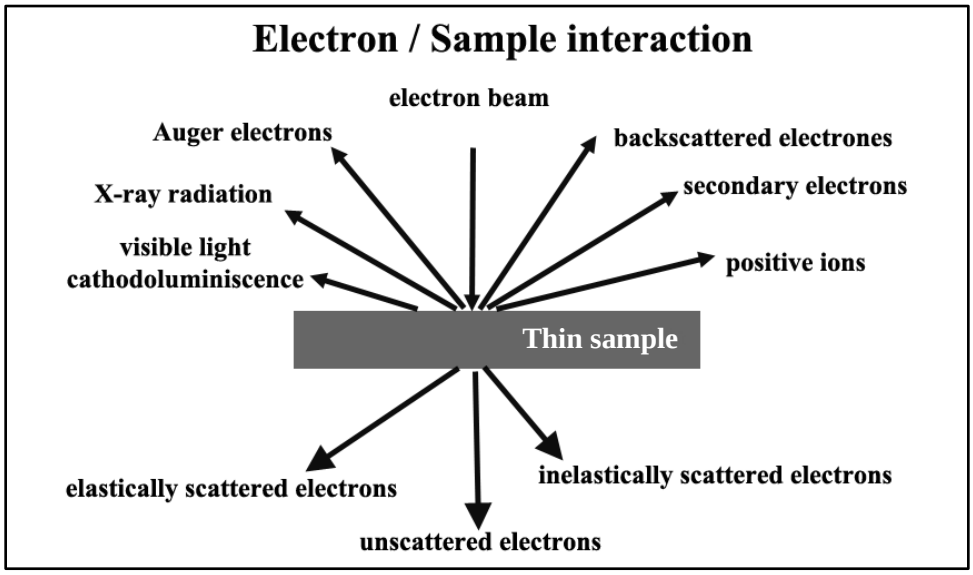

Figure 4.3. Schematic diagram of the signals created during transmission of a high-energy electron beam through a thin solid sample (Brydson and Hammond, 2005)

Electron scattering caused by the specimen can be classified into two groups: elastic scattering and inelastic scattering. Elastic scattering is generally coherent, that is, the phase relationship between scattered waves from different atoms is preserved, and involves no change in the energy of the primary electron, although there may be large changes in direction (Brydson & Hammond, 2005). Diffracted electrons and back-scattered electrons belong to the elastic scattering category. Imaging modes such bright-field methods, dark-field method, and high-resolution electron microscopy mainly utilize elastically scattered electrons.

Although elastic scattering strictly refers to scattering involving no exchange of energy, this is only true for small scattering angles. For scattering angle of 180˚, a head-on collision, the energy transfer may exceed 1eV for a 100-keV incident electron and may be sufficient to displace the atom from its position in a crystalline lattice (Brydson & Hammond, 2005).

Inelastic scattering is incoherent, that is, any phase relationship between scattered waves are lost, and involves a loss in the energy of the incident electrons. There are many interaction processes that can cause energy to be lost by the incident electrons and transferred to the electrons or atoms of the specimen. Inelastic scattering processes are responsible for the stopping of an electron by a bulk solid with almost all of the kinetic energy carried by the primary incident electrons ending up as a heat (phonons) in the specimen (Brydson & Hammond, 2005). A small proportion of the energy may escape as either X-rays or secondary electrons. It is the energy analysis of the inelastic scattered electrons that forms the basis for electron energy loss spectroscopy (EELS). The spectroscopy of characteristic X-rays resulting from inner-shell excitation is called energy dispersive X-ray spectroscopy (EDX) (Shindo & Oikawa, 2002).

4.2.1.2 Basics of the analytical electron microscope

A detailed description of the components and operation of the transmission electron microscope is given by Williams and Carter (1996). In this section, the basic experimental design will be summarized. Firstly, the electron gun is located at the top of the column and consists of a filament (W or LaB_6) and a focusing electrode (Wehnelt). Electrons are emitted from the electron gun by

thermionic emission (W or LaB_6) or by field emission (single crystal W) or, in recent machines, a combination of the two. The type of electron gun determines the total emission current from the gun, the source size, and the spread of electron energies contained in the electron beam (Brydson R. , 2002).

The electron beam is accelerated towards the anode and then passes through electromagnetic lenses. The final beam energy ranges typically between 100 and 400 keV in most standard commercial instruments. Two or more electromagnetic condenser lenses demagnify the probe to a size typically between a few microns and few nanometers; the excitation of these lenses controls both the beam diameter and the beam divergence/convergence. The electron beam then passes through the sample, which is usually a thin (<100nm) 3 mm disc of the material or a material supported on an electron transparent grid. The specimen is inserted into the vacuum of the TEM column via an airlock and fixed into a side-entry specimen rod, which can be translated or tilted (about one or two axes) (Brydson R. , 2002).

After passing through the specimen, the electron beam forms an image by appropriate action of the objective lens. The main electromagnetic objective lens forms the first intermediate real-space projection image of the illuminated specimen area (in the image plane of the lens) as well as the corresponding reciprocal space diffraction pattern (in the back focal plane of the lens). The objective aperture can be inserted in the back focal plane of the objective lens to limit beam divergence to the magnified image. The large image is then formed via a projector lens system. This system consists of a first projector or

intermediate lens which focuses on either the objective lens image plan (image mode) or the back focal plane (diffraction mode). The first projector lens is followed by a series of three or four projector lenses – each of which magnifies the image by a factor of 20 x. The final image is formed on the fluorescent screen and recorded on a photo-film or by a digital camera. The EESL spectrometer is located below the camera and usually possesses a variable entrance aperture (Brydson R. , 2002).

A TEM image consists of a combination of mass-thickness contrast, diffraction contrast, and at higher magnifications phase contrast. Image resolution is primarily determined by imperfections or aberrations in the objective lens; two common aberrations are known as spherical aberration – whereby electrons from one object point travelling through the lens at differing distances from the optic axis, are focused to different points in the image – and chromatic aberration – whereby electron from one object point, which have differing energies, are focused to different points in the image.

A scanning TEM (STEM) serially scans a small (typically nanometer) probe, produced by an electron gun/lens system, in a two-dimensional raster across the specimen. Dedicated STEMs employ extremely small probe sizes produced by cold field emission electron sources and can provide extremely high-spatial and high-energy resolution EELS measurements, while there are a number of hybrid TEM/STEM instruments which can operate in both modes, which is the case of the TEMs used in this work.

4.3 Sputtering

Sputtering is a vacuum evaporation process which physically removes portions of a coating material called the target, and deposits a thin, firmly bonded film onto an adjacent surface called the substrate. The process occurs by bombarding the surface of the sputtering target with gaseous ions under high voltage acceleration. As these ions collide with the target, atoms or occasionally entire molecules of the target material are ejected and propelled against the substrate, where they form a very tight bond. The resulting coating is held firmly to the surface by mechanical forces, although, in some cases, and alloy or chemical bond may result.

Sputtering has proven to be successful method of coating a variety of substrates within thin films of electrically conductive or non-conductive materials. One of the most striking characteristics of sputtering is its universality. Since the coating material is passes into the vapor phase by a mechanical rather than a chemical thermal process, virtually any material can be deposited. Direct current is used to sputter conductive materials, while radio frequency is used for non-conductive materials. The range of sputtering application is large. Current applications of great importance include thin films of magnetic materials for data storage, optical materials for lens characteristics, thin film resistors, amorphous bubble memory devices, among others.

CHAPTER 5

DIRECT OBSERVATION OF NUCLEATION AND EARLY STAGES OF GROWTH OF GAN NANOWIRES

5.1 Introduction

Due to their special characteristics, the group III nitride semiconductors nanowires have attracted considerable interest for applications in a number of optoelectronics devices and high power/temperature electronic applications. The synthesis of GaN nanowires has been reported using different growth methods such as laser ablation (Duan & Lieber, 2000), chemical vapor deposition (Chen, et al., 2000) (Tang, Fan, Dang, Li, & Liu, 2000), and metalorganic chemical vapor deposition (Kuykendal, Pauzauskie, Lee, Zhang, Goldberger, & Yang, 2003). Most of these methods use a metal particle to grow the nanowires, following the vapor-liquid-solid mechanism first proposed by Wagner in 1964 (Wagner & Ellis, 1964). Although this mechanism is widely accepted, there is a lack of understanding of the processes involved during nucleation and early stages of growth of GaN nanowires. Some questions, still to be resolved, concern the phase of the metal particle, the nature of nucleation sites, and the evolution of the particle-nanowire interface.

In this chapter, direct observations and early stages of growth of GaN nanowires are reported. The nanowires were formed by exposing Au + Ga alloy droplets to ammonia (NH_3). The formation process was observed *in situ,* and controlled in real time using an environmental transmission electron microscope. *In situ* observations on self-catalytic growth of GaN nanowires have been

reported by Stach et al. (Stach, Pauzauskie, Kuykendall, Goldberger, He, & Yang, 2003). GaN nanowires were formed by decomposing a GaN film at high temperature inside a transmission electron microscope (TEM) column. The decomposition of the GaN film produced Ga droplets and Ga/N vapor species. Then, Ga droplets dissolved N from the vapors, resulting in GaN nanowires. Although this is an interesting observation and a novel technique to synthesize GaN nanowires, they were not able to observe the nucleation events or early stages of growth of the nanowires.

Recently, Hoffman et al. (2008) and Kim et al. (2008) have shown that *in situ* observations of nucleation events using a TEM can provide unambiguous insight into the nucleation of nanowires, in these cases Si. In both studies the growth process followed several steps: 1) disilane (Si_2H_6) introduction into the TEM column, 2) Si_2H_6 adsorption and dissociation at metal particle interface, and 3) Si supersaturation of the metal particle and later nucleation of solid Si at the edge of the metal-Si alloy particle. Even though these early studies showed that *in situ* electron microscopy is a powerful tool to study the nucleation of semiconductor nanowires, they only focused on the formation of solid Si from Au-Si and Pd-Si alloy particle. In both cases, the only reaction involved was the dissociation of Si_2H_6 at the surface of the alloy particle. In the present study, we prove that a more complicated system, i.e., a system with more than one reaction involved during the growth of compound semiconductor nanowires, can be investigated by a careful design of the experiments, but requires a precise control of the introduction of gas precursors and the temperature of the sample.

5.2 Experimental Setup

An environmental transmission electron microscope (E-TEM), FEI Tecnai F-20, was employed for the simultaneous acquisition of atomic level chemical and structural information while introducing gases into the sample area at elevated temperatures. First, Au was sputtered at room temperature onto porous polycrystalline Si film (200 μm thickness) TEM grids. The Si grids were not pretreated to remove oxide layers prior Au deposition. These grids were then transported in air and introduced into the ESTEM column and heated to 480 ˚C, using a Gatan single-tilt heating holder* (T_{max} = 900 ˚C). This was followed by the introduction of 53.33 Pa (400 mTorr) of trimethylgallium (TMG) into the column for 2 minutes. The sample area and delivery lines were evacuated and purged to remove any residual TMG vapors. Next, the sample temperature was increased to 800 ˚C and 0.13 Pa to 5.33 Pa (0.4 x 10^{-3}Torr to 2 Torr) of ammonia (NH_3) was introduced into the ESTEM column. Low and high magnification images and digital videos with 15 frames per second time resolution were recorded using a Gatan Orius 600SC camera. A TEM/STEM JEOL F2010 was used for *ex situ* imaging and chemical analysis of the GaN nanowires formed during the *in situ* observations.

5.3 Results and discussion

Figure 5.1 shows a TEM image of Au particles deposited on a polycrystalline Si film after heating the sample to 480 ˚C. The speckle contrast in the high resolution electron microscopy (HREM) image (inset lower right hand corner in Figure 5.1) is characteristic of amorphous layers. There is no pre-

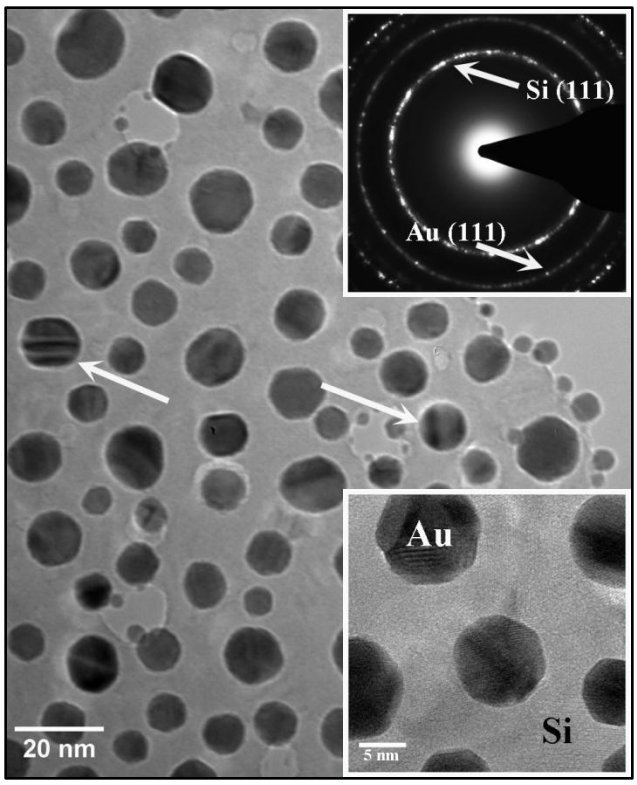

Figure 5.1. TEM image of Au particles on a polycrystalline Si film at 480 ˚C, the randomly distributed Au particles are faceted and exhibit banding contrast. The rings in the selected area diffraction pattern (inset in upper right hand corner) indicate the polycrystallinity nature of Au particles and the Si. The oxide amorphous layer is shown by the speckle contrast in the HREM image (inset in lower right hand corner).

treatment of the polycrystalline Si film before Au deposition or before introduction in the ESTEM column: exposing the sample to air produces a thin oxide layer on the polycrystalline Si film. The Au particles exhibit sizes ranging from 2 to 16 nm, and show a combination of faceting and banding contrast (indicated by arrows in Figure 5.1) that is consistent with particles being solid. The solid nature, as well as the polycrystallinity of the Au particles, is

corroborated by a diffraction pattern obtained at 480 ˚C (inset upper right hand corner in Figure 5.1).

The decomposition temperature of TMG is above 400 ˚C (Stringfellow, 1999). Thus, after the introduction of TMG into the sample area at 480 ˚C, the resulting Ga atoms dissolved into the Au solid particles and Au + Ga alloy droplets are observed to form (Figure 5.2). Initially, the newly formed droplets (marked i and ii in Figure 5.2 A) showed a rounded configuration, but as the TMG pressure increased, neighboring droplets experienced surface migration and coalescence, creating a new set of larger droplets with a tear drop configuration (marked i + ii in Figure 5.2 B). It appears that most of the small droplets were partially consumed by the large ones leaving a thin wetting layer along their migration path (indicated by arrows in Figure 5.2 B).

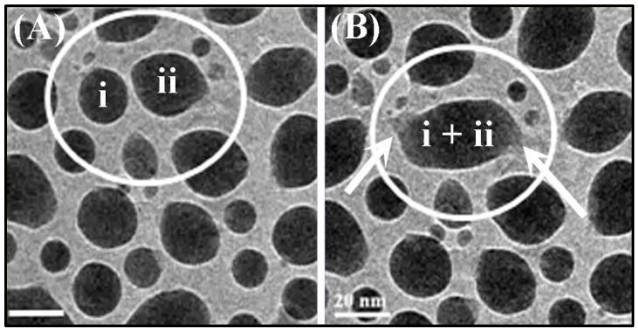

Figure 5.2. TEM images extracted from a digital video recorder during the introduction of TMG into the sample area at 480 ˚C. These images show the coalescence of neighboring Au + Ga droplets and formation of droplets with a tear drop configuration. (A) shows droplets (i - ii) before they coalesced and (B) shows the resulting larger droplet (i + ii) with tapered edges (indicated by arrows). The time difference between frames is less than a second for each case.

X-Ray energy-dispersive spectroscopy (EDS) analysis of these tapered droplets showed an average Ga content equal to 40 wt.%, which is within the liquid region in the Au-Ga phase diagram at 480 ˚C (Figure 5.3). EDS point measurements on several tapered droplets were performed in STEM mode. These measurements indicated that the relative concentrations of Ga and Au varied along the tapered droplets, with the concentration of Ga increasing from the droplet centers to the tapered edges (Figure 5.4).

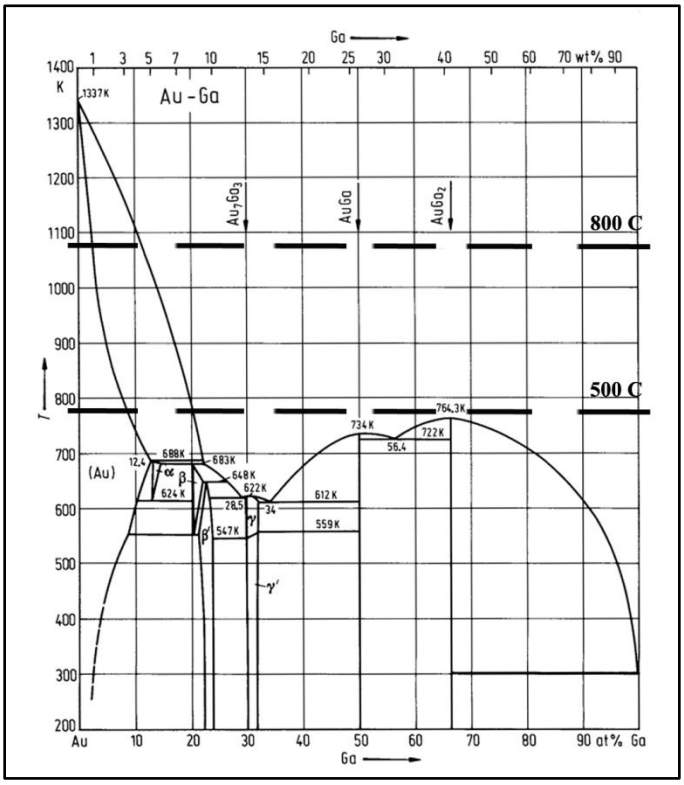

Figure 5.3. Au-Ga phase diagram. Dashed lines indicate the temperature at which the Au – Ga droplets were formed (500 ˚C) and the temperature at which the GaN nuclei were formed (800 ˚C) respectively (Predel & Madelung, 1991-1998).

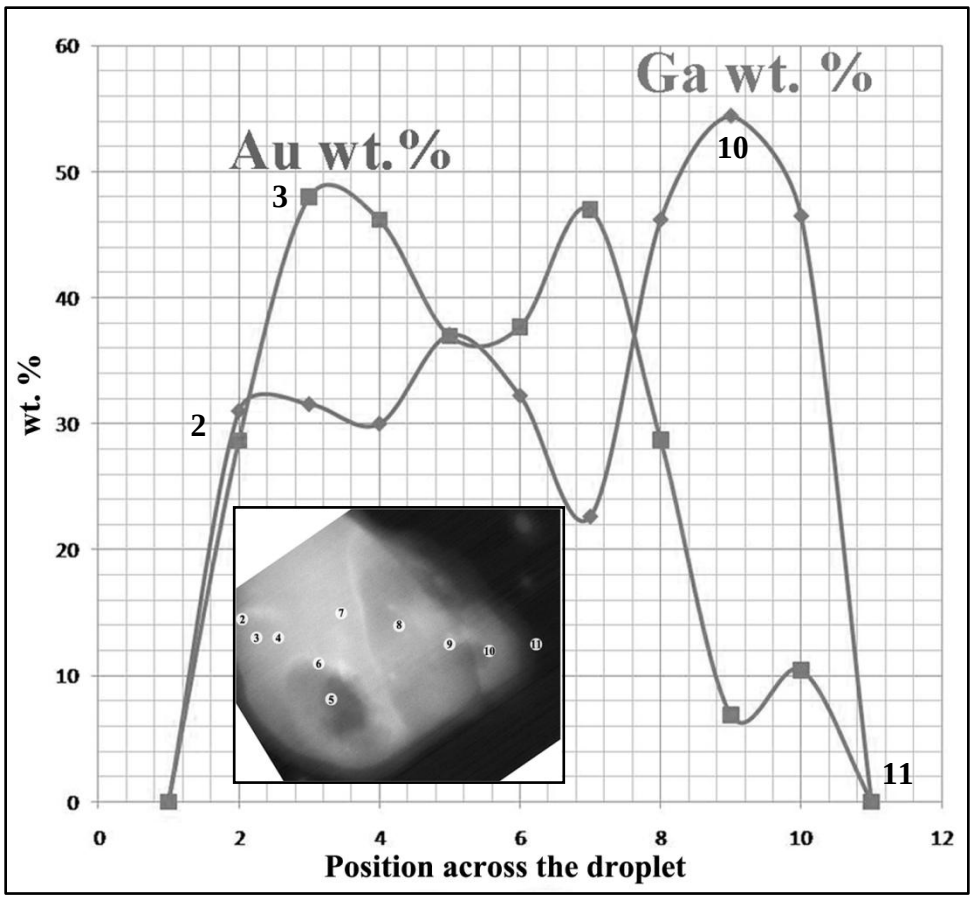

Figure 5.4. Graph showing the relative concentrations of Ga and Au along the tapered droplets. Inset shows a STEM image of the droplet with the positions were scan was performed.

Even though the Au + Ga tapered droplets were observed to experience some Ga evaporation while heating the sample to 800 ˚C, these droplets were liquid at all times. To further verify this, a series of diffraction patterns were taken during the formation of these tapered droplets. These diffraction patterns showed both Au and Si reflections before introducing TMG (Figure 5.5 A), and only Si reflections after both introducing TMG (Figure 5.5 B) and increasing the temperature to 800 ˚C (Figure 5.5 C). Also, HREM images of the Au + Ga

tapered droplets were recorded at 800 ˚C. Fast Fourier Transforms (FFT) from HREM images indicated that the lattice fringes observed at the tapered edge of the Au + Ga droplets correspond to the polycrystalline Si film underneath these droplets.

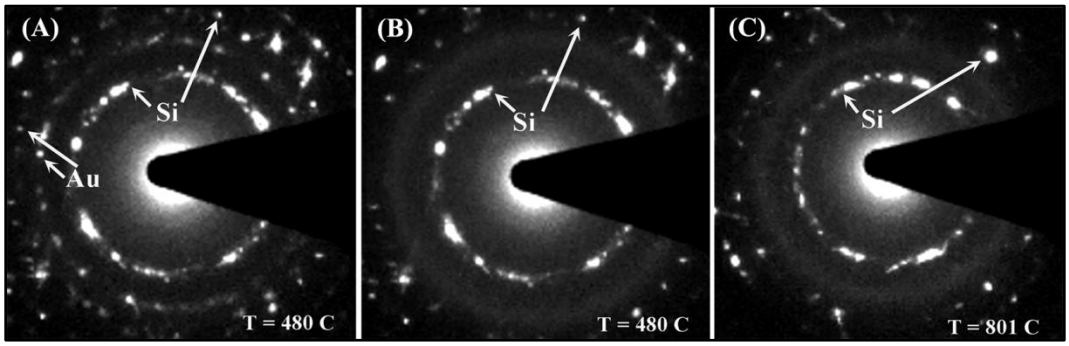

Figure 5.5. These are a series of diffraction patterns extracted from a digital video recorded during the formation of Au + Ga liquid droplets. (A) Au and Si reflections at 480 ˚C. There is an absence of Au reflections after (B) introduction of TMG at 480 ˚C and (C) heating the sample up to 800 ˚C.

Our observations indicated that GaN nanowires began to nucleate after 0.93 Pa (7 mTorr) of NH_3 was introduced into the sample area at 800 ˚C. This growth temperature was preferred for two reasons. First, even though growth of GaN by MOCVD starts at 450 ˚C (Nakamura S. , 1991), the crystallinity of GaN has been reported to improve by increasing the growth temperature up to 925 ˚C (MacKenzie, Abernathy, Stweart, & Muhr, 1996). The second reason was the upper temperature limit that is restricted by the TEM heating holder used for these experiments (T_{max} = 900 ˚C).

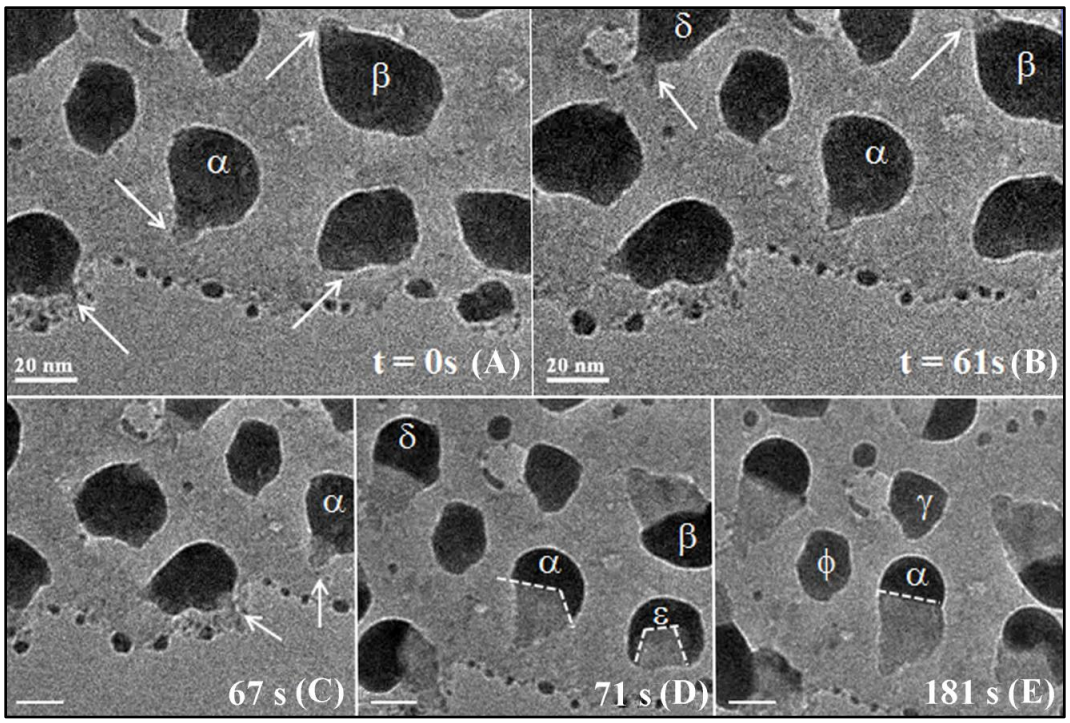

Figure 5.5. Sequences of frames extracted from a digital video recorded during the formation of GaN nuclei and their evolution into nanowires. (A) The tapered edges of the Au + Ga droplets, indicated with arrows, are still present at 800 ˚C. (B) First appearance of GaN nuclei (arrows) within particles β and δ after 61 s of introducing 0.933 Pa (7 mTorr) of NH_3. (C) Appearance of GaN nuclei within particle after 67 s. (D) GaN nanowires (α and ε) in early stages of growth presenting a multi-faceted droplet-nanowire interface. (E) GaN nanowires with no faceting (α) and with smaller number of facets (ε). Also in (E) particles ϕ and γ, with faceted shapes, do not formed GaN nuclei.

Sequences of frames extracted from one of the digital videos recorded during the formation of GaN nanowires are shown in Figure 5.6. It is clear from these images that the tapered edge of the Au + Ga droplets are still present after increasing the temperature to 800 ˚C (indicated by arrows in Figure 5.6 A). The

first GaN nuclei were observed to form within the tapered edges in droplets β and δ (Figure 5.6 B) after 60 s of introducing NH_3. As the growth continues, more GaN nuclei were observed to form in other droplets (α in Figure 5.6C).

An interesting feature observed was the faceting of the GaN nuclei at the droplet-nanowire interface. If we focus our attention on the nanowires formed from particles α and ε in Figure 5.6 D, we can see that particle α contains two facets, while particle ε contain three facets at the droplet-nanowire interface. As the nanowire grows these facets disappear for particle α and the interface becomes planar (Figure 5.6 E), whereas for the particle ε there is only a reduction in the number of facets (Figure 5.5 E) from three to two within the time were the video was recorded. The angle between the facets in Figure 5.6 D is ~130˚, which might correspond to the angle between M planes {01-10} and the high order planes {10-12}.

Another interesting observation is that particles ϕ and γ remain inactive for GaN nucleation (Figure 5.6 E). Chemical analysis of these particles, EDX measurements in STEM mode, indicated that these particles contain high concentration of Au, greater than 95 wt.%, which falls in the solid region of the Au – Ga phase diagram at 800 ˚C (Figure 3.3). To further corroborate the crystallinity of the faceted particles, FFT of high resolution images were taken at 800 ˚C. These patterns indicate that all the particles that remain inactive for GaN formation are crystalline (Figure 5.7). Thus, the inactivity of these particles could be attributed to their crystalline nature, which might cause N to diffuse at a very

slow rate or not diffuse at all into the solid. In either case, N does not dissolve appreciably in the solid particles and the solubility limit is not reached.

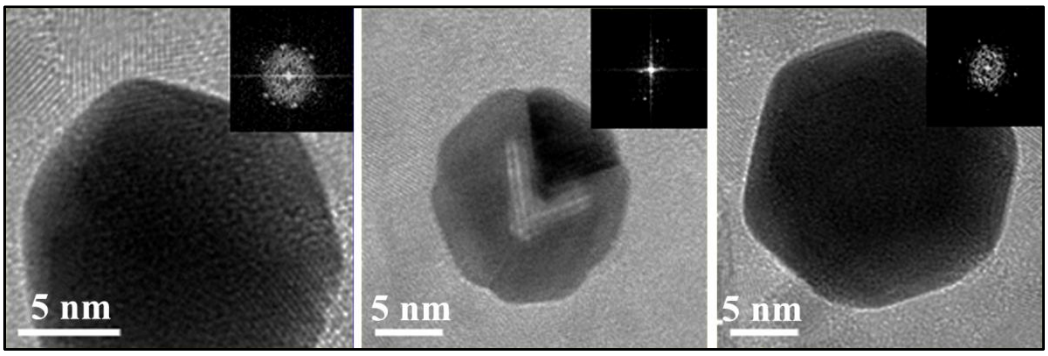

Figure 5.7. HREM images with respective FFT (inset) corroborating the crystallinity nature of the faceted particles that did not form GaN nuclei. These images were taken at 800 ˚C.

The GaN nuclei contained both Ga and N as shown by *in situ* electron energy loss spectroscopy (EELS) (Figure 5.8). The EELS spectrum was taken at 800 ˚C in high vacuum mode after evacuating the gases from the sample area and the measurements were performed on individual nuclei. Additionally, selected area diffraction patterns (Figure 5.9) show that these nuclei have wurtzite structure, characteristic of GaN.

Based on the *in situ* observation described above, the nucleation of GaN nanowires may be rationalized by referring to a schematic shown in Figure 5.10. Thermal decomposition of NH_3 starts at 400 ˚C (Stringfellow, 1999). Therefore, when NH_3 is introduced into the system at 800 °C, it decomposes and the resulting N atoms dissolve into the Ga + Au tapered droplet. Additional incorporation of N atoms creates a situation depicted in Figure 5.10 B, where the tapered edge of the droplet has a higher concentration of N than that in the rest of

droplet. As a result, the solubility limit of N in the tapered edge is exceeded first, and the Ga and N atoms inside this region come together to form a GaN nucleus. The Au atoms that exceed the solubility limit of Au into GaN nucleus are expelled into the attached liquid droplet, creating a situation as illustrated in Figure 5.10 C. Using the arguments similar to those used above, additional growth of GaN occurs leads to the migration of the droplet-nanowire interface.

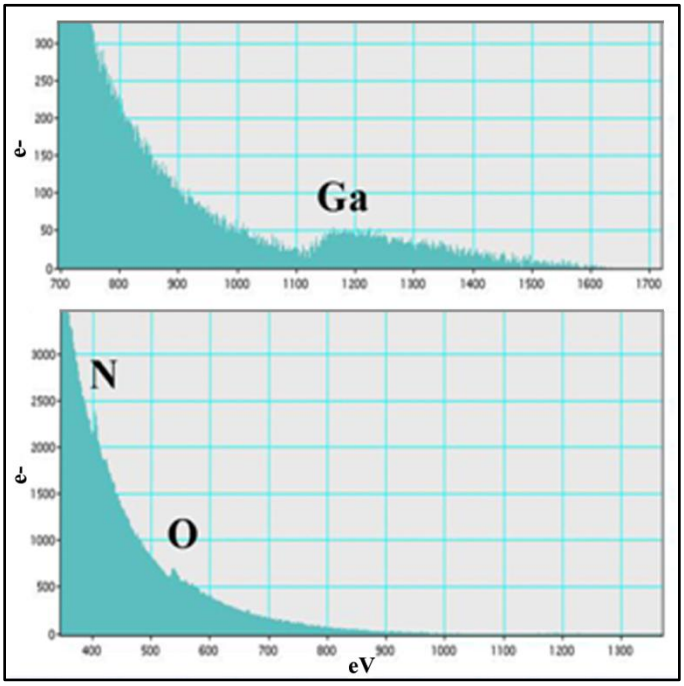

Figure 5.8. In situ EELS spectrum of individual nuclei recorded without any gas in the sample area at 800 ˚C. This spectrum shows the characteristic peaks for Ga and N. The oxygen peak is attributed to the oxygen present on the SiOx film where the GaN nuclei is sitting on.

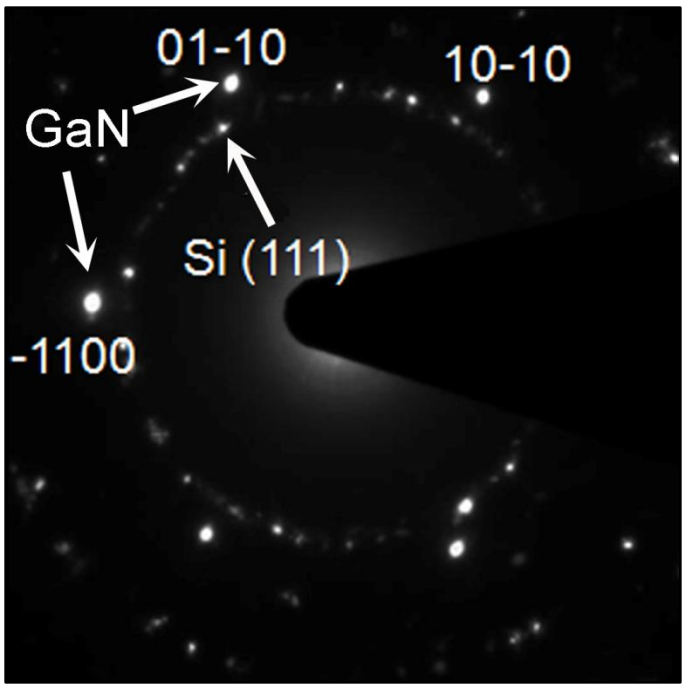

Figure 5.9. SAD pattern obtain from a single GaN nucleus on the polycrystalline Si film.

In addition, faceting might result from external perturbations, such as the evaporation of Ga or absorption of N at the tapered edge, or as the result of the surface being thermodynamically unstable. According to a theory developed by Herring (1951), surfaces other than those found on the equilibrium crystal shape will decompose into a hill-and-valley structure in order to reduce the overall surface free energy. Thus, the first to grow GaN nuclei might not have the same orientations and when they coalesce, a faceted solid-liquid interface could be created. As the nanowire grows, some of the grains win out leading to vicinal facets. These facets are not atomically flat, and some of them must have higher interfacial energy than others. Then steps on facets with higher interfacial energy

move laterally, faster than the steps on facets with lower energy, leading to the formation of a planar interface as shown in Figure 5.6 E.

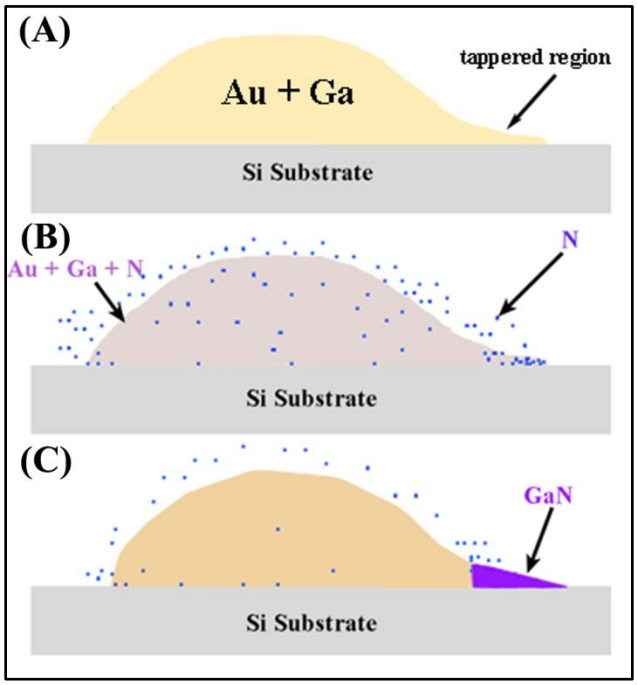

Figure 5.10. Schematic showing (A) the Au + Ga droplet before NH_3 was introduced into the sample area, (B) the arrival of N atoms onto the surface of the Au + Ga droplets and substrate, and the accumulation of N inside the thin film region, and (C) the formation of GaN nuclei when the solubility limit of N is exceeded in thin film region..

In addition, faceting might result from external perturbations, such as the evaporation of Ga or absorption of N at the tapered edge, or as the result of the surface being thermodynamically unstable. According to a theory developed by Herring (1951), surfaces other than those found on the equilibrium crystal shape will decompose into a hill-and-valley structure in order to reduce the overall

surface free energy. Thus, the initial GaN clusters clusters might not have the same orientations and when they coalesce, a faceted solid-liquid interface could be created. As the nanowire grows, some of the grains win out leading to vicinal facets. These facets are not atomically flat, and some of them must have higher surface energy than others. Then steps on facets with higher surface energy move laterally, faster than the steps on facets with lower energy, leading to the formation of a planar interface as shown in Figure 5.6 E.

5.4 Conclusions

GaN nanowires growth was successfully achieved by first forming Au + Ga droplets and subsequently exposing them to NH_3. High magnification images of the formation of GaN nuclei were obtained using an environmental transmission electron microscope. Chemical and structural analysis confirmed that these nuclei were GaN having the wurtzitic structure.

Several interesting observations emerge from this study. First, the coalescence of the Au + Ga droplets leads to the formation of tapered droplets that wet the underlying oxide layer on the Si substrate. Second, the nucleation and growth of GaN nanowires occur only within liquid droplets following the well know VLS mechanism. GaN nuclei were not observed to form within Au + Ga solid particles, which could be attributed to the reduced solubility of N within these solid particles. Third, under these particular growth conditions, the origin of the GaN nuclei is at the tapered edge of the Au + Ga droplets. Finally, at early stages of growth, there is more than one facet of the droplet - nanowire interface, which might be related to the thermal instability within the tapered droplet.

Additional GaN growth continues by step propagation on the interface, resulting in a planar interface.

In order to use compound semiconductor nanowires as building blocks for nanoscale devices, a precise control of the nanowire structure, crystallinity, morphology, and chemistry is necessary. This could be achieved by first understanding the nucleation and growth of compound nanowires. These findings suggest that our approach can be used for this purpose and can be extended to other binary semiconductor compound such as GaP, GaAs, and InP, or even ternary compounds such as InGaN. However, further experimental work is required to fully elucidate the kinetic effects on the growth process and effects of temperature and pressure on the crystallinity and morphology of nanowires.

CHAPTER 6

GROWTH OF GAN NANOWIRES WITH

6.1 Introduction

As discussed earlier, owing to their unique physical properties, group III-Nitride nanowires are considered ideal building blocks for the fabrication of optoelectronic devices. However, the synthesis of nanowires with predictable physical properties is still a major concern for reliable device integration. In order to control the dimensions, morphology, crystallinity, and chemical composition of nanowires, a detail understanding of the nucleation and growth at the nanoscale is extremely important. Most frequently, growth of semiconductor nanowires is promoted by metal particles following the previously described VLS and VSS mechanism (Wagner & Ellis, 1964) (Kodambaka S. , Tersoff, Reuter, & Ross, 2007). Despite significant amount of research on the growth of GaN nanowires, many aspects involved during growth of these nanowires remain unresolved. For example, the phase of the metal particle, and thus, the growth mechanism are still under investigation and debate. Some research groups claim that GaN nanowires grown following the VLS mechanism (Kuykendal, Pauzauskie, Lee, Zhang, Goldberger, & Yang, 2003) (Weng, Burke, & Redwing, 2009), however, just recently Cheze et al. has demonstrated using low energy electron microscopy that GaN nanowires nucleate from the solid (2010). Other important aspects of growth are, for example, the rate-limiting process, the evolution of the particle-nanowire interface, the dependence of growth on pressure and temperature as well as nanowire's diameter.

Recently, *in situ* electron microscopy has been utilized to obtain direct evidence of the state of the metal particle (Kodambaka S. , Tersoff, Reuter, & Ross, 2007), the growth dependence on nanowire's diameter (Kodambaka, Tersoff, Reuter, & Ross, 2006), and the evolution of the particle-nanowire interface (Hofmann, et al., 2008) (Wen, Reuter, Tersoff, Stach, & Ross, 2010) for the metal-assisted growth of Si and Ge nanowires. In the present study, we prove that the growth of compound semiconductor nanowires – where the nucleation and growth processes are expected to be more complex since more elements are involved – can be investigated by a careful design of the experiments, but requires a precise control of the introduction of the gas precursors and temperature of the sample.

In the previous chapter, *in situ* electron microscopy was used to obtain direct observations of nucleation and early stages of growth of GaN nanowires. These nanowires were grown by first forming Au + Ga alloy droplets and subsequently exposing these droplets to NH_3. These observations offered important information regarding the shape and phase of the alloy droplets, the nature of the nucleation sites, and profile and evolution of the newly formed droplet-nanowire interface. In this chapter, we report evidence of the state of the metal particle and the evolution of the droplet-nanowire interface during the growth stage, after the nucleation stage was completed. Also, we investigated the growth rate dependence on pressure as well as nanowire's diameter, concluding that the rate limiting step is the incorporation of growth species, from the vapor onto the vapor-liquid interface or the vapor-liquid-solid boundary. These

experiments follow a similar experimental setup that the one described in Chapter 5, the only difference is that, in this case, the NH_3 pressure is increased up to 2 Torr.

6.2 Results

After the nucleation stage was complete, *in situ* observations on several samples showed that the growth stage started over a range of NH_3 pressures (P_{NH_3}) from $10x10^{-3}$ to $70x10^{-3}$ Torr at 800 ˚C. The maximum NH_3 pressure during growth was about 2 Torr and temperatures ranged from 770 – 850 ˚C. NH_3 was leaked continuously into the microscope column to ensure a constant NH_3 pressure during nanowire growth. Also, the electric current of the heating holder was controlled manually to ensure a constant temperature. Figure 6.1 is a low magnification TEM image acquired after nanowire growth at P_{NH_3} =1.75 Torr and T = 805 ˚C. Nanowires are observed over the entire surface of the sample, even in those areas with no electron beam irradiation, this eliminates the possibility of electron beam influence on nanowire growth. Nanowires grow with a Au + Ga particle sitting on their tip and the majority of nanowires that leave the SiO_x film grow with straight sidewalls and in different directions. Only the growth of nanowires with straight sidewalls was studied in this work.

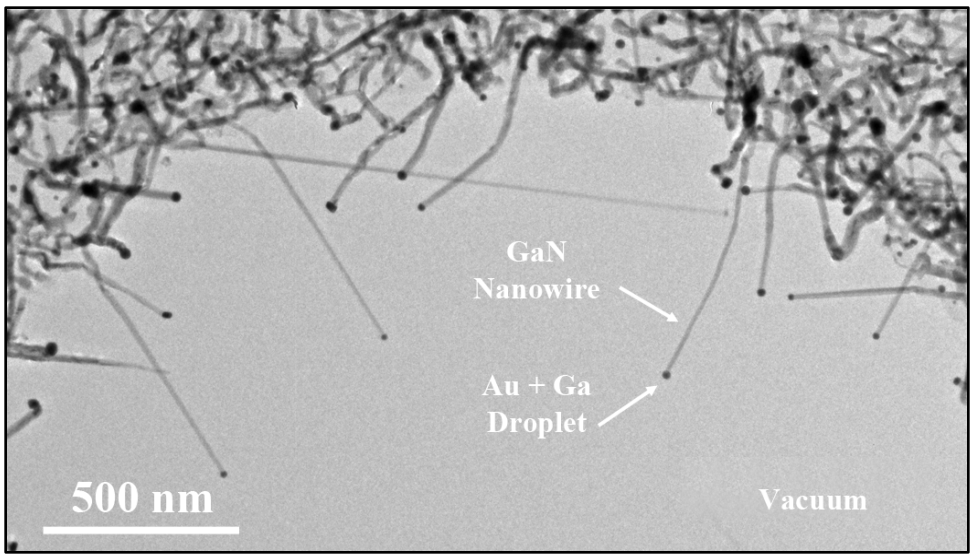

Figure 6.1. Low magnification TEM image taken after nanowire growth at P_{NH3} = 1.75 Torr and T = 805 ˚C. Nanowires are observed over the entire sample, indicating that the electron beam does not affect the nanowire growth.

The nanowires obtained in these experiments contained both Ga and N as shown by both *in situ* EELS and *ex situ* EDX analysis in Figure 6.2. The EELS spectrum was taken at 800 ˚C in high vacuum mode after evacuating the gases from the sample area, and the EDX spectrum was taken in STEM mode at room temperature. Both techniques were performed on individual nanowires. The STEM image in the inset in Figure 6.2 shows the difference in contrast between the nanowire and the metal particle, which is sitting on the tip of the nanowire. Chemical analysis of the metal particles indicated Ga concentrations ranging from 2 to 20 at%.

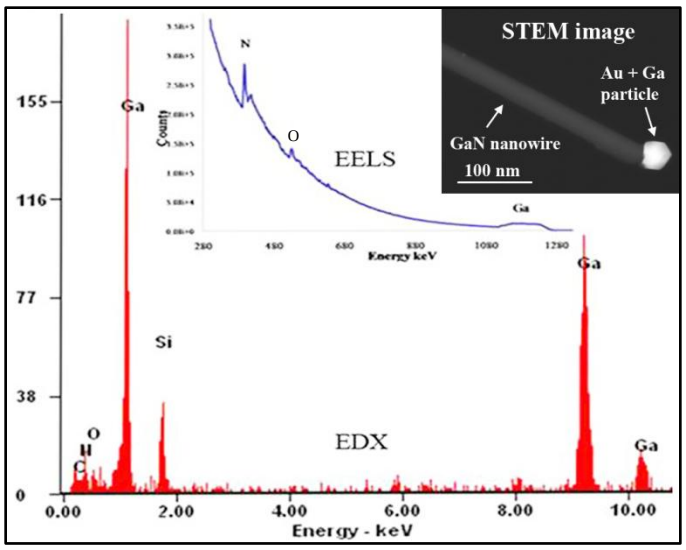

Figure 6.2. In situ EELS as well as ex situ EDX analysis shows that the nanowires obtained in this experiments contained both Ga and N. STEM image (inset) shows the difference in contrast between the nanowire and the metal particle, which is sitting on the nanowire tip. EDX analysis of the metal particles indicated a high content of Au within the particle. The oxygen pick observed in the EELS spectrum might be attributed to oxygen contamination in the sample area.

High resolution TEM images (Figures 6.3 A - D) show that these nanowires are single crystal and the corresponding fast Fourier transform (FFT) (inset in Figures 6.3 A - D) indicates that their structure is wurtzite, which is the characteristic crystalline structure of GaN. Nanowires with straight sidewalls have diameters ranging from 6 to 40 nm with hexagonal or truncated triangular cross sections. Additional analysis indicates that those nanowires with diameters ranging from 6 to 40 nm grow in the <10-10> directions.

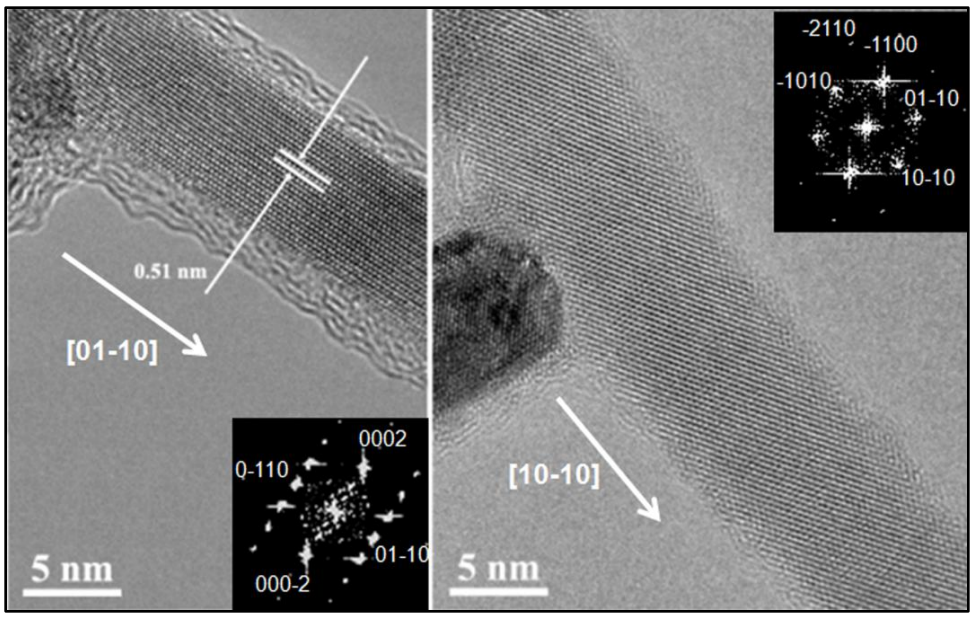

Figure 6.3. High resolution images indicate that the nanowires are single crystal and the corresponding FFT (insets) show that their structure is wurtzite, characteristic of GaN. Single crystal nanowires grew in the <10-10> directions preferentially.

Figure 6.4 shows a bright-field TEM images acquired during GaN nanowire growth at constant temperature and NH_3 pressure. Under these growth conditions, GaN nanowires grow with a droplet (wire 2 and 3) or solid particle (wire 1) sitting on their tip. The Au + Ga droplets show a smoothly curved surface while the Au + Ga solid particle shows a faceted surface during growth (inset in Figure 6.4 A). The measured diameters for wire 1, 2, and 3 are 10, 17, and 18 nm, respectively. Nanowires were observed to grow in a direction perpendicular to the droplet-nanowire interface. Additionally, chemical quantification of the droplets indicated that the Ga content ranges from 7 to 18 at%.

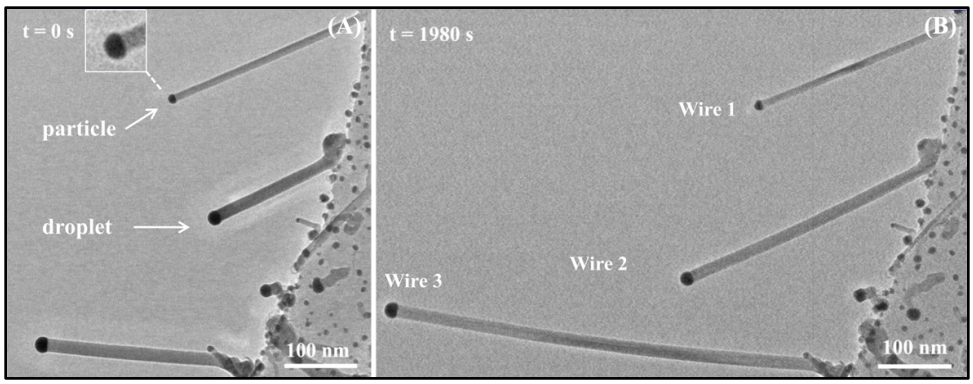

*Figure 6.4. Bright-field TEM images taken during growth of GaN nanowires at constant temperature and pressure ($\boldsymbol{P_{NH3}}$ = 6.52 x 10^{-2} Torr and **T** = 813 ˚C). Nanowires grow with straight sidewalls with Au + Ga droplets or solid particles sitting on their tip.*

Further analysis indicated that over the life time of nanowire growth, the growth rate varies with diameter. Nanowire diameters were observed to decrease with time; this might be attributed to the continued consumption of Ga atoms from the droplet and also to the diffusion of Au atoms away from the droplet. The measured length and diameter vs. time for a particular nanowire are shown in Figure 6.5. In this short period of time (300s), the diameter only decreased about 6% of its original value and length increase seemed to be constant. However, for a longer growth of time (about 17 x 10^3 s), the diameter decreased about 20% of its original value and the nanowire growth rate is affected significantly. Figure 6.6 shows the calculated volumetric growth rate and diameters vs. time for the same nanowire shown in Figure 6.5 with a longer growth time. Nanowires in this experiment were grown P_{NH3} = 1.7 x 10^{-1} Torr and T = 811 ˚C.

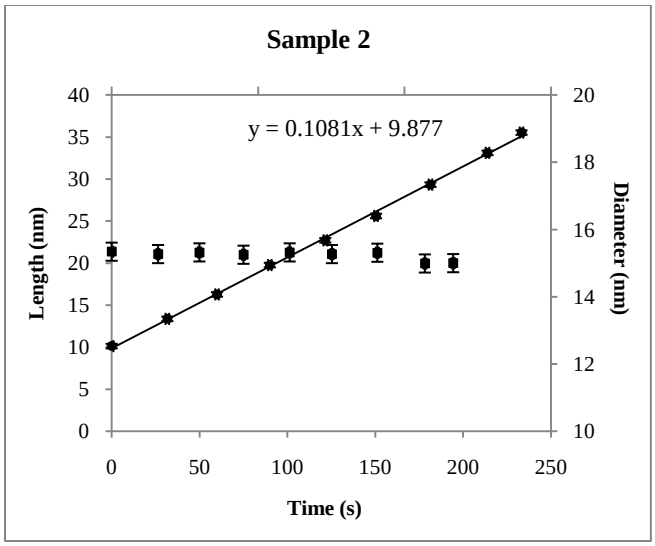

Figure 6.5. Plot of measured length and diameter vs. time for a nanowire grown at $\boldsymbol{P_{NH3}}$ *= 1.7 x* 10^{-1} *Torr and T = 811 ˚C. The nanowire's diameter decreases while its length increases over time at constant rate.*

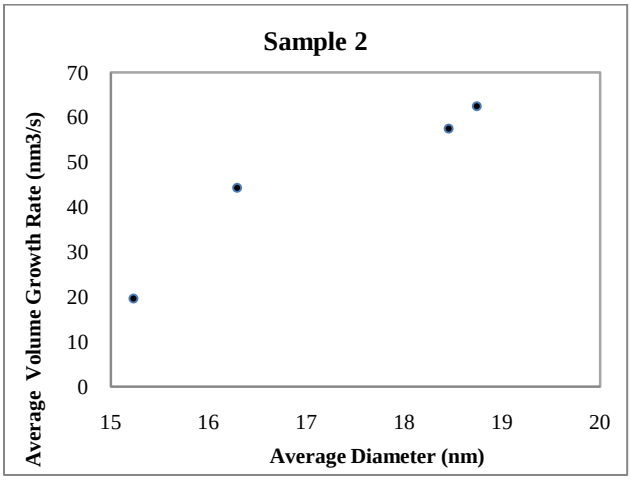

Figure 6.6. Average volumetric growth rate as a function of time for a particular nanowire in sample 1. There is a clear decrease in the growth rate with diameter.

Additional analysis permitted to compare the growth rate of a group of nanowires with different diameters. Figure 6.7 shows a plot of the volumetric growth rate and average diameter of nanowires grown at constant NH_3 pressure

and temperature ($\boldsymbol{P_{NH3}}$ = 6.52 x 10^{-2} Torr and $\boldsymbol{T}$ = 813 ˚C). Even though there is some scatter in the graph, there is a visible reduction of the growth rate with decreasing diameter.

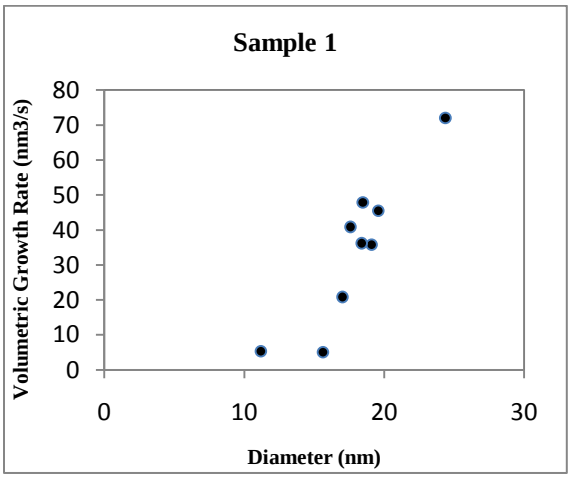

Figure 6.7. Plot of volumetric growth rate vs. diameter for GaN nanowires grown at constant pressure and temperature (P_{NH3} = 6.52 x 10^{-2} Torr and T = 813 ˚C).

Additionally to these results, *in situ* observations also allowed us to monitor the events of the droplet-nanowire interface. Due to the lower diffusivity of Au in GaN (D_o = 1.55 x 10^{-7} cm^2/s^{-1}) compare to other semiconductor materials – for example the diffusivity of Au in Si is D_o = 2.44 x 10^{-4} cm^2s^{-1} – Au forms sharp interfaces with GaN (Kang, Li, Gong, & Jiang, 2003), thus allowing us to observe the evolution of these sharp droplet-nanowire interfaces. Figure 6.8 shows a sequence of frames extracted from a digital video recorded during nanowire growth at constant NH_3 pressure and temperature (P_{NH3} = 1.35 x10^{-1} Torr and T = 797 ˚C). The movement of the droplet-nanowire interface is indicated by arrows in Figure 6.8 A-C). The evolution of the interface occurs by

ledge flow parallel to the interface. Calculations of the volumetric growth rate of the nanowire using the measured ledge linear growth rate (1.16 nm/s) result in a volumetric growth rate of 29 nm^3/s. However, the volumetric growth rate calculated using the measured nanowire axial growth rate (0.2153 nm/s) is 58 nm^3/s. Same calculations were made for a second nanowire (Figure 6.8) grown under different growth conditions (P_{NH3} = 7.36 $x10^{-1}$ Torr and T = 798 ˚C). In this case, the volumetric growth rate calculated by using both the measured ledge linear growth rate and nanowire axial growth rate are the same.

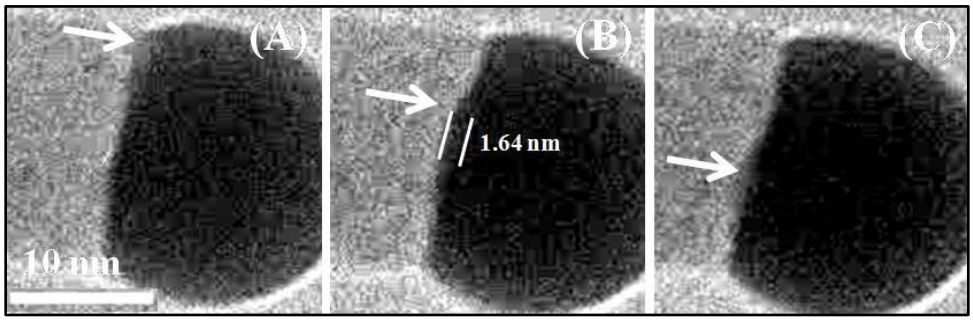

Figure 6.8. Sequence of frames extracted from a digital video taken during growth of GaN nanowires at constant pressure and temperature (P_{NH3} = 7.36 x 10^{-1} Torr and T = 798 ˚C). The ledge motion parallel to the droplet-nanowire interface is observed is this video.

6.3 Discussions

Under these particular growth conditions, our observations are direct evidence of the state of the alloy particle– liquid and solid. Thus, nanowires grow following both the VLS and VSS mechanism. This could be explained by considering the composition of the metal particles. Solid phases appeared because Ga is consumed from the droplet. The solubility of Ga in Au is 4 at% at 800 ˚C,

thus solid particles contain enough Ga to contribute to nanowire growth. Nanowires that were grown following the VSS mechanism grew at slower rates (~0.5 nm^3/s) than the growth rates of nanowires grown by the VLS mechanism (~20 to 40 nm^3/s).

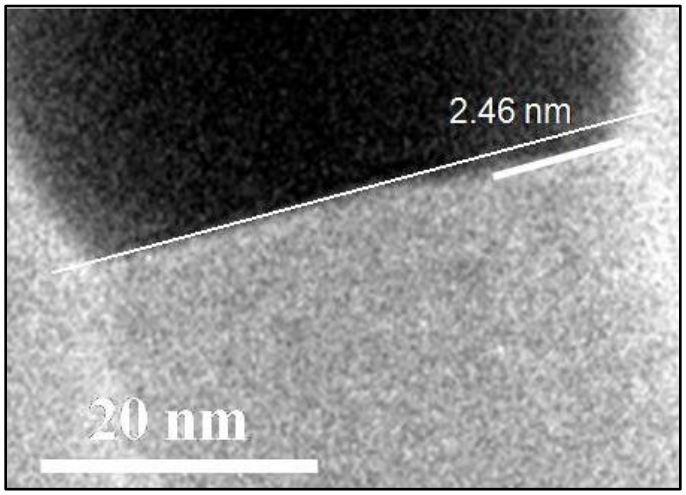

Figure 6.9. GaN nanowire grown under P_{NH3} = 7.36 x10^{-1} Torr and T = 798 ˚C. Ledge flow parallel to the droplet-nanowire interface was also observed in this case.

The classical analysis of Givargizov (1975) concluded that narrower wires should grow more slowly due to the Gibbs-Thomson effect, with a critical diameter below which growth cannot occur. Our experimental measurements for GaN nanowires confirm this behavior. The Gibbs-Thomson effect relates the surface curvature to vapor pressure. Droplets with smaller diameter have higher vapor pressure above the droplet than droplets with larger diameter. An increase on the vapor pressure decreases the supersaturation of the system. Recalling the expression of supersaturation from Chapter 3: $\boldsymbol{S = p/p_\infty}$, thus, an increase in the vapor pressure of the droplet ($\boldsymbol{p}$) decreases the supersaturation of the system,

decreasing the driving force for growth, and thus the growth rate. This indicates that under these growth conditions the rate-limiting growth step is the incorporation of the vapor into the liquid or triple boundary.

As indicated before, the VLS and VSS mechanisms follow the same concept, that is, preferential nucleation at the triple phase boundary. Wacaser and coworkers review thermodynamic and kinetic theory involved during nanowire growth (Wacaser et al., 2008). The highlights of this review were mentioned in Chapter 3. In this paper, the authors concluded that the Gibbs free energy can be minimized at the triple phase boundary. This means that the boundary in which the liquid droplet, the crystalline nanowire, and the vapor growth species meet is a preferential site for nucleation of the growth species. According to our experimental observations, preferential growth at the triple phase boundary might be thought of as follows. The alloy droplet acts as catalyst for NH_3 decomposition. Decomposition of NH_3 must happen at the tip of the wires and the resulting N atoms diffuse on the surface towards the triple phase boundary. Nitrogen diffusion through the particle is discarded since nitrogen does not dissolve into liquid or solid Au, and only 0.001 % dissolves into molten Ga (Stringfellow, 1999). Additionally, chemical analysis of the alloy particles on the nanowires' tip indicated that these particles only contain Au and Ga. Thus, N is more likely to react with Ga on the surface of the droplet or at the droplet-nanowire interface.

6.4 Conclusions

Our *in situ* observations indicated that GaN nanowires grow by both the VLS and VSS mechanism. The consumption of Ga atoms from the Au + Ga droplet during VLS growth causes the droplet to become reach in Au and solidify. Then, nanowire growth continues via the VSS mechanism until Ga is depleted completely from the droplet. Nanowire growth rate decreased with decreasing diameter. This is attributed to the Gibbs-Thompson effect, where small droplets have higher vapor pressure than big droplets. Higher vapor pressure reduces the supersaturation of the system, decreasing the nanowire growth rate. Under these growth conditions the rate-limiting growth step is the incorporation of the vapor into the liquid or triple boundary. Additionally, study of the droplet-nanowire interface indicated that the interface advances in the same direction of the nanowire by ledge flow parallel to the interface.

In order to develop a growth method for the synthesis of nanowires of desired material, it is important to understand the effects of the experimental parameters on the size, shape, and crystallinity of the nanowires, as well as the ease of tailoring the synthesis to form nanowire heterostructures. Further experimental work is required to fully elucidate the effects of, for example, temperature and pressure on the growth process.

REFERENCES

Abrams, M., & McBain, J. (1944). A closed cell for electron microscopy. *Journal of Applied Physics , 15*, 607.

Adachi, S. (2005). *Properties of Group-IV, III-V, and II-VI.* West Sussex: Wiley.

Amano, H., Kito, M., Hiramatsu, K., & Akasaki, I. (1989). P-type conduction in Mg-doped GaN treated with low-energy electron beam irradiation (LEEBI). *Jap. J. Appl. Phys. Part 2 Lett. , 28*, L2112-L2114.

Amano, H., Sawaki, N., Akasaki, I., & Toyoda, Y. (1986). Metalorganic vapor-phase epitaxial-growth of a high-quality GaN film using an AlN buffer layer. *App. Phys. Lett. , 48*, 353-355.

Ashcroft, N. W., & Mermin, D. N. (1976). *Solid State Physics.* Philadelphia: Saunders College Publishing.

Baker, R. T., Thomas, R. B., & Wells, M. (1975). Controlled Atmosphere Electron Microscopy Studies of Graphite Gasification - The Catalytic Influence of Vanadium and Vanadium Pentoxide. *Carbon , 13*, 141-145.

Bao, J. e. (2008). Optical properties of rotationally twinned InP nanoiwre heterostructures. *Nano Letters , 8*, 836-841.

Bjork, M. T., J, O. B., T, S., Al, P., C, T., H, M. M., et al. (2002). One-dimensional heterostructures in semiconductor nanowhiskers. *Applied Physics Letters , 80*, 1058-1060.

Borgstrom, M., Deppert, K., Samuelson, L., & Seifert, W. (2004). *J. Cryst. Growth , 260*, 18.

Boyes, E. D., & Gai, P. L. (1997). Environmental high resolution electron microscopy and application to chemical science. *Ultramicroscopy , 67*, 219-232.

Brydson, R. (2002). *Electron Energy Loss Spectroscopy.* Oxford: BIOS Scientific Publisers Ltd.

Brydson, R. M., & Hammond, C. (2005). Generic methodologies for nanotechnology: classification and fabrication. In R. W. Kelsall, I. W. Hamley, & G. Mark, *Nanoscale Science and Technology* (pp. 1-54). West Sussex: John Wiley & Sons, Ltd.

Buffat, P., & Borel, J.-P. (1976). Size effect on the melting gold of particles. *Phys. Rev. A , 13*, 2287-2298.

Burton, W. K., Cabrera, N., & Frank, F. C. (1951). The growth of crystal and the equilibrium structure of their surfaces. *Phil. Trans. Soc. London , 243*, 299-358.

Butler, E. P., & Hale, K. F. (1981). *Dynamic Experiments In The Electron Microscope* (Vol. 9). (A. M. Glavert, Ed.) Amsterdam: North-Holland Publishing Company.

Cao, G. (2004). *Nanostructures and nanomaterials: synthesis, properties and aplications.* London: Imperial College Press.

Caroff, P., Dick, K. A., Johansson, J., Messing, M. E., Deppert, K., & Samuelson, L. (2008). Controlled polytypic and twin-plane superlattices in III-V nanowires. *Nature Nanotechnology , 4*, 50-55.

Chen, X., Li, J., Cao, Y., Lan, Y., Li, H., He, M., et al. (2000). *Ad. Mater. , 12*, 1432.

Cheze, C., Geelhaar, L., Trampert, A., Olvier, B., & Riechert, H. (2010). Collector Phase transition during Vapor-Solid-Solid Nucleation of GaN Nanowires. *NanoLetters , 10*, 3426-3431.

Chung, S., Yu, J., & Heath, J. R. (2000). Silicon nanowire devices. *Applied Physics Letters , 76*, 2068-2070.

Clark, S. (1996, October 31). *Band Structures*. Retrieved November 30, 2010, from Modelling complex strcutures: http://cmt.dur.ac.uk/sjc/thesis/thesis/node39.html

Daniel, M.-C., & Astruc, D. (2004). Gold Nanoparticles: Assembly, Supramolecular Chemistry, Quantum-Size-Related Properties, and Applications toward Biology, Catalysis, and Nanotechnology. *Chem. Rev. , 104*, 293-346.

Davydoc, A. V., Boettinger, W. J., Kattner, U. R., & Anderson, T. J. (2001). Thermodynamic Assesment of Gallium-Nitrdogen System. *Phys. Stat. Sol (a) , 188*, 407-410.

Diaz, R. E., Sharma, R., Jarvis, K., Zaidi, Z., Zhang, Q., & Mahajan, S. (Submitted). Direct observations of Nucleation and early stages of growth of GaN nanowires. *Journal of Crystal Growth* .

Dick, K. (2008). A review of nanowire growth promoted by alloys and non-alloying elements with emphasis on Au assisted III-V nanowires. *Progress in Crystal growth and Characterization of Materials , 54*, 138-173.

Dick, K. A., Caroff, P., Bolinsson, J., Messing, M. E., Johansson, J., Deppert, K., et al. (2010). Control of III-V nanowire crystal structure by growth parameter tunning. *Semiconductor Science and Technology , 25*, 024009.
Dovidenko, K., Oktyabrsky, S., & Narayan, J. (1997). *J. Appl. Phy. , 82*, 4296.

Duan, X., & Lieber, C. M. (2000). *J. A. Che. Soc , 12*, 188.

Duan, X., Huang, Y., Cui, Y., Wang, J., & Lieber, C. M. (2001). Indium Phosphide nanowires as building blocks for nanoscale electronic and optoelectronic devices. *Nature , 409*, 66-69.

Elwell, D., & Elwell, M. M. (1988). Crystal Growth of Gallium Nitride. *Prog. Crystal Growth and Charact , 17*, 53-78.

Ferhat, M., Zaoui, A., Certier, M., & Khelifa, B. (1996). Empirical Tight-Binding Band Structure of Zinc-Blende Nitrides GaN, AlN, and BN. *Phys. Stat. Sol. (b) , 195*, 415.

Feyman, R. P. (1959, December 29). *There's Plenty of Room at the Bottom.* Retrieved August 27, 2010, from Nanotechnology: http://www.zyvex.com/nanotech/feynman.html

Gai, P. L. (1999). Environmental high resolution electron microscopy of gas-catalyst reactions. *Topics in Catalysis , 8*, 97-113.

Gai, P. L. (1997). *In-Situ microscopy in Materials Research.* Kluwer Academic Publishers.

Givargizov, E. I. (1975). Fundamental Aspects of VLS growth. *Journal of Crystal Growth , 31*, 20-30.

Goldberger, J., Sirbuly, D. J., Law, M., & Yang, P. (2005). ZnO nanowire transistors. *Journal of Physical Chemestry B , 109*, 9-14.

Gorczyca, I., & Christensen, N. E. (1993). Band structure and high-pressure phase transition in GaN, AlN, InN, and BN. *Physica B: Condensed Matter , 183*, 410-414.

Gudiksen, M. S., J, L. L., J, W., C, S. D., & M, L. C. (2002). Growth of nanowire superlattice structures for nanoscale photonics and electronics. *Nature , 415*, 617-620.

Haider, M., Rose, H., Uhlemann, S., Kabius, B., & Urban, K. (1998). Towards 0.1 nm resolution with the first spherically corrected transmission electron microscope. *Journal of Electron Microscopy , 47*, 396-405.

Harriot, L. R., & Hull, R. (2004). Nanolithography. In M. Di Ventra, S. Evoy, & J. R. Heflin, *Introduction to Nanoscale Sience and Technology* (pp. 7-40). Boston: Kluwer Academic Publishers.

Herring, C. (1951). *Phys. Rev. , 82*, 87.
Hess, K. (2007). Room at the Bottom, Plenty of Tyranny at the Top. In W. A. Goddard, D. W. Brenner, S. E. Lyshevski, & G. J. Iafrate, *Handbook of Nanoscience, Engineering, and Technology* (Second Edition ed., pp. 2.1-2.2). New York: CRC Press Taylor & Francis Group.

Hirsch, P., Horne, R., & Whelan, M. (1956). Direct Observation of the Arragment and Motion of Dislocations in Aluminium. *The Philosophical Magazine , 1*, 677.
Hofmann, S., Sharma, R., Wirth, C. T., Cervantes-Sodi, F., Ducati, C., Kasama, T., et al. (2008). Ledge-flow-controlled catalyst interface dynamics during Si nanowire growth. *Nature , 8*, 372.

Hull, D., & Bancon, D. J. (1984). *Introduction to dislocations.* Oxford: Pergamon.

Ijima, S., & Ichihashi, T. (1993). Single-Shell carbon nanotubes of 1nm diameter. *Nature , 363*, 603-605.

Inoue, Y., Hoshino, T., Takeda, S., Ishino, K., Ishida, A., & Fujiyasu, H. (2004). *Appl. Phys. Lett. , 85*, 2340.

Jefferson, D. (2008, 01 01). *Dr. David Jefferson web page at University of Cambridge, Department of Chemestry*. Retrieved 09 10, 2010, from Department of Chemstry, University of Cambridge: http://www.ch.cam.ac.uk/staff/daj.html

Johnson, J. C., Choi, H., Knutsen, K. P., Schaller, R. D., Yang, P., & Saykally, R. J. (2002). Single GaN nanowires lasers. *Nature Materials , 1*, 106-110.

Johnson, W. C., Parsons, J. B., & Crew, M. C. (1932). Nitrogen compounds of gallium. III. Gallic nitride. *J. Phus. Chem , 36*, 2651-2654.

Kang, Y., Li, X., Gong, H., & Jiang, R. (2003). Study on Au diffusion in 0001 undoped wurtzite GaN. *Semiconductor Science and Technology , 18*, 607-610.

Karpinski, J., & Porowski, S. (1984). High pressure thermodynamics of GaN. *Journal of crystal growth , 66*, 11-20.

Kim, B. J., Tersof, J., Kodambaka, S., Reuter, M. C., Stach, E. A., & Ross, F. M. (2008). *Science , 322*, 1070.

Kim, B. J., Tersoff, J., Kodambaka, S., Reuter, M. C., A, S. E., & Ross, F. M. (2008). Kinetics of Individual Nucelation Events Observed in Nanoscale Vapor-Liquid-Solid Growth. *Science , 322*, 1070-1073.

Kim, H., Yan, H., Messer, B., Law, M., & Yang, P. (2002). Nanowire ultraviolet photodetectors and optical switches. *Advanced Materials , 14*, 158-160.

Kodambaka, S., Tersoff, J., Reuter, C. M., & Ross, F. M. (2007). Germanium Nanowire Growth Below the Eutectic Temperature. *Science , 316*, 729.

Kodambaka, Tersoff, J., Reuter, M. C., & Ross, F. M. (2006). Diameter-Independent Kinetics in the Vapor-Liquid-Solid Growth of Si Nanowires. *Physical Review Letters , 96*, 096105.

Krivanek, O. L., Dellby, N., & Lupini, A. R. (1999). Towards sub-A electron beams. *Ultramicroscopy , 78*, 1-11.

Kuykendal, T., Pauzauskie, P., Lee, S., Zhang, Y., Goldberger, J., & Yang, P. (2003). *Nano Lett. , 3*, 1063.

Lagerstedt, O., & Monemar, B. (1979). Variations of lattice parameter in GaN with stoichiometry and doping. *Physical Review B , 19*, 3064-3071.

Law, M., Goldberger, J., & Yang, P. *Semiconductor Nanowires and Nanotubes.*

Law, M., Goldberger, J., & Yang, P. (2004). Semiconductor Nanowires and Nanotubes. *Annu. Rev. Mater. Res. , 34*, 83-122.

Lee, J., Park, K., Kim, T., Choi, H., & Sung, Y. (2006). Controlled growth of high-quality TiO2 nanowires on sapphire and silica. *Nanotechnology* , 4317-4321.

Lee, N. E., Powell, R. C., Kim, Y. W., & Greene, J. E. (1995). *J. Vac. Sci. Technol. A , 13*, 2293.

Lester, S. D., Ponce, F. A., Craford, M. G., & Steigerwald, D. A. (1995). *Appl. Phys. Lett. , 66*, 1249.

Levinshtein, M. E., Rumyantsev, S. L., & Shur, M. S. (2001). *Properties of Advanced Semiconductor Materials: GaN, Al, In, Bn, and SiGe.* New York: John Wiley and Sons.

Li, Y., Qian, F., Xiang, J., & Lieber, C. (2006). Nanowire electronics and optoelectronic devices. *Materials Today , 9*, 18.

Lieber, C. M. (1998). One-dimensional nanostructures: chemistry, physics and applications. *Solid State Communications , 107*, 607-616.

Lu, W., & Lieber, C. M. (2007). Nanoelectronics from the bottom-up. *Nature Materials , 6*, 841-850.

Lymperakis, L., & Neugebauer, J. (2010, 07 26). *Ab-initio based growth simulations of III-Nitride nanostructures*. Retrieved 10 04, 2010, from Max-Planck-Institut: http://www.mpie.de/index.php?id=iii-nitride-nanostru

MacKenzie, J. D., Abernathy, C. R., Stweart, J. D., & Muhr, G. T. (1996). *J. Cryst. Growth , 164*, 143.

Mahajan, S., & Harsha, S. K. (1998). *Principles of growth and processing of semiconductors.* Boston: WCB McGraw-Hill.

Manasevit, H., Erdmann, F., & Simpson, W. (1971). Use of metalorganics in preparation of semiconductor materials. 4. Nitrides of aluminun and gallium. *Journal of Electrochemical Society , 118*, 1864.

Markov, I. V. (2003). *Crystal growth for beginners: Fundamentals of nucleation, crystal growth, and epitaxy* (2nd Edition ed.). London: World Scientific Publishing Co.

Martensson, T., Svensson, P., Wacaser, B., Larsson, M., Seifer, W., Deppert, K., et al. (2004). Epitaxial Growth of III-V Nanowires on Silicon. *Nano Letters , 4*, 1987-1990.

Marton, L. (1935). La microscopie electroniqe des objets biologiques. *Bull. Acad. r. Belg. Cl. Sci. , 21*, 553.

Maruska, H. P., & Tietjen, J. J. (1969). The preparation and properties of vapor-deposited single-crystal-line GaN. *Appl. Phy. Lett. , 15*, 327.

Mohammad, S. N., & Morkoc, H. (1996). Progress and prospects of group-III nitride semiconductors. *Prog. Quant. Electr. , 20*, 361-525.

Mohammad, S. N., Salvador, A. A., & Hadis, M. (1995). Emerging Gallium Nitride Based Devices. *Proc. IEEE , 83*, 1363.

Morkoc, H. (1999). *Nitride Semiconductors and Devices* (First ed.). Berlin: Springer.

Nakamura, S. (1991). *Jpn. J. Appl. Phys. , 30*, 1705.

Nakamura, S. (1998). GaN Growth Using GaN Buffer Layer. *Science , 281*, 956.

Nakamura, S. (1998). *The history of the blue laser diode.* New York: Springer.

Nakamura, S., Mukai, T., & Senoh, M. (1994). Candela-class high-brightness InGaN/AlGaN double-heterostrcuture blue-light-emitting diodes. *Appl. Phys. Lett. , 64*, 1687-1689.

Nakamura, S., Mukai, T., & Senoh, M. (1994). Candela-class high-brightness InGaN/AlGaN double-heterostructure blue-light-emitting diodes. *Appl. Phys. Lett. , 64*, 1687-1689.

Nakamura, S., Mukai, T., & Senoh, M. (1994). High-brightness InGaN/AlGaN double heterostructure blue-green light-emitting diodes. *J. Appl. Phys. , 76*, 8189-8191.

Nakamura, S., Mukai, T., Senoh, M., & Iwasa, N. (1992). Thermal annealing effects on p-type Mg-doped GaN films. *Jpn. J. Appl. Phys. , 31*, L139-L142.

Nakamura, S., Mukai, T., Senoh, M., Nagahama, S., & Iwasa, N. (1993). InxGa1-xN/InyGa1-yN superlattices grown on GaN films. *J. App. Phys. , 74*, 3911-3915.

Nakamura, S., Senoh, M., Nagahama, S., Iwasa, N., Yamada, T., Matsushita, T., et al. (1996). InGaN-based multi-quantum-well-structure laser diodes. *Jpn. J. Appl. Phys. , 35*, L74.

NNI. (2010). *About NNI - Funding*. Retrieved August 29, 2010, from National Nanotechnology Initiative: http://www.nano.gov/html/about/funding.html

Pankove, J. I., Miller, E. A., & Berkeyhe, J. E. (1971). GaN electroluminescent diodes. *RCA Review , 32*, 383.

Pashley, D. W. (1965). Nucleation growth structure and epitaxy of thin surface films. *Advances in Physics , 14*, 327.

Phillips, J. C. (1970). Ionicity of chemical bond in crystals. *Reviews of Modern Physics , 42*, 317.

Phillips, J. C. (1970). Ionicity of chemical bond in crystals. *Reviews of Modern Physics* , 317.

Ponce, F. A., Srinivasan, S., Bell, A., Geng, L., Liu, R., Stevens, M., et al. (2003). Microstructure and electronic properties of InGN alloys. *Phys. Stat. Sol. (B) , 240*, 273-284.

Porowski, J., & Grzegory, I. (1997). Thermodynamical properties fo III-V nitrides and crystal growth of GaN at high N2 pressures. *Journal of Crystal Growth , 178*, 174-188.

Porter, D. A., & Easterling, K. E. (2004). *Phase transformations in Metals and Alloys* (Second ed.). Boca Raton: CRC Taylor and Francis Group.

Predel, B., & Madelung, O. (1991-1998). *Landolt-Bornstein, Group IV Physical Chemestry - Phase Equilibria, Crystalographic and Thermodynamic Data of Binary Alloys* (Vol. 6). Berlin: Springer-Verlag.

Richardson, N. V., Holloway, S., & Unertl, W. N. (1996). *Physical Structure* (Vol. 1). Amsterdam: Elsevier.

Roco, M. C. (2007). National Nanotechnology Initiative - Past, Present, Future. In W. A. Goddard, D. W. Brenner, S. E. Lyshevski, & G. J. Iafrate, *Handbook of Nanoscience, Engineering and Technology* (Second Edition ed., pp. 3.1-3.2). New York: CRC Press Taylor & Francis Group.

Ruvimov, S., Liliental-Weber, Z., Washburn, J., Amano, H., Akasaki, I., & Koike, H. (1996). *Mat. Res. Soc. Symp. Proc , 423*, 487.

Schubert, L., Werner, P., Zakharov, N. D., Gerth, G., Kolb, F. M., Long, L., et al. (2004). *Appl. Phys. Lett , 84*, 4968.

Sharma, B. K. (2010, April 22). *SSPD CHAPTER 1 Part10 Concluded_Kronig-Penney Mode*. Retrieved September 09, 2010, from Conexions Org: http://cnx.org/content/m34271/latest/

Sharma, R. (2005). An environmental transmission electron microscope for in situ synthesis and characterization of nanomaterials. *Journal of Materials Research , 20*, 1695.

Sharma, R. (2009). Kinetic Measurement from In Situ TEM Observations. *Microscopy Research and Technique* , 144-152.

Shchukin, V. A., Ledentsov, N. N., & Bimberg, D. (2003). *Epitaxy of Nanostructures.* Berlin: Springer.

Shindo, D., & Oikawa, T. (2002). *Analytical Electron Microscopy for Material Science.* Tokyo: Springer.

Sinclair R., Y. T. (1981). Atomic motion on the surface of a cadmium telluride single crystal. *Nature , 290*, 386-388.

Sinclair, R., Yamashita, T., & Ponce, F. A. (1981). Atomic motion on the surface of a cadmium telluride single crystal. *Nature , 290*, 386-388.

Sirbuly, D. J., Law, M., Yan, H., & Yang, P. (2005). Semiconductor nanowires for subwavelength photonics integration. *Journal of Physical Chemistry B , 109*, 15190.

Stach, E. A., Pauzauskie, J., Kuykendall, T., Goldberger, J., He, R., & Yang, P. (2003). *Nano Lett. , 3*, 867.

Stiles, M. D., & Hammann, D. R. (1990). Electron transmission through silicon stacking faults. *Phys. Rev. B , 41*, 5280-5282.

Stringfellow, G. B. (1999). *Organometallic Vapor-Phase Epitaxy: Theory and Practice* (Second ed.). San Diego: Academic Press.

Sunagawa, I. (2005). *Crystals: Growth, Morphology and Perfection.* Cambridge: Cambridge University Press.

Tang, C. C., Fan, S., Dang, H. Y., Li, P., & Liu, Y. M. (2000). *Appl. Phy. Lett , 77*, 1961.

Taniguchi, N. (1974). On the basic concep of Nano-Technology. *International Conference on Production Ingineering.* Tokyo: Japan Society of Precision Engineering.

Tham, D., Nam, C.-Y., & Fischer, J. E. (2006). Dfects in GaN Nanowires. *Advanced Functional Materials , 16*, 1197-1202.

Tro, N. J. (2008). *Chemistry.* New Jersey: Pearson Education, Inc.

Ullrich, B. (2001, January 1). *Kottan-Labs*. Retrieved 11 30, 2010, from Kottan Labs Workshop 2001: http://kottan-labs.bgsu.edu/teaching/workshop2001/chapter5.htm

Unland, J., Onderka, B., Davydov, A., & Schmid-Fetzer, R. (2003). Thermodynamics and Phase stability in the Ga-N system. *Journal of Crystal Growth , 256*, 33-51.

Wacaser, B. A., Dick, K. A., Johansson, J., Borgstrom, M. T., Deppert, K., & Samuelson, L. (2008). Preferential Interface Nucleation: An Expansion of the VLS Growth Mechanism for Nanowires. *Advanced Materials , 21*, 153-165.

Wagner, R. S., & Ellis, W. C. (1964). Vapor-solid-liquid mechanism of single crystal growth. *Appl. Phys. Lett. , 4*, 89.

Wang, J., Gudiksen, M., Duan, X., Cui, Y., & Lieber, C. M. (2001). Highly polarized photoluminescense from single indium phosphide nanowires and photodetection application. *Science , 293*, 1455-1457.

Weisbuch, C., & Borger, V. (1991). *Quantum semiconductor structures: fundamental and applications.* Boston: Academic Press.

Wen, C. Y., Reuter, M. C., Tersoff, J., Stach, E. A., & Ross, F. M. (2010). Structure, Growth Kinetics, and Ledge Flow during Vapor-Solid-Solid Growth of Copper-Catalyzed Silicon Nanowires. *Nano Letters , 10*, 514-519.

Weng, X., Burke, R. A., & Redwing, J. M. (2009). The nature of catalyst particles and growth mechanisms of GaN nanowires by Ni-assisted metal-organic chemical vapor deposition. *Nanotechnology , 20*, 085610.

Williams, D. B., & Carter, B. C. (1996). *Transmission electron microscopy.* New York: Springer .

Wright, A. F. (1997). *J. Appl. Phys. , 82*, 5259.

Wu, Y., & Yang, P. (2001). Direct Observation of the Vapor-Liquid-Solid Nanowire Growth. *J. Am. Chem. Soc. , 123*, 3165-3166.

Wu, Y., Fan, R., & Yang, P. D. (2002). Block-by-block growth of single-crystalline Si/SiGe superlattice nanowires. *Nano Letters , 2*, 83-86.

Xia, Y., Yang, P., Sun, Y., Wu, Y., Mayers, B., Gates, B., et al. (2003). One-Dimensional Nanostructures: Synthesis, Characterization, and Applications. *Adv. Mater. , 15*, 353.

Yagi, K., Takayanagi, K., Kobayashi, K., & Honjo, G. (1976). In Situ Electron Microscope Studies On Epitaxial Growth of Thin Metals on Metal Substrates. *Thin Solid Films , 32*, 185-190.

Yazawa, M., Koguchi, M., Muto, A., Ozawa, M., & Hiruma, K. (1992). Effect of one monolayer of surface gold atoms on the epitaxial-growth of InAs nanowhiskers. *Appl. Phys. Lett , 61*, 2051-2053.

Appendix A

[TITLE OF APPENDIX IN ALL CAPS]

[Insert text of appendix here. Do not repeat appendix title.]